# RCA Review

December 1976 Volume 37 No. 4

RCARCI 37(4) 435-550 (1976)

RCA Review, published quarterly in March, June, September and December by RCA Research and Engineering, RCA Corporation, Princeton, New Jersey 08540. Entered as second class matter July 3, 1950 under the Act of March 3, 1879. Second-class postage paid at Princeton, New Jersey, and at additional mailing offices. Effective Jan. 1, 1971, subscription rates as follows: United States and Canada: one year $6.00, two years $10.50, three years $13.50; in other countries, one year $6.40, two years $11.30, three years $14.70. Single copies (except for special issues) up to five years old $3.00.

RCA
Review

A technical journal published quarterly by RCA Research and Engineering in cooperation with the subsidiaries and divisions of RCA.

## Contents

December 1976 Volume 37 Number 4

# Extending the Content and Expanding the Usefulness of the Simple Gaussian Lens Equations

**L. T. Sachtleben**

**Abstract**—The two classical, simple Gaussian lens equations relate four variables; this study extends them to three equations and adds a fifth, composite variable. The equations are stabilized and kept analytically manageable by adopting a purely optical sign convention proposed by Gardner. A table presents complete solutions of the three equations. Further usefulness of the equations is developed by applying them to the case of two separated lenses, or systems in air or vacuum. Partial solutions are derived, and a few representative two-lens applications are developed. General use of the solutions is simplified by a transformation. The extended equations are useful in planning new systems, and in analyzing and further developing an existing or proposed system. Their use may precede or accompany considerations of both photometry and computer-programmed correction of aberrations. They are *not* useful in the case of systems such as high-speed spherical condensers, whose aberrations though minimized or otherwise adjusted will remain large and uncorrected.

## 1. Introduction

The academic, research, or engineering worker who is required to use the simple Gaussian lens equations to obtain first-order solutions to lens problems, is likely to have some frustrating experiences. This can sometimes happen, even if the problem involves only one simple lens. But the difficulties can mount very rapidly if the problem involves two or more separated lenses on a common axis. Not the least frustrating part of such a problem will be the worker's inability to find clear and efficient guidance in available optical literature.

In any event, the statements just made reflect the writer's own experience; an experience that slowly and indirectly resulted in his working out the relationships presented here. If these, or other equally useful, or more useful Gaussian relationships are well known in the optical industry, they remain a part of its fund of proprietary information that does not find its way into optical literature.

## 2. The Historical Background

The simple Gaussian equations for a lens in air or vacuum, enable us to deal with lens problems that are framed in terms of the following quantities (see Fig. 1):

(1) an object distance, $x$;
(2) an image distance, $y$;
(3) a focal length, $f$;
(4) a transverse magnification, $M$.

The equations have the typical form

$$\frac{1}{x} + \frac{1}{y} = \frac{1}{f}$$

$$\frac{y}{x} = M.$$

These two equations are commonly referred to as the "thin-lens" equations, and they are ordinarily applied on the assumption that the lens thickness is zero.

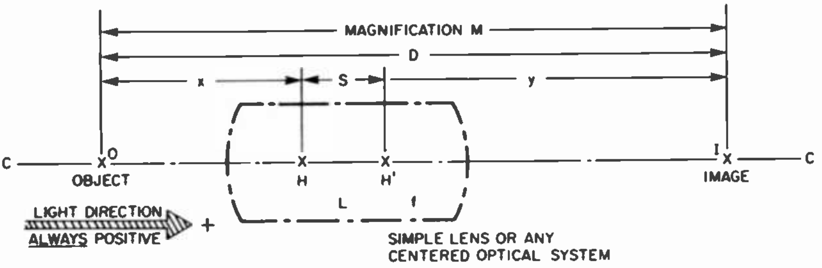

Fig. 1—Simple lens or any centered optical system.

Gauss' theory of the principal points of a lens or optical system showed, in 1840, that the thin-lens equations can be applied to a "thick" lens, or to any lens system, if the principal point locations are known or assumed.[1,2] Since that time, optical literature appears to have been well satisfied with Gauss' solution to the thick-lens problem; in practice, however, first-order solutions to many such problems remain very difficult to accomplish. The reason for this difficulty is two-fold:

(1) A large and very confusing assortment of sign conventions exists in the literature.[3]

(2) Gauss' solution to the thick-lens problem is customarily applied in the manner of a rule-of-thumb practical expedient. The solution, and

its broad implications, have not received a general mathematical formulation and development in optical literature.

## 3. Extension of the Content of the Equations

The sign convention situation was neatly resolved in 1927 by I. C. Gardner of the Bureau of Standards, who replaced the usual Cartesian frame of reference by a purely optical reference frame for determining signs.[4] In the Gardner scheme the positive direction is defined simply as the direction of light-travel through a lens or system. By defining the initial and terminal points of any relevant optical distance or segment along the optical axis, the sign of the distance becomes positive if its direction (from the initial to the terminal point) is the same as that of the light; otherwise it is negative.

When the sign convention question is settled in this manner and a new equation is set up that represents Gauss' solution to the thick-lens problem, the simple lens equations take the *permanent* form:

$$\frac{1}{y} - \frac{1}{x} = \frac{1}{f} \qquad [1]$$

$$\frac{y}{x} = M, \qquad [2]$$

$$y - x = (D - S), \qquad [3]$$

where (see Fig. 1) $D$ is the object-to-image distance, with the object defined by the writer to be the initial point. The image is the terminal point. Distance $S$ is the first-to-second principal point distance, with the first principal point $H$ also defined by the writer to be the initial point. The second principal point $H'$ is the terminal point.

In the light of Gauss' theory of principal points, the initial point of the object-distance $x$ is, in effect, defined by Gardner to coincide with the first principal point $H$. Its terminal point is the object 0. The initial point of the image-distance $y$ is similarly defined as the second principal point $H'$. Its terminal point is the image $I$.

Negative values of the magnification $M$ correspond to inverted images and positive values of $M$ to upright images.[5] Negative values of the focal length $f$ correspond to a diverging lens, and positive values of $f$ correspond to a converging lens.

Although the sign convention proposed by Gardner was originally restricted to the thin-lens case, its unique and valuable property of being a purely optical convention is not lost when it is extended to the thick-lens case, in the manner of Gauss' solution. It should, therefore, continue

*Table 1*—Extension of the Simple Gaussian Lens Eqs. [1], [2], and [3] (Complete Solution of the Equation Set: $(1/y) - (1/x) = (1/f)$; $M = (y/x)$; and $(D - S) = -x + y$). The Gardner Sign Convention Applies *Without Exception*

| Independent Variables | Dependent Variables | | | | |
|---|---|---|---|---|---|
| | I<br>$(D - S)$ | II<br>$f$ | III<br>$x$ | IV<br>$y$ | V<br>$M$ |
| 1. $x, y$ | $-x + y$ | $\frac{xy}{x - y}$ | $x$ | $y$ | $\frac{y}{x}$ |
| 2. $x, f$ | $\frac{-x^2}{f + x}$ | $f$ | $x$ | $\frac{fx}{f + x}$ | $\frac{f}{f + x}$ |
| 3. $x, M$ | $-x(1 - M)$ | $\frac{Mx}{1 - M}$ | $x$ | $Mx$ | $M$ |
| 4. $x, (D - S)$ | $(D - S)$ | $\frac{x^2 + (D - S)x}{-(D - S)}$ | $x$ | $(D - S) + x$ | $\frac{(D - S) + x}{x}$ |
| 5. $y, f$ | $\frac{-y^2}{f - y}$ | $f$ | $\frac{fy}{f - y}$ | $y$ | $\frac{f - y}{f}$ |
| 6. $y, M$ | $\frac{-y(1 - M)}{M}$ | $\frac{y}{1 - M}$ | $\frac{y}{M}$ | $y$ | $M$ |
| 7. $y, (D - S)$ | $(D - S)$ | $\frac{-y^2 + (D - S)y}{(D - S)}$ | $y - (D - S)$ | $y$ | $\frac{y}{y - (D - S)}$ |
| 8. $f, M$ | $\frac{-f(1 - M)^2}{M}$ | $f$ | $\frac{f(1 - M)}{M}$ | $f(1 - M)$ | $M$ |
| 9. $f, (D - S)$ | $(D - S)$ | $f$ | $x^2 + (D - S)x$<br>$+(D - S)f = 0$ | $y^2 - (D - S)y$<br>$+(D - S)f = 0$ | $M^2 + 1 - \left[2 - \frac{(D - S)}{f}\right]M = 0$ |
| 10. $M, (D - S)$ | $(D - S)$ | $\frac{-(D - S)M}{(1 - M)^2}$ | $\frac{-(D - S)}{1 - M}$ | $\frac{-(D - S)M}{1 - M}$ | $M$ |

to be known as the Gardner sign convention, although certain arbitrary elements have been added by the writer.

When the content of the equations is extended by including both $S$ and $D$ among the relevant quantities with which they are concerned, the usual two Gaussian lens equations become three in number. As a result, both the analytical significance and the practical usefulness of the equations are greatly expanded.

## 4. Significance of the Three Equations for a Single Lens or System

The three equations involve five variables, it being convenient to regard $(D - S)$ as a single variable. Any one of these variables may be expressed in terms of the remaining four taken two at a time. The complete set of such solutions is presented in Table 1. Each Roman-numeral column of the table is headed by a dependent variable, and each Arabic-numeral row is preceded by two independent variables in terms of which each of the remaining three dependent variables is expressed. The expressions for the dependent variables appear at the intersections of the appropriate rows and columns.

The thirty expressions of Table 1 allow all of the variables in the three equations to be calculated when any two of them are given or assumed. In the case of row 9 of the table, the expression is quadratic in the dependent variable $x$, $y$, or $M$, and the expression can consequently have complex solutions for certain sets of values of the independent variables $f$ and $(D - S)$. Such complex solutions correspond to the well-known thin-lens situation in which $S = 0$, and

$$\infty > \frac{4f}{D} > 1 < \frac{4f}{y - x} < \infty.$$

The occurrence of a complex solution always means that there can be no physical optical system that corresponds to the chosen values of the independent variables.

The simplest solution for $x$, $y$, and $M$ in row 9 in Table 1 is as follows. From (V-9),

$$M_{1,2} = \left\{1 - \frac{D - S}{2f}\right\} \pm \sqrt{\left\{1 - \frac{D - S}{2f}\right\}^2 - 1};$$

from (III-10),

$$x_{1,2} = -\frac{D - S}{1 - M_{1,2}},$$

and from (IV-10)

$$y_{1,2} = -\frac{(D-S)M_{1,2}}{1-M_{1,2}} \text{ and } y_2 = -x_1; y_1 = -x_2; M_2 = 1/M_1.$$

Table 1 can be said to contain the solution of any problem that concerns only a single lens, or that concerns a system of lenses that is regarded as only a single image-forming entity represented by two principal points and a focal length. An ordinary photographic lens is a good example of such a system.

The Gardner sign convention governs the sign of each linear quantity that enters any expression in the table. It also governs the interpretation of the sign of each solution in accordance with the definitions of the initial and terminal points of $x$, $y$, $D$, and $S$ and in accordance with the definitions of the signs of $M$ and $f$ that were given above. There are *no* exceptions to this rule. The Gardner sign convention *never* has to be changed from the form given here. The occasional problem that may be troublesome because it involves an indeterminate form will not require any change in the sign convention or its manner of application to the problem.

## 5. Significance of the Extended Simple Lens Equations For Two Separated Lenses or Systems

A group of problems of much interest concerns two separated lenses or lens systems on a common axis. The axis is defined as the straight line on which lie all of the centers of curvature of the spherical refracting surfaces of the system. These problems are often very difficult to solve on the restricted four-variable basis of Eqs. [1] and [2], even when additional equations that apply to separated lenses are deduced from Eqs. [1] and [2]. The general solution of such two-lens problems is very much simplified by the extended relationships of Eqs. [1], [2], and [3], and the equations of Table 1.

Two separated lenses, or two separated optical systems on a common axis c-c, are represented schematically by Fig. 2. The lenses or systems are $L_1$ and $L_2$. The distances, principal points, and other quantities that are locally or immediately associated with either of them are given the same ordinal subscript as the lens, or system. Of themselves, the subscripts indicate the order in which the light reaches and passes through the two lenses or systems.

The separation of $L_2$ from $L_1$ is an optical separation, and is the distance $a$ from the second principal point of $L_1$ as initial point, to the first principal point of $L_2$ as terminal point, with its sign conforming to the Gardner convention. Table 2 identifies each of the quantities represented in Fig. 2 and in Fig. 1, and defines the sense of the corresponding directed axial line segments. By the Gardner sign convention the sign of any such finite segment is positive when its sense coincides with the direction of the light through the system; otherwise its sign is negative.

In Fig. 2, L$_1$ has a focal length $f_1$, and produces an image of 0 at 0′, the magnification being $M_1$. L$_2$ likewise has focal length $f_2$, and reimages 0′ at I with magnification $M_2$. By this two-stage or relay-type imaging sequence, 0 is finally imaged at I, the overall magnification being

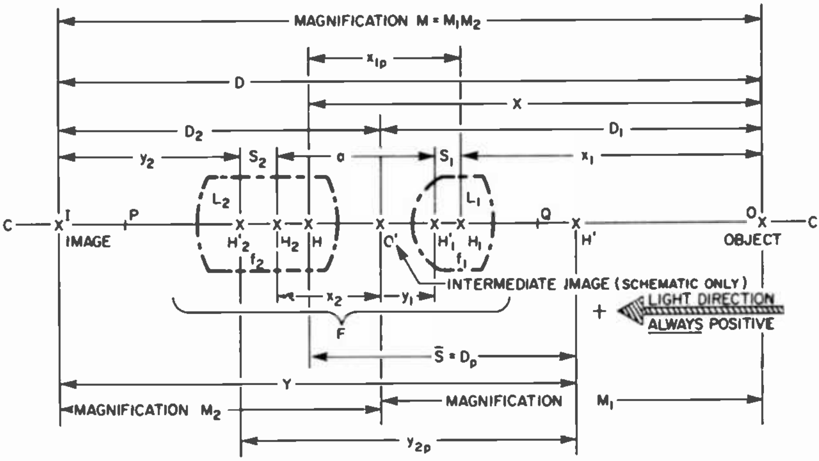

Fig. 2—Two separated lenses, or two separated optical systems, centered on c-c and with optical separation *a*.

$$M = M_1 M_2 \tag{4}$$

Inspection of Fig. 2 reveals the following two relations, when the Gardner sign convention is kept in mind,

$$y_2 = x_1 - S_1 - a - S_2 + D \tag{5}$$

$$x_2 = y_1 - a. \tag{6}$$

By suitably using the relationships of Table 1, together with Eqs. [4] through [6], the following two equations that express the principal or primary working relationship between six of the seven primary variables of Table 2 may be established. For convenience $(D - S_1 - S_2)$ is considered a single primary variable.

$$f_1 = \frac{-M x_1 a}{(1 - M)(x_1 - a) + D - S_1 - S_2}, \tag{7}$$

$$f_2 = \frac{a(x_1 + D - S_1 - S_2) - a^2}{(1 - M)\, x_1 + D - S_1 - S_2}. \tag{8}$$

*Table 2*—Key to the Sense of the Applicable Directed Axial Line Segments in Fig. 2 (and Fig. 1)

| Ser. No. | Segment Symbol | Sense of the Segment | Name of Segment | Rank (Fig. 2 Only) |
|---|---|---|---|---|
| 1* | $x_1$ | $H_1O$ (*Not* $OH_1$) | Object Distance Relative to $L_1$ | Primary |
| 2 | $S_1$ | $H_1H_1'$ (*Not* $H_1'H_1$) | Principal Point Separation; for $L_1$ | Primary |
| 3 | $f_1$ | ........... | Focal Length of $L_1$ (*not* represented by a segment) | Primary |
| 4 | $a$ | $H_1'H_2$ (*Not* $H_2H_1'$) | Optical Separation; $L_2$ from $L_1$ | Primary |
| 5 | $S_2$ | $H_2H_2'$ (*Not* $H_2'H_2$) | Principal Point Separation; for $L_2$ | Primary |
| 6 | $f_2$ | ........... | Focal Length of $L_2$ (*not* represented by a segment) | Primary |
| 7 | $y_2$ | $H_2'I$ (*Not* $IH_2'$) | Image Distance Relative to $L_2$ | Primary |
| 8 | $y_1$ | $H_1'O'$ (*Not* $O'H_1'$) | Intermediate Image Distance; Relative to $L_1$ | Secondary |
| 9* | $x_2$ | $H_2O'$ (*Not* $O'H_2$) | Intermediate Object Distance; Relative to $L_2$ | Secondary |
| 10 | $D$ (Figs. 1 & 2) | OI (*Not* IO) | Object-to-Image Distance (Figs. 1 & 2) | Primary |
| 11 | $F$ (or $f$, Fig. 1) | ........... | Focal Length; System $L_1L_2$ (*not* represented by a segment) (or System L, Fig. 1) | Secondary |
| 12* | $\overline{S} = D_p$ (or $S$, Fig. 1) | HH′ (*Not* H′H) | Principal Point Separation; System $L_1L_2$ (or L, Fig. 1) | Secondary |
| 13† | $X$ (or $x$, Fig. 1) | HO (*Not* OH) | Object Distance; System $L_1L_2$ (or L, Fig. 1) | Secondary |
| 14 | $Y$ (or $y$, Fig. 1) | H′I (*Not* IH′) | Image Distance; System $L_1L_2$ (or L, Fig. 1) | Secondary |
| 15* | $M_1 = \frac{y_1}{x_1}$ | ........... | Partial Transverse Magnification; for $L_1$ (*not* represented by a segment) | Secondary |
| 16* | $M_2 = \frac{y_2}{x_2}$ | ........... | Partial Transverse Magnification; for $L_2$ (*not* represented by a segment) | Secondary |
| 17 | $M\left(= M_1M_2 = Y/X = \frac{y_1}{x_1}\cdot\frac{y_2}{x_2}\right)$ | ...........<br>Parenthetic Statement *Not* Applicable to Fig. 1. | Magnification; System $L_1L_2$ (or L, Fig. 1) (*not* represented by a segment) | Primary |
| 18 | $H_1H = x_{1p}$ | $H_1H$ (*Not* $HH_1$) | Location of H Relative to $L_1$ | Secondary |
| 19* | $H_2'H' = y_{2p}$ | $H_2'H'$ (*Not* $H'H_2'$) | Location of H′ Relative to $L_2$ | Secondary |
| 20 | $D_1$ | OO′ (*Not* O′O) | Partial Object-to-Image Distance; for $L_1$ | Secondary |
| 21 | $D_2$ | O′I (*Not* IO′) | Partial Object-to-Image Distance; for $L_2$ | Secondary |

* These items are (shown) negative in Fig. 2.

† This item is (shown) negative in Fig. 2 and in Fig. 1.

## 6. The Replacement Transformation

The thirty equations of Table 1, Eqs. [4] through [8], and all *general* equations that may be derived from those thirty-five equations, may be conveniently transformed by means of the transformation replacements that are scheduled in Table 3.

*Table 3*—Schedule of Transformation Replacements. Make *All* Replacements of This Table, As May Be Applicable in Any Particular General Working Equation Pertaining to Fig. 2, Fig. 1, and Table 1. Keep Light Direction Unchanged and Continue Observance of Gardner Sign Convention.

| Item | Replace | By |
|---|---|---|
| 1 | $x_1$ | $-y_2$ |
| 2 | $y_2$ | $-x_1$ |
| 3 | $f_1$ | $f_2$ |
| 4 | $f_2$ | $f_1$ |
| 5 | $S_1$ | $S_2$ |
| 6 | $S_2$ | $S_1$ |
| 7 | $a$ | $a$ |
| 8 | $M$ (Figs. 1 or 2) | $1/M$ (Figs. 1 or 2) |
| 9 | $\underline{D}$ (Figs. 1 or 2) | $\underline{D}$ (Figs. 1 or 2) |
| 10 | $D_p = \bar{S}$ (or $S$, Fig. 1) | $D_p = \bar{S}$ (or $S$, Fig. 1) |
| 11 | $X$ (or $x$, Fig. 1) | $-Y$ (or $-y$, Fig. 1) |
| 12 | $Y$ (or $y$, Fig. 1) | $-X$ (or $-x$, Fig. 1) |
| 13 | $F$ (or $f$, Fig. 1) | $F$ (or $f$, Fig. 1) |
| 14 | $\mathrm{H_1H} = x_{1p}$ | $-\mathrm{H_2'H'} = -y_{2p}$ |
| 15 | $\mathrm{H_2'H'} = y_{2p}$ | $-\mathrm{H_1H} = -x_{1p}$ |
| 16 | $y_1$ | $-x_2$ |
| 17 | $x_2$ | $-y_1$ |
| 18 | $M_1$ | $1/M_2$ |
| 19 | $M_2$ | $1/M_1$ |
| 20 | $D_1$ | $D_2$ |
| 21 | $D_2$ | $D_1$ |

By using the replacement transformation, each equation of Table 1 is transformed either into itself or into another equation of the Table. Eqs. [4] through [6] are transformed into themselves, but Eq. [8] transforms into

$$f_1 = \frac{Ma(-y_2 + D - S_1 - S_2) - Ma^2}{(1 - M)y_2 + M(D - S_1 - S_2)}, \qquad [9]$$

and Eq. [7] transforms into

$$f_2 = \frac{ay_2}{(1 - M)(y_2 + a) + M(D - S_1 - S_2)}. \qquad [10]$$

Thus, two new equations are formed with a minimum of work.

Some of the primary working equations that are presented here, and some of the equations that may be derived from them, are obtained through the use of what is quite tedious algebra. In many instances, however, such as in the case above, the use of the replacement transformation avoids much unnecessary work. It will be advantageous to use this transformation wherever possible in developing new solutions.

## 7. Primary Working Equations For Two Separated Lenses or Systems

The principal relationship, expressed by Eqs. [7] and [8], can be solved in a number of different ways to obtain additional primary working equations that involve only the primary variables of Table 2. The general approach is to solve both Eqs. [7] and [8] for any one of the four variables that appear in both equations, then eliminate that variable and solve the resulting equation for each of the remaining variables in turn. This process will produce seven new equations for each variable that is eliminated. Application of the replacement transformation will then double the number of primary working equations, except in those cases where an equation transforms into itself.

The basic derivations of the primary working equations are as follows:

I. $$D - S_1 - S_2 = \frac{-Mx_1a - (1 - M)(x_1 - a)f_1}{f_1}, \text{ from Eq. [7]}, \qquad [11]$$

$$D - S_1 - S_2 = \frac{x_1[a - (1 - M)f_2] - a^2}{f_2 - a}, \text{ from Eq. [8]}. \qquad [12]$$

By eliminating $D - S_1 - S_2$ between Eqs. [11] and [12],

$$M = \frac{f_1f_2}{(f_1 + f_2 - a)x_1 + f_1(f_2 - a)}. \qquad [13]$$

II. $$x_1 = \frac{-f_1[D - S_1 - S_2 - (1 - M)a]}{f_1(1 - M) + Ma}, \text{ from Eq. [7]}, \qquad [14]$$

$$x_1 = \frac{(a - f_2)(D - S_1 - S_2) - a^2}{f_2(1 - M) - a}, \text{ from Eq. [8]}. \qquad [15]$$

By eliminating $x_1$, between Eqs. [14] and [15],

$$a = \frac{D - S_1 - S_2}{2} \pm \sqrt{\left(\frac{D - S_1 - S_2}{2}\right)^2 - (D - S_1 - S_2)(f_1 + f_2) - \frac{(1 - M)^2}{M} f_1 f_2} \qquad [16]$$

III. $M = \dfrac{f_1(D - S_1 - S_2 + x_1 - a)}{f_1(x_1 - a) - a x_1}$, from Eq. [7], [17]

$$M = \frac{f_2(x_1 + D - S_1 - S_2) - a(x_1 - a + D - S_1 - S_2)}{f_2 x_1}, \text{ from} \qquad [18]$$

Eq. [8]. By eliminating $M$ between Eqs. [17] and [18],

$$D - S_1 - S_2 = a - x_1 + \frac{f_2[(f_1 - a)x_1 - f_1 a]}{(f_1 + f_2 - a)x_1 + f_1(f_2 - a)}. \qquad [19]$$

IV. $a = \dfrac{f_1[(1 - M)x_1 + D - S_1 - S_2]}{(1 - M)f_1 - M x_1}$, from Eq. [7]. [20]

$$a = \frac{x_1 + D - S_1 - S_2}{2} \pm \sqrt{\left(\frac{x_1 + D - S_1 - S_2}{2}\right)^2 - f_2[(1 - M)x_1 + D - S_1 - S_2]}, \qquad [21]$$

from Eq. [8]. By eliminating $a$ between Eqs. [20] and [21],

$$x_1 = \frac{f_1 M[2f_2(1 - M) - (D - S_1 - S_2)]}{2(f_1 M + f_2 M^2)} \pm \left[\left(\frac{f_1 M[2f_2(1 - M) - (D - S_1 - S_2)]}{2(f_1 M + f_2 M^2)}\right)^2 - \frac{f_1^2[f_2(1 - M)^2 + M(D - S_1 - S_2)]}{f_1 M + f_2 M^2}\right]^{1/2}, \qquad [22]$$

Eqs. [13], [16], [19], and [22] may be solved explicitly for any of their variables. They are all subject to the replacement transformation process (Eq. [16] transforms into itself). All transformed equations may be solved explicitly for any of their variables.

While the thirty equations of Table 1 comprise *all* the solutions for a single lens or system, no correspondingly simple tabulation of all the solutions for two separated lenses, or systems, is possible due to the large number of variables involved. Many such solutions have to be worked out as they are needed by using Table 1, Eqs. [4] through [22], the replacements of Table 3, and the clarifying rationale of the Gardner sign convention.

## 8. An Inherent Property of Principal Points

The two principal points of a lens or optical system have the inherent property that they are conjugate to each other, the magnification being +1. This property is easily demonstrated by noting (IV, 2) in Table 1, where

$$y = \frac{fx}{f + x} \qquad [23]$$

from which $y = 0$, when $x = 0$. This means that when the object coincides with the first principal point, the image coincides with the second principal point.

From (V, 2) and (V, 5) in Table 1,

$$M = \frac{f}{f + x} \qquad [24]$$

$$M = \frac{f - y}{f}; \qquad [25]$$

thus making it clear that in the case where either $x = 0$ or $y = 0$, $M = +1$. The relationships of Table 1 also show this property to be consistent with (I, 1) of the table, which states

$$(D - S) = -x + y, \qquad [26]$$

whence (D − S) = 0 when $x = y = 0$, or when $M = +1$.

The reader can easily calculate from Table 1 the values of $x$, $y$, and $M$ when $(D - S) = 0$; in particular by using (III, 9), (IV, 9), and (V, 9) of the table. The other relations in the table that are instructive in this respect are (III, 7), (III, 10), (IV, 4), (IV, 10), (V, 4), and (V, 7), some of which result in an indeterminacy that it is instructive to resolve. In column II of Table 1, the indeterminacy of $f$ when $(D - S) = 0$ is such a case.

## 9. The Principal Points of a System of Two Separated Lenses (or Sub-Systems)

There is no problem in designing a two-lens system with its principal points in any desired location, and order, on the common axis. It is only necessary to set $M = +1$ in Eqs. [7] and [8], whence

$$f_1 = \frac{-ax_{1p}}{D_p - S_1 - S_2},\ (M = +1) \text{ and} \qquad [27]$$

$$f_2 = \frac{a(x_{1p} + D_p - S_1 - S_2) - a^2}{D_p - S_1 - S_2},\ (M = +1) \qquad [28]$$

wherein the $p$-subscript is added to $D$ to identify it as the distance $\overline{S}$ between the principal points $H$ and $H'$ of the system of Fig. 2. Similarly, $x_{1p}$ is the distance from $H_1$ to $H$ of Fig. 2, when $M = +1$. Every quantity on the right-hand side of both Eqs. [27] and [28] may be assigned an arbitrary value. Values that make $f_1 = 0$ or $f_2 = 0$ must be avoided, since for photometric reasons no physical lens or optical system can have a "zero" focal length. Infinite values of $x_1p$ and $D_p$ involve interesting special cases that are not discussed here.

If two lenses or systems with arbitrary focal lengths $f_1$ and $f_2$, are coaxial with an optical separation $a$, it is useful to be able to calculate the locations of the principal points of the overall system. By solving Eq. [16] for $D$,

$$D = \frac{-a^2 - \dfrac{(1 - M)^2}{M} f_1 f_2}{f_1 + f_2 - a} + S_1 + S_2. \qquad [29]$$

This equation gives the object-to-image distance $D$ for any magnification $M$. In particular, if $M = +1$,

$$D_p = \overline{S} = \frac{-a^2}{f_1 + f_2 - a} + S_1 + S_2,\ (M = +1) \qquad [30]$$

which is the separation of the two principal points of the overall system, or the distance $H - H'$ of Fig. 2.

By solving Eq. [13] for $x_1$,

$$x_1 = \frac{f_1[f_2 - M(f_2 - a)]}{M(f_1 + f_2 - a)}, \qquad [31]$$

which gives the object-distance $x_1$ for any magnification $M$. In the special case where $M = +1$,

$$x_{1p} = \frac{f_1 a}{f_1 + f_2 - a}, \qquad [32]$$

which is the distance from $H_1$ to $H$ of Fig. 2.

Eq. [30] transforms into itself when the replacement transformation is applied to it, but Eq. [32] transforms into

$$y_{2p} = \frac{-f_2 a}{f_1 + f_2 - a}, \; (M = +1) \qquad [33]$$

which is the distance $H_2' - H'$ in Fig. 2. The $p$-subscript is added to $x_1$ in Eq. [32] and to $y_2$ in Eq. [33] to denote that the terminal points of $x_1$ and $y_2$ coincide, respectively, with the principal points $H$ and $H'$ of the overall system of Fig. 2. Eqs. [32] and [33] are developed in other ways in the literature.[6,7]

## 10. The Conjugate Displacement Theorem; a Further Extension of the Usefulness of the Simple Gaussian Lens Equations

If two object-points on the axis of an optical system are separated by any arbitrary finite distance, this distance can be called a displacement $\Delta x$ in the object-space. Similarly, if two image-points on the axis are separated by any arbitrary finite distance, the distance can be called a displacement $\Delta y$ in the image-space.

If the two image-points are not arbitrary, but happen to be the conjugates of the two arbitrary object-points, a special relation between $\Delta x$ and $\Delta y$ is implied. In this case the finite displacement $\Delta y$ is the conjugate of the finite displacement $\Delta x$. When the related displacements are being considered in their conjugate sense, they are designated respectively as $\Delta_c y$ and $\Delta_c x$, to distinguish them from simple, arbitrary increments of some image-distance $y$ and of some unrelated object-distance $x$.

From (IV, 8) in Table 1, we may write

$$y = f(1 - M), \qquad [34]$$

$$y' = f(1 - M'), \qquad [35]$$

from which

$$y' - y = f(M - M'). \qquad [36]$$

Similarly, from (III, 8) in Table 1 we may write

$$x = \frac{f(1 - M)}{M}, \qquad [37]$$

$$x' = \frac{f(1 - M')}{M'}, \qquad [38]$$

from which

$$x' - x = \frac{f(M - M')}{MM'}. \qquad [39]$$

When Eq. [36] is divided by Eq. [39],

$$\frac{y' - y}{x' - x} = MM', \qquad [40]$$

wherein the magnification $M(=y/x)$ corresponds to the conjugate distance pair $(x, y)$, and magnification $M'(=y'/x')$ corresponds to the conjugate distance pair $(x',y')$. The fixed focal length of the optical system has cancelled out, and the finite displacement $y' - y$ in the image-space is the conjugate of the finite displacement $x' - x$ in the object-space. Therefore we may rewrite Eq. [40] in the form

$$\Delta_c y = MM' \Delta_c x. \qquad [41]$$

Eq. [41] is the conjugate displacement theorem for any fixed-focal-length optical system in air or vacuum.

The conjugate displacement theorem has received no explicit statement, and therefore no discussion in the literature. The closest approach to a derivation of this theorem appears in Conrady,[8] but the derivation is not completed.

By substituting Eq. [36] into Eq. [40] and solving for $f$,

$$f = \frac{-MM'\Delta_c x}{M' - M}. \qquad [42]$$

By similarly substituting Eq. [39] into Eq. [40], the focal length becomes

$$f = \frac{-\Delta_c y}{M' - M}. \qquad [43]$$

The derivation of the conjugate displacement theorem does not involve Gauss' theory of principal points, or the extended five-variable form of the simple Gaussian lens equations. The theorem is an indispensable adjunct to the equations for two separated lenses or systems, when developing the general Gaussian theory of relay optical systems. Taken by itself, the theorem can lead to quick answers to certain otherwise very knotty problems.

## 11. Conclusion

The foregoing is a brief, introductory description of a useful extension of the simple Gaussian lens equations. This extension recasts the equations into a more general form that is directly applicable to problems for which they were not previously well suited.

The new form of the equations, together with the indispensable Gardner sign convention, makes possible an analytical approach to problems that have not been easily amenable to Gaussian treatment in the past.

The extension, as it applies to a single lens or single system of lenses, is complete. As it applies to two separated lenses or two separated lens systems (sub-systems), a principal relationship has been derived that can be further extended, as necessary, using general analytical methods.*

Details of such further extensions are developed, as required, in solving the problems given in the examples that follow. The forms that the extensions take, depend both upon the problem and upon the ingenuity of the problem solver. In practice, they can take an endless variety of forms of which only a few are developed here.

Where the problem is to develop or design a high-speed condenser, or illuminating system whose aberrations will not be corrected, the Gaussian equations are *not* useful.[9]

## 12. Representative Applications

A large number of different kinds of problems either involve two separated lenses, or can best be solved in a preliminary way by employing two separated lenses (or sub-systems) on a common axis. The equations for such two-lens arrangements provide a firm basis for study and analysis of possible Gaussian solutions to many lens problems.

### Example 1: Setting Up Two Given Lenses to Produce an Optical System That Has a Predetermined $D$ and $M$

A common, and usually troublesome problem involves setting up two arbitrarily chosen lenses or systems to produce a specified magnification

---

[*] The methods of this paper apply just as well to systems of convex and concave mirrors, as to lenses. The Gaussian imagery of a mirror is not mathematically distinct from that of a lens. For Gaussian purposes, a mirror is represented by two principal points (coincident at the mirror vertex), and a focal length, just as in the case of a thin lens. A little care has to be taken in applying the Gardner sign convention, for the direction of the light is always the positive direction, both before and after reflection by the mirror.

$M$, when the object and the image must also be separated by a specified distance, $D$. Fig. 2 will serve to illustrate the discussion of this type of problem. The focal lengths and the principal point locations of the two lenses can be measured, or obtained from the manufacturer, but determination of the locations of the lenses in the system, either by experiment or by calculation is ordinarily difficult.

*Table 4*—Solution for Example 1 for Specified Distance $D = 11.5$ Inches and Magnification $M = \pm .40$ (I and II Represent Interchange of Order of Lenses)

| $M$ | $a$ (inches) Eq. [16] | $x_1$ (inches) Eq. [15] | Sign of Radical in Eq. [16] |
|---|---|---|---|
| | I. $f_1 = 1.277, S_1 = .049, f_2 = .624, S_2 = -.407$ (inches) | | |
| +.40 | 9.377742 | −1.761549 | Pos. |
| +.40 | 2.480258 | −7.531290 | Neg. |
| −.40 | 9.992931 | −1.232339 | Pos. |
| −.40 | 1.865069 | −11.334812 | Neg. |
| | II. $f_1 = .624, S_1 = -.407, f_2 = 1.277, S_2 = .049$ (inches) | | |
| +.40 | 9.377742 | −0.942520 | Pos. |
| +.40 | 2.480258 | −4.735285 | Neg. |
| −.40 | 9.992931 | −0.425933 | Pos. |
| −.40 | 1.865069 | −45.229521 | Neg. |

With the extended Gaussian equations at hand the difficulty is eased. First, the optical separation $a$ of the two lenses is calculated using Eq. [16]. Then the object-distance $x_1$ for the first lens is calculated using either Eq. [14] or Eq. [15]. The problem has either four real solutions or four complex solutions. The existence of four solutions stems from the general form of Eq. [16] and from the fact that its radicand is symmetrical in the focal lengths $f_1$ and $f_2$. This symmetry means that the order of the lenses in the system can be reversed without changing the distance between them, providing a new value of $x_1$ is determined. A complex solution indicates that for the given or arbitrary values of the four independent variables, the required optical system can have no physical existence, and the problem must be reformulated or abandoned. Reversal of the sign of $M$, if permitted by the conditions of the problem, increases the number of solutions to eight, and under certain circumstances may result in solutions being real instead of complex.

Table 4 sets forth the solution of a problem of this type for $D = 11.5$ inches and $M = \pm 0.40$. Values of $a$ calculated from Eq. [16] and $x_1$ calculated from Eq. [15] are shown, with the last column indicating the sign of the radical in Eq. [16]. Given quantities of $f_1$, $S_1$, $f_2$, and $S_2$ are shown, depending on the order of the two lenses in the system. The table thus presents the full set of eight real solutions that are mathematically possible, from which the most suitable practical optical solution (or solutions) may be selected.

### Example 2: Designing a Zoom Projection Optical System That Comprises Two Separated Lenses

The preliminary design of a zoom projection lens is readily carried out by assuming the projection distance $D$, the initial magnification $M$, the "zoomed" magnification $M_Z$, the initial object-distance $x_1$ (for lens $L_1$), an initial optical separation $a$ for the two lenses, and the principal point separations $S_1$ and $S_2$, as shown in Fig. 2. The focal lengths of the two lenses $L_1$ and $L_2$, can be calculated immediately from Eqs. [7] and [8]. By then using $M_Z$ (instead of $M$) in Eq. [16], the zoomed optical separation $a_Z$ is calculated for the two lenses. Then, when $a_Z$ and $M_Z$ (instead of $a$ and $M$) are used in either Eq. [14] or [15], the "zoomed" object-distance $x_{1Z}$ (for lens $L_1$) is calculated. The problem can be changed, if desired, by making $D$ also variable, while keeping $M$ either fixed or variable, without changing the basic solution procedure. The most cumbersome part of the work may be the search for a suitable set of initial values of $x_1$ and $a$, and a number of preliminary Gaussian designs may have to be worked through to find it.

*Table 5*—Solution of Example 2 Type Problem ("Zoom" Projection Lens)

| Given | Calculated |
|---|---|
| $x_1 = -1.5$ inches | $f_1$(Eq. [7]) = 2.4463 inches |
| $a = 9.0$ inches | $f_2$(Eq. [8]) = 12.8225 inches |
| $M = -600$ | $a_Z$(Eq. [16]) = 5.3359 inches |
| $M_Z = -600\sqrt{2.5}$ | $x_{1Z}$(Eq. [15]) = −1.8471 inches |
| $D = 3{,}000$ inches | |
| $S_1 = .333$ inch | |
| $S_2 = .333$ inch | |

Table 5 presents the solution of a problem of the type just discussed. The given and calculated values in Table 5 correspond roughly to the zoom projection lens used in New York's Radio City Music hall when it opened in the early 1930's.

### Example 3: Designing an Afocal Separated Two-Lens Optical System for Adjusting Focus at Fixed Magnification

From Fig. 2 and Table 1 we may write

$$M = \frac{F}{F + X}. \tag{44}$$

Also, it has been shown that

$$M = \frac{f_1 f_2}{(f_1 + f_2 - a)x_1 + f_1(f_2 - a)}. \tag{13}$$

By differentiating Eqs. [44] and [13] and then setting

$$\frac{dM}{dX} = \frac{dM}{dx_1}$$

it can be shown, upon making suitable substitutions from Table 1, etc., that

$$F = \frac{f_1 f_2}{f_1 + f_2 - a} \tag{45}$$

(Eq. [45] is a well known equation in textbooks.[1,2,6,7]) By Eq. [45], $F$ is clearly infinite, or the system afocal, when

$$f_1 + f_2 = a, \tag{46}$$

and when $a$ is eliminated between Eqs. [46] and [13]

$$M_A = -\frac{f_2}{f_1}. \; (F = \text{infinite}) \tag{47}$$

Thus, a system with an infinite focal length has a finite or absolute magnification $M_A$, that is independent of object-distance $x_1$.

The distance $D$ between object and image, however, is shown by eliminating $a$ between Eqs. [46] and [19] (and also noting Eq. [47]), to be

$$D = (M_A^2 - 1)x_1 - (M_A - 1)(f_1 + f_2) + S_1 + S_2. \; (F = \text{infinite}) \tag{48}$$

From Eq. [48], by differentiating,

$$\frac{dD}{dx_1} = (M_A^2 - 1) = \text{constant} = \frac{\Delta D}{\Delta x_1}, \tag{49}$$

or

$$M_A = \pm \sqrt{\frac{\Delta D}{\Delta x_1} + 1}. \qquad [50]$$

By eliminating $f_2$ between Eqs. [46] and [47],

$$f_1 = \frac{a}{1 - M_A}, \qquad [51]$$

and by similarly eliminating $f_1$,

$$f_2 = \frac{-aM_A}{1 - M_A}. \qquad [52]$$

In Fig. 3, a lens $L_0$ projects an image to $I_0$. It is desired to follow $L_0$ with a two-lens optical system $L_1 - L_2$ that can be shifted along axis c-c to adjust the focal position of the image without the adjustment changing the image dimensions. Eqs. [50], [51], and [52] enable such a design to be accomplished.

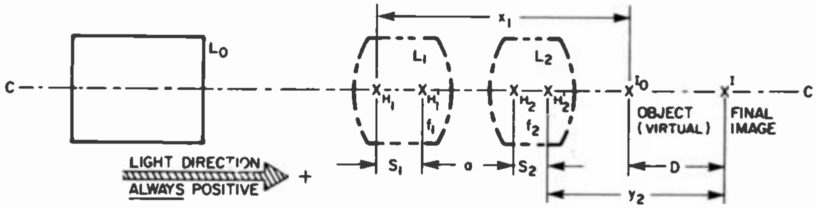

Fig. 3—Schematic diagram for afocal two-lens system to adjust focus at fixed magnification (example 3).

By letting $\Delta D/\Delta x_1$ be sufficiently small (but not zero), say equal to 0.04, Eq. [50] gives us

$$M_A = 1.019804.$$

By letting $a = 0.50$ inch, Eq. [51] gives us

$$f_1 = -25.247548 \text{ inches},$$

and Eq. [52] gives us

$$f_2 = 25.747548 \text{ inches}.$$

The values of $f_1$, $f_2$, and $a$ satisfy Eq. [46].

In order to set the focusing lens system, $L_1 - L_2$, for a required initial value of $y_2$, it is sufficient to determine the corresponding value of $D$, then solve Eq. [48] for $x_1$ and calculate the corresponding initial value of $x_1$.

From Eq. [48], by the replacements of Table 3 and suitable rearrangement,

$$D = \frac{(M_A^2 - 1)}{M_A^2} y_2 + \frac{(M_A - 1)}{M_A} (f_1 + f_2) + S_1 + S_2. \; (F = \text{infinite}) \qquad [53]$$

If the arbitrary value of $y_2$ is one inch, and $S_1 = S_2 = 0.125$ inch, then Eq. [53] gives us

$$D(\text{initial}) = 0.298171 \text{ inch.}$$

From Eq. [48], by solving for $x_1$,

$$x_1 = \frac{D + (M_A - 1)(f_1 + f_2) - S_1 - S_2}{M_A^2 - 1}, \qquad [54]$$

which then gives us

$$x_1 \,(\text{initial}) = 1.451829 \text{ inches.}$$

Thus, by using a straightforward and systematic Gaussian procedure, a compact afocal system has been designed that shifts focus without changing the image size, merely by moving the afocal combination toward or away from the image. The lens movement is greater than the focus change by the factor of twenty-five, which is reasonable.

### Example 4: Designing a Separated Two-Lens Telephoto Optical System

The first-order dimensioning of a telephoto system that comprises two separated lenses $L_1$ and $L_2$ is shown schematically in Fig. 4. The problem of the telephoto system is typically to make the ratio of the distance between the anterior vertex and the posterior principal focal point to the system focal length $F$ less than unity. This ratio can be called the telephoto "effect" $E_T$,[11] which is given an arbitrary value and kept constant for design purposes. Upon assuming the object to be at infinity, then from Fig. 4, and the definition of $E_T$ we may write

$$E_T = \frac{y_2 + a + 2S_1 + S_2}{F} = \text{constant} < 1, \qquad [55]$$

or

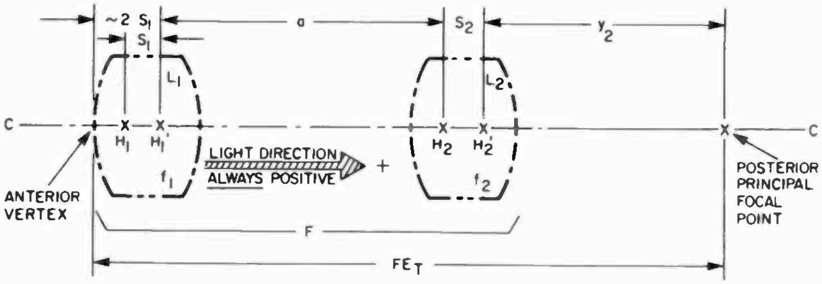

Fig. 4—Schematic diagram for a separated two-lens telephoto optical system (example 4).

$$y_2 + a = FE_T - 2S_1 - S_2 = \text{constant.} \tag{56}$$

The focal length of $L_1$ is (see Appendix 1 for derivation)

$$f_{1T} = \frac{Fa}{F(1 - E_T) + 2S_1 + S_2 + a}, \tag{57}$$

and the focal length of $L_2$ is (see Appendix 1 for derivation)

$$f_{2T} = \frac{a^2 - a(FE_T - 2S_1 - S_2)}{F(1 - E_T) + 2S_1 + S_2}. \tag{58}$$

By assigning a constant value to each quantity on the right side of Eq. [56], the values of $y_2$, $f_{1T}$, and $f_{2T}$ can be calculated for arbitrary values of the independent variable $a$. Table 6 gives calculated values for a typical set of assigned values ($F$ = 10 inches, $E_T$ = 0.5, and $S_1 = S_2$ = 0.125 inch).

(Note: For photometric reasons, no physical lens or optical system can have a "zero" focal length.)

*Table 6*—Calculated Values for Separated Two-Lens Telephoto Optical System (Example 4). Given Values: $F$ = 10 inches, $E_T$ = 0.5, and $2S_1 + S_2$ = 0.375 inches. Calculated Values in Inches (See Fig. 4 and Eqs. [56], [57], and [58]).

| $a$ | $y_2$ | $f_{1T}$ | $f_{2T}$ |
|---|---|---|---|
| 4.625 | Zero | 4.625 | Zero |
| 3.625 | 1 | 4.028 | -.674 |
| 2.625 | 2 | 3.281 | -.977 |
| 1.625 | 3 | 2.321 | -.907 |
| 0.625 | 4 | 1.042 | -.465 |
| Zero | 4.625 | Zero | Zero |

### Example 5: Designing a Separated Two-Lens Inverse Telephoto Optical System

The first-order dimensioning of an inverse telephoto, or retrofocus system that comprises two separated lenses $L_1$ and $L_2$, is shown schematically in Fig. 5. The problem of the inverse telephoto system is typically to make the ratio of the system focal length $F$ to the distance between the posterior vertex and the posterior principal focal point less than unity. This ratio can be called the (inverse) telephoto "power" $P_I$,[10]

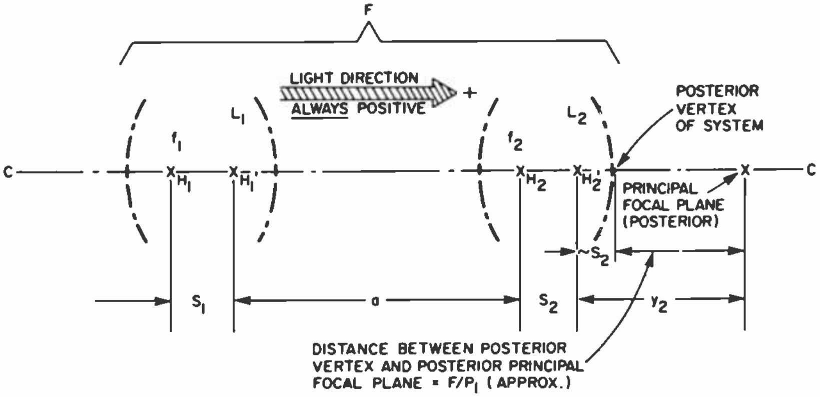

Fig. 5—Schematic diagram for a separated two-lens inverse telephoto optical system (example 5).

which is given an arbitrary value and kept constant for design purposes. Upon assuming the object to be at infinity, then from Fig. 5, and the definition of $P_I$ we may write

$$P_I = \frac{F}{y_2 - S_2} = \text{constant} < 1, \qquad [59]$$

or

$$y_2 = \frac{F}{P_I} + S_2 = \text{constant}. \qquad [60]$$

The focal length of $L_1$ is (see Appendix 2 for derivation)

$$f_{1I} = \frac{P_I F a}{F(P_I - 1) - S_2 P_I}, \qquad [61]$$

and the focal length of $L_2$ is (see Appendix 2 for derivation)

$$f_{2I} = \frac{-a(F + S_2P_I)}{F(P_I - 1) - S_2P_I - aP_I}. \qquad [62]$$

By assigning a constant value to each quantity on the right side of Eq. [60], the value of $y_2$ is determined and the values of $f_{1I}$ and $f_{2I}$ can be calculated for arbitrary values of the independent variable $a$. Table 7 presents calculated values for a typical set of assigned values.

(Note: For photometric reasons, no physical lens or optical system can have a "zero" focal length.)

*Table* 7—Calculated Values for Separated Two-Lens Inverse Telephoto Optical System (Example 5). Given Values: $F$ = 10 inches, $P_I$ = 0.5, $S_2$ = 0.125 inches. Calculated Values in Inches (See Fig. 5 and Eqs. [60], [61], and [62]).

| $a$ | $y_2$ | $f_{1I}$ | $f_{2I}$ |
|---|---|---|---|
| Zero | 15.1175 | Zero | Zero |
| 1 | 15.1175 | -0.988 | 1.809 |
| 2 | 15.1175 | -1.975 | 3.320 |
| 3 | 15.1175 | -2.963 | 4.600 |
| 4 | 15.1175 | -3.951 | 5.699 |
| 5 | 15.1175 | -4.938 | 6.653 |

### Example 6: The Principal Points of a System of Two Separated Lenses (or Systems), That Has a Specified Overall Focal Length *F*

Definite design problems arise when a system of two separated lenses is required to have not only specified principal point locations but also a specified overall focal length $F$. The problem is considered here because it offers an excellent opportunity to demonstrate a typical analytical application of the extended Gaussian equations. It will, furthermore, be useful in working out Example 7. Fig. 2 applies to the following.

By eliminating $f_2$ between Eqs. [13] and [45], and solving for $f_1$,

$$f_1 = \frac{a(Mx_1 - F)}{M(x_1 - a) + (M - 1)F}, \qquad [63]$$

and by similarly eliminating $f_1$ and solving for $f_2$,

$$f_2 = \frac{aFM}{Mx_1 + (M - 1)F}. \qquad [64]$$

When $M = +1$ in Eqs. [63] and [64],

$$f_1 = \frac{a(x_{1p} - F)}{x_{1p} - a}, \qquad [65]$$

$$f_2 = \frac{aF}{x_{1p}}. \quad [66]$$

The $p$-subscript is added to $x_1$ to denote that the terminal point of $x_1$ coincides with the first principal point H of the overall system (see Sec. 8 and Sec. 9).

By making a suitable substitution from Eq. [45] into Eq. [30]

$$D_p = \frac{-a^2F}{f_1f_2} + S_1 + S_2, \quad (M = +1) \quad [67]$$

from which

$$f_2 = \frac{-a^2F}{f_1(D_p - S_1 - S_2)}. \quad [68]$$

On eliminating $f_2$ between Eqs. [66] and [68], and solving for $f_1$,

$$f_1 = \frac{-ax_{1p}}{D_p - S_1 - S_2}. \quad [69]$$

The following substitutions are now made in Eqs. [68] and [69]:

$$x_{1p} = pF, \quad [70]$$

$$a = qF, \quad [71]$$

$$(D_p - S_1 - S_2) = rF, \quad [72]$$

as a result of which,

$$f_1 = \frac{-pqF}{r}, \quad [73]$$

$$f_2 = \frac{qF}{p}. \quad [74]$$

When Eqs. [71], [73], and [74] are substituted into Eq. [45] for $F$, $F$ cancels out and leaves the following relation between $p$, $q$ and $r$,

$$q = p + r\frac{(p-1)}{p}. \quad [75]$$

Eq. [75] is completely independent of $F$, and it furthermore expresses $q$ as a linear function of $r$ when $p$ has any constant value. This function is plotted in Fig. 6 for each of eighteen different, arbitrary numerical values of $p$.

In order to make practical application of Fig. 6, we first note that

$$p = x_{1p}/F, \qquad [76]$$

$$q = a/F, \qquad [77]$$

$$r = (D_p - S_1 - S_2)/F. \qquad [78]$$

Suppose, that for the purpose of an arbitrary example we assume

$S_1 = S_2 = +0.20$ inch

$F = +6.0$ inches

$D_p = +3.0$ inches

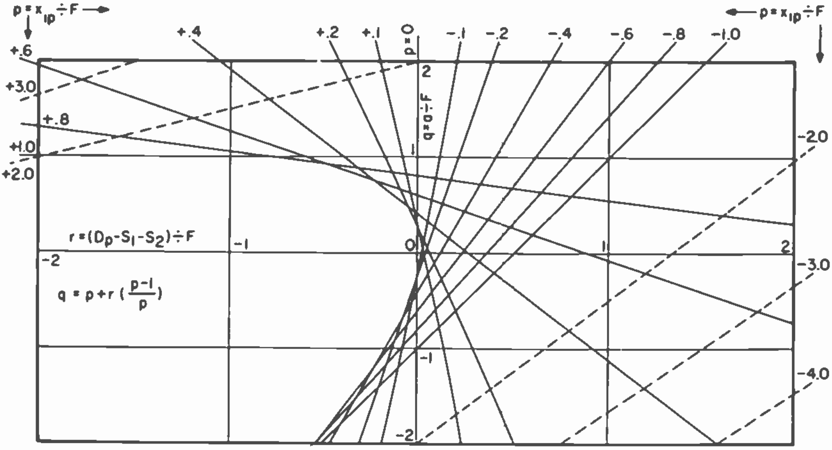

**Fig. 6**—Plot of design functions for example 6 (see Eq. [75]).

and study the practical aspects of determining suitable values of $x_{1p}$, $a$, $f_1$, and $f_2$. From Eq. [78]

$$r = \frac{3 - 0.2 - 0.2}{6} = 0.433.$$

It is likely that it will be necessary for $a$ to have positive values, from which Fig. 6 shows, that since $F$ is positive, $p$ cannot be algebraically less than about $-0.9$. Suppose we choose $p = -0.6$. Then, from Fig. 6,

$q = a/F = +.55$, and

$a = .55F = +3.30$ inches.

At the same time, by Eq. [76],

$$p = x_{1p}/F = -.6, \text{ and}$$

$$x_{1p} = -.6F = -3.60 \text{ inches.}$$

The corresponding values of $f_1$ and $f_2$, are, from Eq. [73],

$$f_1 = \frac{-(-.6)(.55)(6)}{.433} = +4.573 \text{ inches}$$

and from Eq. [74]

$$f_2 = \frac{.55(6)}{-.6} = -5.500 \text{ inches}$$

Suppose we modify the solution to keep $a$ small, by choosing $p = -.85$. Then, from Eq. [75]

$$q = -.85 + .433 \frac{-.85 - 1}{-.85} = +.0924,$$

and $a = qF = +.554$, which is a reasonably small value. The corresponding values of $f_1$ and $f_2$ are then, from Eq. [73]

$$f_1 = \frac{-(-.85)(.0924)(6)}{.433} = 1.088 \text{ inches}$$

and from Eq. [74]

$$f_2 = \frac{.0924(6)}{-.85} = -.652 \text{ inches}$$

from Eq. [70]

$$x_{1p} = pF = -.85(6) = -5.100 \text{ inches.}$$

The two calculated sets of values of $f_1$,$f_2$, and $a$ are readily checked by calculating $F$, using Eq. [45].

From the foregoing, it is obvious that a gamut of solutions exists, that are readily investigated with the help of Fig. 6 and Eqs. [70] through [78]. In the arbitrary examples studied here, both principal points are located anteriorly to the first principal point $H_1$ of the anterior lens. For some other set of $D_p$, $S_1$, $S_2$, $F$, and allowable values of $p$, the behavior of the locations of the principal points of the system may be quite different. The manner in which the separation of the two lenses is controlled is clearly indicated by the present examples.

### Example 7: Designing an Optical System to Image Two Axial Object-Points at Different Distances from The System

A system is to be designed to produce images of two object-points that are separated 2.0 inches along the system axis. One of the images is to be upright, the other inverted. The numerical magnification of one image is to be 0.40, and of the other 5.0. The choice of which image is inverted is arbitrary. The distance from either of the objects to either of the images is not to exceed +10 inches. No minimum distance, whether positive or negative, is specified.

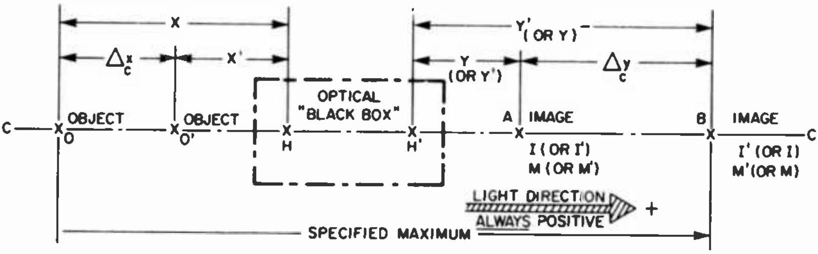

Fig. 7—Schematic diagram for judging "designability" of a proposed system with two object distances (example 7).

No explicit discussion of this type of optical system is to be found in optical books and publications, and reliance would ordinarily have to be placed on vague interpretations of whatever textbook information appears to relate to the problem.

In Fig. 7 the two objects are at 0 and 0′. One image is at A, and the other at B. On the basis of "reasonable," or "semi-educated" judgments it is assumed that 0 is imaged at A, the magnification being $M = \pm.40$, while 0′ is imaged at B, with magnification $M' = \mp 5.0$. The estimated distance from A to B is +10.58 inches. Thus we have as a proposed or submitted basis for the required optical "black-box" design:

Required:

$$X' - X = 2.0 \text{ inches} = \Delta_c x = \text{Object-space Displacement}$$

$$M = \pm.40$$

$$M' = \mp 5.0$$

Proposed:

$$Y' - Y = 10.580 \text{ inches} = \Delta_c y = \text{Image-space Displacement}$$

The problem is to design the optical "black-box."

We can easily answer the question of the possibility of such a design by consulting the conjugate displacement theorem, in the form of Eq. [41],

$$\Delta_c y = MM'\Delta_c x \qquad [41]$$

which immediately gives us

$$\Delta_c y = \pm.40(\mp 5.0)(2) = -4.0\ (\neq +10.580 \text{ inches})$$

Thus the proposed "black-box" design is optically impossible, unless the value of $Y' - Y$ is changed from $\Delta_c y = +10.580$ inches, to $\Delta_c y = -4.0$ inches. In this particular case, 0 must be imaged at B, and 0′ must be imaged at A, or the order of the image-points along the axis must be the reverse of the original assumption.

In the following discussion of the design of the separated two-lens system, Fig. 2 should also be consulted.

The focal length of the proposed optical black-box will be, by Eq. [42] or [43], respectively,

$$F = \frac{-(\pm.40)(\mp 5.0)(2)}{\mp 5.0 - (\pm.40)} = \mp.740741 \text{ inch},$$

or

$$F = \frac{-(-4.0)}{\mp 5.0 - (\pm.40)} = \mp.740741 \text{ inch},$$

It is clear from the calculated values of $F$, that its algebraic sign depends on the choice of signs of the two magnifications. The value of $\Delta_c y$ is independent of such choice.

By (I, 8) in Table 1, we may write

$$\overline{S} = D + \frac{F(1-M)^2}{M}, \qquad [79]$$

where $D = +10$ inches, $F = \mp.740741$ inch, and $M = \pm.40$. By making these substitutions into Eq. [79],

$$\overline{S}_{(M=+.4)} = 10 + \frac{-.740741(1-.4)^2}{.4} = +9.333 \text{ inches},$$

or

$$\overline{S}_{(M=-.4)} = 10 + \frac{.740741(1+.4)^2}{-.4} = +6.370 \text{ inches}.$$

We will let $M = -.40$ to make $X$ large and negative, for by (III, 8) of Table 1

$$X = \frac{F(1 - M)}{M}, \qquad [80]$$

and by making the indicated substitutions into Eq. [80],

$$X = \frac{.740741(1 + .4)}{-.4} = -2.593 \text{ inches.}$$

As a current check, $X' = -.593$ and, by (V. 2) in Table 1,

$$M' = \frac{F}{F + X'} \qquad [81]$$

or

$$M' = \frac{.740741}{.740741 - .593} = +5.014$$

which is a good rough check.

The foregoing is preliminary to the determination of $f_1$ and $f_2$, which is the central purpose of the design work. These two focal lengths cannot be determined by merely making substitutions into Eqs. [7] and [8], because a specified focal length $F = +.740741$ inch is required for the two-lens system. Nor can they be determined by a simple substitution into Eqs. [63] and [64], because a specified separation, $D_p = S = +6.370$ inches, of the principal points of the overall system is required. It is therefore proposed to proceed as in Example 6, where the work of determining $f_1$ and $f_2$ is based on the required system focal length $F$, the required separation $D_p$ of the principal points, the assumed or arbitrary location of the first principal point $H$ (of the overall system) as represented by $p$, and of course the $S_1$ and $S_2$ of the two lenses.

We start with

1. $S_1 = S_2 = +.1$
2. $F = +.740741$ inch
3. $D_p = \overline{S} = +6.370$ inches

As in Example 6, Eq. [78] gives

$$r = \frac{6.370 - .1 - .1}{.740741} = 8.329497.$$

Such values of $r$ do not appear on the graph of Fig. 6, but since $q$ (=1) is constant and independent of $r$ when $p = +1$, we will assume a trial value of $p = +1$. As a result, from Eqs. [71] and [70], respectively,

$$a = qF = F = +.740741 \text{ inch},$$

$$x_{1p} = pF = F = +.740741 \text{ inch}.$$

Finally, from Eqs. [73] and [74], respectively,

$$f_1 = \frac{-pqF}{r} = \frac{-.740741}{8.329497} = -.088930 \text{ inch}$$

$$f_2 = \frac{qF}{p} = +.740741 \text{ inch}.$$

The solution gamut is easily expanded into Table 8 by means of simple calculations based on Eqs. [70] through [76]. The restricted range of Fig. 6 does not limit this expansion. Arbitrary values are assumed for $p$, and the other quantities in the table are calculated from the equations whose numbers appear at the heads of the corresponding columns.

*Table 8*—Optical System to Image Two Axial Object Points at Different Distances from the System (Example 7) (By Eqs. [42] or [43], $F = 0.740741$ Inch; and By Eq. [78], $r = 8.329497$).

| $p$ (assumed) | $x_{1p}$ Eq. (70) | $q$ Eq. (75) | $a$ Eq. (71) | $f_1$ Eq. (73) | $f_2$ Eq. (74) | $F$ (check) Eq. (45) |
|---|---|---|---|---|---|---|
| +1.0 | .740741 | 1.000000 | .740741 | -.088930 | .740741 | .740741 |
| 1.1 | .814815 | 1.857227 | 1.375724 | -.181679 | 1.250658 | .740741 |
| 1.2 | .888888 | 2.588250 | 1.917223 | -.276207 | 1.597685 | .740741 |
| 1.3 | .962963 | 3.222192 | 2.386809 | -.372514 | 1.836007 | .740741 |

The intent here has been to illustrate the nature of an application of the extended simple Gaussian lens theory, by means of the study of a completely arbitrary problem. This intent has been accomplished, even though the choice of the problem may have led to sets of values of $a, f_1$, and $f_2$ that may not have the reassuring appearance of a practical optical system. It appears, on comparing the values of $x_{1p}$ with the value of $X'$, that 0′ of Fig. 7 is almost sure to be a virtual object-point. For $D$ (check) calculations, use Eq. [29].

It would be highly instructive to investigate the gamut of solutions that would result from adopting the rejected alternative set of conditions, namely:

$$M = +.40$$

$$F = -.740741 \text{ inch}$$

$$D_p = \overline{S} = 9.333 \text{ inch}.$$

## Example 8: Changing the Length and/or the Magnification of an Existing Optical System by Adding Two Separated Lenses

In Fig. 8(a), a lens $L_0$ produces an image at $I_0$. The object at 0 is 6.5 inches from $I_0$. It is desired to increase the length of the optical system without changing the magnification at which $L_0$ functions, while at the same time increasing the (transverse) linear dimensions of the image. In Fig. 8(b), the distance from 0 to the new and larger image at $I_0'$ is to be 8.5 inches and the new image height is to be 15% greater than originally. The distance $A$ from $L_0$ to $I_0'$ is to remain the same as $L_0$ to $I_0$. This keeps the magnification of $L_0$ unchanged.

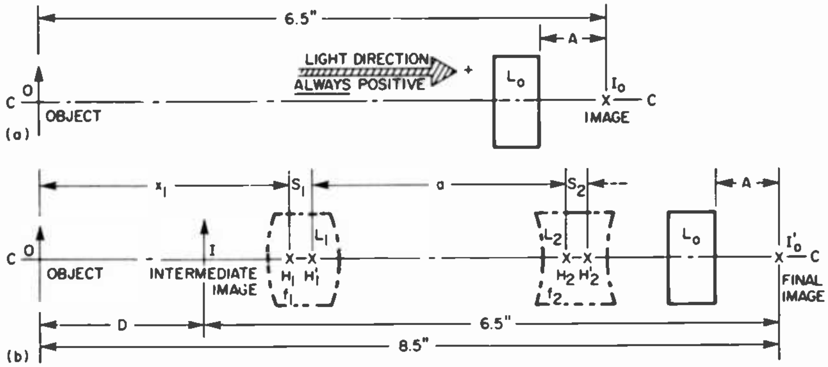

**Fig. 8**—Schematic diagram showing the effect of changing the length and/or the magnification of an existing optical system by adding two separated lenses (example 8).

The requirement will be met by placing two separated simple lenses $L_1$ and $L_2$ in the space between 0 and $L_0$ to form an intermediate image at I, and determining their focal lengths such that $D = +2$ inches and $M = +1.15$. The locations and principal point separations of the lenses are assigned arbitrarily within the limits set by the available space and the following values are chosen:

$x_1 = -3.25$ inches (arbitrary)

$a = +3.25$ inches (arbitrary)

$S_1 = S_2 = 0.125$ inches (arbitrary)

$D = +2$ inches (required)

$M = +1.15$ (required)

By Eq. [7],

$$f_1 = \frac{-Mx_1a}{(1 - M)(x_1 - a) + D - S_1 - S_2}, \qquad [7]$$

$$f_1 = \frac{-1.15(3.25)(-3.25)}{(1 - 1.15)(-3.25 - 3.25) + 2 - 0.125 - 0.125};$$

$$f_1 = +4.457569 \text{ inches.}$$

By Eq. [8],

$$f_2 = \frac{a(x_1 + D - S_1 - S_2 - a)}{(1 - M)x_1 + D - S_1 - S_2}, \qquad [8]$$

$$f_2 = \frac{3.25(-3.25 + 2 - 0.125 - 0.125 - 3.25)}{(1 - 1.15)(-3.25) + 2 - 0.125 - 0.125};$$

$$f_2 = -6.899441 \text{ inches.}$$

Substitutions into Eqs. [13] and [29] provide a good check, since the assigned value of $M = +1.15$ and $D = +2.00$ inches should result.

Ordinarily, where arbitrary choices of some of the parameters of a problem may be made, several solutions should be worked out in order to obtain the best or most suitable one.

The solution of a closely similar problem appears in the specification of United States Patent No. 2,496,069.* This is mentioned because it presents an opportunity to examine a procedure that was followed in solving the problem in 1948, before the extended Gaussian equations were available. Comparison of the complexities of the two approaches serves to indicate what has been accomplished.

## Appendix 1

From Example 4 and Fig. 4, the telephoto "effect" is defined as

$$E_T = \frac{y_2 + a + 2S_1 + S_2}{F} = \text{constant} < 1 \text{ (Eq. [55]).} \qquad [82]$$

From Fig. 2, by inspection,

$$X = x_1 - H_1H, \text{ and} \qquad [83]$$

$$Y = y_2 - H_2'H'. \qquad [84]$$

---

* L. T. Sachtleben, "Variable Length Optical System Without Change of Magnification."

In Eqs. [32] and [33], respectively,

$$H_1H\ (= x_{1p}) = \frac{f_1 a}{f_1 + f_2 - a}, \qquad [85]$$

$$H_2H'\ (= y_{2p}) = \frac{-f_2 a}{f_1 + f_2 - a}. \qquad [86]$$

Therefore, from Eqs. [83] and [85]

$$X = x_1 - \frac{f_1 a}{f_1 + f_2 - a}, \qquad [87]$$

and from Eqs. [84] and [86]

$$Y = y_2 + \frac{f_2 a}{f_1 + f_2 - a}. \qquad [88]$$

Since, by Eq. [45]

$$F = \frac{f_1 f_2}{f_1 + f_2 - a}, \qquad [89]$$

Eq. [88] may be restated as

$$Y = y_2 + \frac{Fa}{f_1}. \qquad [90]$$

When the object is at infinity ($X = \infty$), we may write from (IV, 2) in Table 1,

$$Y = \frac{FX}{F + X} = \frac{F}{\frac{F}{X} + 1} = F. \qquad [91]$$

Therefore, from Eqs. [90] and [91]

$$y_2 + \frac{Fa}{f_1} = F;\ (X = \infty) \qquad [92]$$

Solving Eq. [92] for $f_1$ gives

$$f_1 = \frac{Fa}{F - y_2}, \qquad [93]$$

and solving Eq. [89] for $f_2$ gives

$$f_2 = \frac{(f_1 - a)F}{f_1 - F}. \qquad [94]$$

Substituting the value of $f_1$ from Eq. [93] into Eq. [94] gives

$$f_2 = \frac{ay_2}{a + y_2 - F} \qquad [95]$$

Eliminating $y_2$ between Eqs. [82] and [93], and solving for $f_1$, gives

$$f_1 = f_{1T} = \frac{Fa}{F(1 - E_T) + 2S_1 + S_2 + a}, \qquad [96]$$

which is the Eq. [57] that is used in Example 4. Similarly, by eliminating $y_2$ between Eqs. [82] and [95] and solving for $f_2$,

$$f_2 = f_{2T} = \frac{a^2 - a(FE_T - 2S_1 - S_2)}{F(1 - E_T) + 2S_1 + S_2}, \qquad [97]$$

which is the Eq. [58] that is used in Example 4.

## Appendix 2

From Example 5 and Fig. 5, the (inverse) telephoto "power" is defined as

$$P_I = \frac{F}{y_2 - S_2} = \text{constant} < 1 \text{ (Eq. [59])} \qquad [98]$$

$$y_2 - S_2 = \frac{F}{P_I}. \qquad [99]$$

On rewriting Eq. [93] in the form

$$f_1 = f_{1I} = \frac{Fa}{F - (y_2 - S_2) - S_2}, \qquad [100]$$

and substituting the value of $(y_2 - S_2)$ from Eq. [99],

$$f_{1I} = \frac{P_I Fa}{F(P_I - 1) - S_2 P_I}, \qquad [101]$$

which is the Eq. [61] that is used in Example 5. On continuing in a similar manner by rewriting Eq. [95] as

$$f_2 = f_{2I} = \frac{ay_2}{a + (y_2 - S_2) - F + S_2}, \qquad [102]$$

and substituting the value of $(y_2 - S_2)$ from Eq. [99],

$$f_{2I} = \frac{-ay_2 P_I}{F(P_I - 1) - (a + S_2)P_I}. \qquad [103]$$

By then eliminating $y_2$ between Eqs. [95] and [103],

$$f_{2l} = \frac{-a(F + S_2P_l)}{F(P_l - 1) - S_2P_l - aP_l}, \qquad [104]$$

which is the Eq. [62] that is used in Example 5.

**References:**

[1] Hardy and Perrin, *The Principles of Optics*, pp. 50–61, McGraw-Hill Book Co., N.Y. (1930).

[2] D. H. Jacobs, *Fundamentals of Optical Engineering*, pp. 25–27, McGraw-Hill Book Co., N.Y. (1943).

[3] A significant comment by David Onn and Richard Berg in, "Let There be Light," *Am. J. Phys.*, **42**, p. 202 (1974) refers to the need in teaching optics to avoid the "formula" in an effort to treat "multiple lens systems and optical instruments without the confusion of the sign conventions of the professionals."!!! (!!!'s added by the referencer).

[4] I. C. Gardner, *Application of the Algebraic Aberration Equations to Optical Design*, U.S. Bureau of Standards Scientific Paper No. 550 (1927), p. 80.

[5] A. E. Conrady, *Applied Optics and Optical Design—Part One*, p. 42, Oxford Univ. Press (1929) and Dover Publications, Inc. (1957).

[6] See Ref. (1), pp. 59–61.

[7] R. S. Longhurst, *Geometrical and Physical Optics*, 2nd Edn., p. 30, John Wiley and Sons, Inc., N.Y. (1967).

[8] See Ref. (5), p. 442 and p. 449.

[9] L. T. Sachtleben, "A One-Ray System for Designing Spherical Condensers," *J. Soc. Mot. Picture Eng.*, **XXXIX**, p. 358, Dec. 1942.

[10] R. Kingslake, Ed., *Applied Optics and Optical Engineering*, **III**, p. 104, Academic Press, Inc., N.Y. (1965).

# Surface and Bulk Electrical Conduction in Low-Deposition-Temperature $Si_3N_4$ and $Al_2O_3$ Films for Silicon Devices

**Robert B. Comizzoli**

RCA Laboratories, Princeton, N.J. 08540

**Abstract**—Surface and bulk conduction of $Al_2O_3$ and $Si_3N_4$ films produced by low-temperature processes (<450°C) were measured. These properties of the deposited layers were compared with those of chemical vapor deposited $SiO_2$ and phosphosilicate glass of the type commonly used for integrated-circuit passivation. The performance and reliability implications of the electrical properties, particularly in the presence of water, are discussed, and the need for further evaluation is pointed out.

## Introduction

The overcoating of metallized integrated circuits (ICs) with insulating, protective layers is important for device reliability.[1] A widely used technique is the chemical vapor deposition (CVD) of $SiO_2$, often with phosphorus doping to form a phosphosilicate glass (PSG), over aluminum metallized IC's.[2] These layers provide scratch protection for the interconnects,[3] insulation protection against loose conducting particles in cavity packages,[4] and, when doped with phosphorus, sodium gettering capability.[5] The phosphorus addition also lowers intrinsic stress over aluminum metal.[2,5,6]

Various properties of CVD PSG layers such as stress, phosphorus content, and layer integrity[7] affect the performance of the layer as a protective overcoating. Bulk and surface electrical properties of $SiO_2$ and PSG films have been measured and related to device leakage,[8] lateral charge spreading,[9] deleterious electrolytic processes,[8,10–12] and moisture effects.[8–11,13] Also, gold dendritic growth to produce resistive shorts has been related to poor edge coverage by deposited $SiO_2$.[14,15]

Alternative passivation overcoating materials are at present under evaluation in a number of organizations. The principal ones are low-deposition-temperature $Si_3N_4$ and $Al_2O_3$. Reported advantages of the $Si_3N_4$ include alkali barrier properties and good adhesion to gold, but it should be pointed out that PSG can also be used with gold metallization.[16]

The properties of $Si_3N_4$ and $Al_2O_3$ films deposited at high temperature (>800°C) are very good, including high resistivity and effective sodium ion blocking capability,[17–22] and it is hoped that similar characteristics will exist in low-temperature films. For deposition over aluminum the deposition temperature should be no higher than about 450°C, while for gold metallization it should be limited to about 350°C. Thus, possible passivation layers include glow-discharge-formed films of $Si_3N_4$,[23–29] reactivity-sputtered $Si_3N_4$,[30] and CVD $Al_2O_3$.[31–34] Films prepared by these types of processes have been evaluated in a preliminary way in this paper.

A large amount of data exists on capacitance–voltage (CV) and bias–temperature (BT) properties of these films,[23–26,31–34] but relatively little information exists on bulk conductivity, particularly for the glow-discharge-deposited $Si_3N_4$. Also, we are unable to find any data on the surface resistivity in the presence of water, which is of extreme importance for reliability of plastic-packaged IC's.[8,10–11]

In this paper, a preliminary examination of bulk and surface electrical properties of several types of low-temperature $Si_3N_4$ and $Al_2O_3$ films is reported. Our objective is to highlight any potential problem relating to performance or reliability and define those areas needing further study.

## Materials and Procedure

$Si_3N_4$ and $Al_2O_3$ films from various sources, produced in developmental reactors, were evaluated. Film thicknesses ranged from 0.1 to about 1 μm. $Si_3N_4$* was deposited by glow discharge using both $SiH_4$–$N_2$ and $SiH_4$-$NH_3$ reactions, and by reactive sputtering of Si in $N_2$ ambient. $Al_2O_3$ films were formed by CVD at low (~400°C) and at high (~850°C) temperatures, the latter for comparison purposes. The low-temperature

---

* The stoichiometric formula is used even though for glow discharge formed silicone nitride the Si:Ni atomic ratio can vary from 0.6 to 1.5 depending on deposition conditions.

$Al_2O_3$ was formed by reaction of Al-isopropoxide in $N_2$, while the high-temperature $Al_2O_3$ was formed by reaction of $Al_2Cl_6$ with $CO_2$ and $H_2$ at 850°C.

The films were deposited on degenerately doped n-type silicon (0.01 ohm-cm) for conduction measurements. An interdigitated aluminum electrode pattern (formed by photolithography) was used for both bulk and surface conduction measurements, as previously described.[8] Bulk conduction through the film was measured using one of the surface interdigitated electrodes and the substrate as electrodes in a well-shielded probe station in dry $N_2$ ambient.[8] Surface measurements were done at 23°C as a function of relative humidity using the two surface electrodes.[8] For comparison purposes, the current levels at 1 minute after voltage application were selected for analysis. For both bulk and surface current measurements, a voltage of 100 V was applied. CV-BT measurements were done in a shielded probe station in dry argon at 1 MHz. The BT treatment always consisted of heating for 5 minutes at 220°C (with a 3 minute warm-up period); bias was 10 to 20 V depending on the sample.

Some samples were exposed to steam at 121°C, 15 psig in an autoclave to examine bulk moisture effects. These samples were dried for 5 minutes in dry $N_2$ to remove surface water, and the bulk conduction was immediately measured.

## Results

*Bulk Conduction*—For all samples, initial measurements showed that the current increased superlinearly with voltage above a certain voltage threshold, as expected.[17,35] For comparison purposes and to estimate leakage and other reliability effects on IC's, we ignore this current dependence on field and calculate a bulk conductivity from the current levels at 100 V at 23°C. These may be considered order-of-magnitude estimates useful for performance and reliability calculations. The results are shown in Table 1, where we have also included room-temperature measurements of bulk conduction after autoclave exposure. Data for PSG films[8] are also included for comparison purposes. In some cases there were large variations depending on deposition conditions; these are shown in the table as a range of values.

Measurements of bulk conduction at 100°C indicated that $Si_3N_4$ samples had thermal activation energies in the range 0.4 to 0.7 eV, and $Al_2O_3$ samples had about 0.5 eV activation energy. Previous data show CVD $SiO_2$ and PSG to have activation energies of 0.6 and 0.8 eV, respectively, before autoclave exposure.[8]

*Table 1*—Room-Temperature (23° C) Bulk Conductivity (at Fields ~$10^6$ V/cm)

| Material | Deposition Process | Bulk Conductivity $(\text{ohm-cm})^{-1}$ | Bulk Conductivity after 5 hours autoclave $(\text{ohm-cm})^{-1}$ |
|---|---|---|---|
| $Si_3N_4$ | Glow Discharge<br>$SiH_4 + NH_3$<br>Substrate $T \approx 300°C$ | $1 \times 10^{-15}$ | $0.5 \times 10^{-15}$ |
| $Si_3N_4$ | Glow Discharge<br>$SiH_4 + N_2$<br>Substrate $T \approx 300°C$ | $1 \times 10^{-6}$ to $6 \times 10^{-16}$ | No change |
| $Si_3N_4$ | React. Sputtering | $1 \times 10^{-14}$ to $7 \times 10^{-16}$ | — |
| $Al_2O_3$ | CVD, Al-isopropoxide at 450° C | $1 \times 10^{-16}$ | $5 \times 10^{-13}$ |
| $Al_2O_3$ | CVD, $AlCl_3 + CO_2 + H_2$ at 850° C | $2 \times 10^{-16}$ | — |
| $SiO_2$ | CVD, $SiH_4 + O_2$ at 450° C | $3 \times 10^{-16}$ | $2 \times 10^{-14}$ |
| PSG (5 wt % P) | CVD, $SiH_4 + O_2 + PH_3$ at 450° C | $1.5 \times 10^{-17}$ | $7 \times 10^{-14}$ |

*Surface Conduction*—The surface conduction increases with relative humidity above about 30% RH. $Al_2O_3$ has a surface resistance comparable to that of CVD PSG, while that of $Si_3N_4$ is lower. Table 2 shows values at RH = 60%, 23°C. For the $Si_3N_4$ films, it was found that the surface resistance depended more on material type and less on deposition process than did the bulk resistance, which showed large variations depending on the deposition process. Thermal $SiO_2$ has a surface resistance about equal to that of CVD $SiO_2$ at room temperature, 60% RH.[10]

*Capacitance–Voltage, Bias–Temperature, and Na Diffusion Tests*—The general approach here has been to deposit the film of interest ($Al_2O_3$ or $Si_3N_4$) over 1000 Å thick, clean thermal $SiO_2$ and measure CV-BT characteristics, using evaporated aluminum as the capacitor electrode over the $Al_2O_3$ or $Si_3N_4$. Then, the sample is wet with an $NaHCO_3$ so-

*Table 2*—Surface Resistance at 60% RH

| Material | Deposition Process | Surface Resistance (ohms/square) |
|---|---|---|
| $Si_3N_4$ | Glow Discharge | $1 \times 10^{13}$ |
| $Si_3N_4$ | React. Sputtering | $2 \times 10^{14}$ |
| $Al_2O_3$ | High and Low Temp. CVD | $2 \times 10^{15}$ |
| $SiO_2$ | CVD, $SiH_4 + O_2$ at 450°C | $2 \times 10^{14}$ |
| PSG (5 wt % P) | CVD, $SiH_4 + O_2 + PH_3$ at 450° C | $6 \times 10^{15}$ |

lution, air dried, and baked for about 4 hours at 400°C. Then, CV-BT measurements are again made.

For the thermal oxide without overcoating, the initial flat-band voltage was about −0.2 V, and the shift in flat-band voltage after the BT treatment was about −0.8 V. After the exposure to $NaHCO_3$ and 430°C bake, the flat-band voltage was about −10 V, and the BT treatment induced a shift greater than about −50 V. (The flat-band voltage was not measurable since it exceeded the oxide breakdown voltage.)

When the same measurements were done on a sample with 1000 Å of $Al_2O_3$ over the $SiO_2$, the initial flat-band voltage was about +0.2 V and the shift after BT treatment was −1.0 V. After the $NaHCO_3$ treatment, the initial flat-band voltage was unchanged at +0.2 V, but the shift after BT treatment was about −20 V.

Similar measurements were attempted with glow-discharge $Si_3N_4$ layers over thermal $SiO_2$. There were large hysteresis effects in the CV curves consistent with electron trapping at the $SiO_2$-$Si_3N_4$ interface. Initial flat band was about −4 V. The flat-band shift due to BT treatment was at least −15 V: At a voltage of −20 V on the aluminum contact, there was a sudden approximate doubling of the capacitance, after which the flat-band voltage shifted to positive values. Sodium diffusion experiments were not done because of the large shifts found without intentionally added sodium.

## Discussion

*Silicon Nitride*—The reactive-sputtering-produced $Si_3N_4$ thus far has exhibited consistently higher bulk resistivity and higher surface resistance than the glow-discharge material. However, production economy and possible radiation degradation are possible limitations to the use of sputtered passivation layers.

Of the two glow-discharge reactions, the $SiH_4 + NH_3$ process, at least in these initial tests, has shown more consistent high resistivity than the $SiH_4 + N_2$ process. A bulk resistivity of about 2–5 × $10^{12}$ ohm-cm has been reported for glow-discharge $Si_3N_4$.[23,26] For high-deposition-temperature $Si_3N_4$ films, a range of bulk resistivity values has been found, centering about $10^{14}$ to $10^{15}$ ohm-cm.[21] Both glow-discharge reactions produce films with significantly higher surface conduction than CVD $SiO_2$ or PSG layers. The reliability implications of this increased surface conduction are discussed later.

It has been reported[17,19,23] that variation in the $SiH_4$ to $NH_3$ or $N_2$ ratio has a large effect on the bulk electrical conduction. In addition, the low activation energies found in these films, about 0.5 eV versus 1.0 to 1.5 eV for high temperature $Si_3N_4$, may be related to mechanical damage whose effects have been previously described.[17] The complexity of the CV data for nitride films over $SiO_2$ is not unexpected.[19] After autoclave exposure there was no increase in conduction, suggesting excellent water resistance.

*Aluminum Oxide*—The bulk conduction of low-temperature and of high-temperature films are similar in magnitude and are in the range reported previously for aluminum contacts.[35] Exposure to steam resulted in a very large increase in conductivity. Previous reports indicate that the moisture resistance of $Al_2O_3$ films is very good.[31,32] In these previous tests, however, the films were subjected to less severe moisture environments than saturated steam at 121°C. The surface resistance of the $Al_2O_3$ in humid ambient is higher by about 100× than that of glow-discharge $Si_3N_4$ and is approximately equal to that of PSG.

Previous work[34] indicates that the flat-band voltage for 1000 Å of $Al_2O_3$ over 50 Å of thermal $SiO_2$ was about −2.0 V (for aluminum contacts), while we obtain +0.2 V for 1000 Å of $Al_2O_3$ over 1000 Å of thermal $SiO_2$. These differences may reflect varying amounts of charge at the silicon interface, or at the $SiO_2$-$Al_2O_3$ interface, or a combination of these.[36] The shifts in flat-band voltage for our sample are negative, indicating positive ion motion, while the shift for $Al_2O_3$ over very thin $SiO_2$ (50 Å) is positive,[34,36] as expected for electron trapping at the $SiO_2$-$Al_2O_3$ interface.

The sodium diffusion experiment indicates that $Al_2O_3$ is an excellent diffusion barrier, since the flat-band voltage before BT treatment was unchanged. After the BT treatment following the sodium diffusion, a large shift toward negative voltage indicates positive ion motion, presumably occurring in both the $Al_2O_3$ and $SiO_2$. However, the shift is smaller than that for the $SiO_2$ alone, which was immeasurably large. The shape of the CV curve suggested that the Na ions entered the $Al_2O_3$ from the periphery of the capacitor.

*Reliability Implications of Overcoat Electrical Conduction*—There are several important areas of IC reliability relating to overcoat or secondary-passivation-layer electrical properties and the interaction with water in plastic packages.[8,10,11] These include direct contributions to device leakage current,[8] surface inversion by surface charge migration,[9] and deleterious electrolytic processes,[8,10–12] including gold dendritic growth.[14–15]

For PSG passivation layers, reliability predictions have been made based on bulk and surface electrical properties in the presence of moisture.[8] From these results for PSG, we now extrapolate to $Si_3N_4$ and $Al_2O_3$ to highlight possible problem areas requiring further study.

Fig. 1 shows a cross-section schematic of a typical IC metallization pattern.[8] For a medium scale IC, the interconnect geometry of metal lines at low and high potential can be modeled as a pair of metal stripes 0.1 cm long, with an electrode gap of $2 \times 10^{-3}$ cm. Metal line width is $1 \times 10^{-3}$ cm. The passivation overcoating is assumed to be 5000 Å thick. The various dotted lines in Fig. 1 represent possible conduction paths between the metal lines. Path A represents direct conduction through the bulk of the passivation layer. Paths B and b in series represent the bulk and surface portions of a surface conduction path not involving openings in the passivation layer. Path b alone represents a surface path between open regions of metal. (Path c is an interface path which we ignore). Recent measurements indicate negligible conduction at the $SiO_2$-PSG interface[38] compared to bulk and surface contributions. We shall assume the same to be true of $Al_2O_3$ and $Si_3N_4$, although this must be examined in future work.

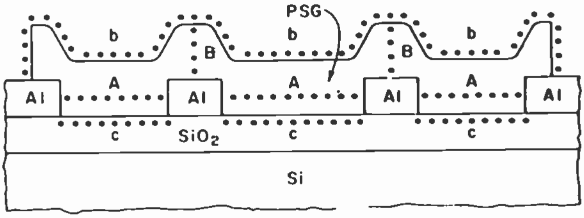

Fig. 1—Cross section of a typical IC metallized pattern with dots representing possible paths between metal lines at different voltages. (see Ref [8]).

Using the values of bulk and surface conductivity in Tables 1 and 2 we can calculate resistance values for the various paths of the assumed metallization geometry. These resistance values are shown in Table 3.

From these results it is clear that at room temperature, direct contributions to leakage current are negligible except for the most conducting samples of $Si_3N_4$, in which case the leakage currents will be hundreds of nanoamperes due to direct bulk conduction, Path A. For many applications, even this relatively large value is tolerable. At 100°C this level will rise to tenths of microamperes, which approaches the leakage limit specifications of many IC's (1–10 $\mu$A). Thus, careful control of glow-discharge $Si_3N_4$ deposition would be required to obtain higher-resistivity films.

Long-term exposure to moisture can lower resistance of conduction paths in $Al_2O_3$ and PSG films, as shown in Table 3. However, the direct contributions to leakage would remain negligible.

PSG passivation layers can have high enough surface conductivity so that surface ion migration can lead to inversion and channeling effects.[8,9] Silicon nitride layers, as shown in Tables 2 and 3, have lower surface resistance and presumably are more likely to exhibit surface ion migration. For equal thickness and other factors, the passivation layer with the higher dielectric constant will result in a structure with the higher surface inversion voltage. Thus, $Al_2O_3$ with [33]$K \approx 8$, will exhibit higher inversion voltages than either $Si_3N_4$[21] or PSG,[39] with $K = 6$ and $K = 4$, respectively. $Al_2O_3$ passivation layers, thus, will be less likely to exhibit channeling or field-inversion effects. Proper channel stoppering will prevent catastrophic failures in any case.

*Table 3*—Resistance in Ohms at 23° C of Current Paths of Fig. 1

| Material | Bulk/Path (A) | Bulk Portion of Surface Path (B) | Surface Component (b) | Total Surface Path (B + b) |
|---|---|---|---|---|
| $Si_3N_4(N_2)$, worst | $4 \times 10^{8}$ | $1 \times 10^{6}$ | $2 \times 10^{11}$ | $2 \times 10^{11}$ |
| $Si_3N_4(N_2)$, best | $7 \times 10^{11}$ | $2 \times 10^{9}$ | $2 \times 10^{11}$ | $2 \times 10^{11}$ |
| $Si_3N_4(NH_3)$ | $4 \times 10^{17}$ | $1 \times 10^{15}$ | $2 \times 10^{11}$ | $1 \times 10^{15}$ |
| $Si_3N_4$ (sputtered), worst | $4 \times 10^{14}$ | $1 \times 10^{14}$ | $4 \times 10^{12}$ | $1 \times 10^{14}$ |
| $Al_2O_3$ (both processes) | $4 \times 10^{18}$ | $1 \times 10^{16}$ | $5 \times 10^{13}$ | $1 \times 10^{16}$ |
| PSG (5 wt % P) | $3 \times 10^{19}$ | $7 \times 10^{16}$ | $1 \times 10^{14}$ | $7 \times 10^{16}$ |
| After 5 hours autoclave treatment | | | | |
| $Al_2O_3$ | $8 \times 10^{14}$ | $2 \times 10^{12}$ | $5 \times 10^{13}$ | $5 \times 10^{13}$ |
| PSG | $6 \times 10^{15}$ | $1 \times 10^{13}$ | $1 \times 10^{14}$ | $1 \times 10^{14}$ |

The importance of surface conduction in the presence of moisture has been emphasized in various failure-inducing electrolytic processes.[7,8,10,14,15] Other factors being equal, $Si_3N_4$ and, to a lesser extent, $Al_2O_3$ could be more prone to these processes than PSG. These metal-conversion or metal-transport processes depend on many factors in addition to surface conduction, such as metal-edge-coverage capability by the passivating layer, ionic content of the films and surfaces,[10] the presence of dopants such as phosphorus in the films,[11] and the general cleanliness and care used in packaging.[14,15] Enhanced conduction at the plastic–passivation-layer interface of plastic-packaged IC's may lead to rapid failure for materials with low surface resistances.[7] Thus, electrolytic failure may not necessarily result from enhanced surface conduction, but it is an area requiring further study.

Cracks and pinholes in the passivation can lead to early metallization failure when surface resistance is sufficiently low.[7,8] Thus, for a low-surface-resistance material, such as $Si_3N_4$, it is very important to maintain the layer integrity.

## Summary

Surface and bulk electrical conduction of various passivating films have been measured and compared. An assessment of reliability effects relating to these film properties shows that a critical study of surface and moisture-related reliability effects is needed to more fully assess use of $Si_3N_4$ or $Al_2O_3$ films as IC passivation layers. In particular, the greatly increased surface conduction of $Si_3N_4$ over that of PSG demands careful consideration.

## Acknowledgments

The author thanks G. L. Schnable for helpful discussions. R. Allen performed most of the electrical measurements. Various samples were provided by M. Duffy, A. Jacob, R. S. Rosler, J. Shaw, and J. Vossen. Some of the processing was done by A. W. Fisher, F. Taft, and R. Vibronek.

## References:

[1] G. L. Schnable, W. Kern, and R. B. Comizzoli, "Passivation Coatings on Silicon Devices,' *J. Electrochem. Soc.*, **122**, p. 1092, Aug. (1975).

[2] W. Kern, G. L. Schnable, and A. W. Fisher, "CVD Glass Films for Passivation of Silicon Devices: Preparation, Composition, and Stress Properties," *RCA Review*, **37**, No. 1, March (1976).

[3] L. K. Karstadt, W. G. Burger, C. M. Hsieh, and W. A. Cosgrove, "Large IC Chip Impact Analysis and Handling Protection," *Solid State Tech.*, **16**, No. 8, p. 41, Aug. (1973).

[4] W. McQuitty and C. R. Lively, "IC Failure and the Packaging Process," *Electronic Packaging and Production*, **11**, No. 11, p. 112, Nov. (1971).

[5] M. M. Schlachter, E. S. Schlegel, R. S. Keen, R. A. Lathlaen, and G. L. Schnable, "Advantages of Vapor-Plated Phosphosilicate Films in Large-Scale Integrated Circuit Arrays," *IEEE Trans Electron Devices*, **ED-17**, p. 1077 (1970).

[6] H. Sunami, Y. Itoh, and K. Sato, "Low Stress CVD Glass Films in Multilevel Interconnection," *Proc. 2nd Conf. Sol. St. Dev.*, Tokyo, 1970, Suppl. to *Japan. J. Appl. Phys.*, **40**, p. 67 (1971).

[7] "Improved CVD Techniques for Depositing Passivation Layers on IC's," Tech. Report AFML-TR-75-160, Final Report April 1974–June 1975, Air Force Materials Laboratory (LTE), Wright-Patterson AFB, Ohio 45433.

[8] R. B. Comizzoli, "Bulk and Surface Conduction in CVD $SiO_2$ and PSG Passivation Layers," *J. Electrochem. Soc.*, **123**, p. 386, March (1976).

[9] E. S. Schlegel, R. S. Keen, and G. L. Schnable, "The Effects of Insulator Surface–Ion Migration on MOS and Bipolar Integrated Circuits," *8th Ann. Proc. Reliab. Phys.*, p. 9 (1971).

[10] H. Koelmans, "Metallization Corrosion in Silicon Devices by Moisture-Induced Electrolysis," *12th Ann. Proc. Reliab. Physics*, p. 168 (1974).

[11] W. M. Paulson and R. W. Kirk, "The Effects of Phosphorus-Doped Passivation Glass on the Corrosion of Aluminum," *12th Ann. Proc. Reliab. Physics*, p. 172 (1974).

[12] S. C. Kolesar, "Principles of Corrosion," *12th Ann. Proc. Reliab. Phys.*, p. 155 (1974).

[13] R. S. Alwitt, "The Growth of Hydrous Oxide Films on Aluminum," *J. Electrochem. Soc.*, **121**, p. 1322 (1974).

[14] A. Shumka and R. R. Piety, "Migrated-Gold Resistive Shorts in Microcircuits," *13th Ann. Proc. Reliab Physics*, p. 93 (1975).

[15] F. J. Grunthaner, T. Griswold, and H. Bright, "Migratory Gold Resistive Shorts (MGRS) Failures—Chemical Aspects of a Failure Mechanism," *13th Ann. Proc. Reliab. Physics*, p. 99 (1975).

[16] H. Khajezadeh and A. S. Rose, "Reliability Evaluation of Hermetic Integrated Circuit Chips in Plastic Packages," *13th Ann. Proc. Reliab. Physics*, p. 87 (1975).

[17] G. A. Brown, W. C. Robinette, Jr., and H. G. Carlson, "Electrical Characteristics of Silicon Nitride Films Prepared by Silane-Ammonia Reaction," *J. Electrochem. Soc.*, **115**, p. 948, Sept. (1968).

[18] M. T. Duffy and W. Kern, "Preparation, Properties, and Applications of Chemically Vapor Deposited Silicon Nitride Films," *RCA Review*, **31**, p. 742, Dec. (1970).

[19] P. Balk, "Layered Dielectrics in the MOS Technology," *Solid State Devices, 1973*, Conf. Series No. 19, p. 51, Institute of Physics, (London).

[20] C. A. T. Salama, "Conduction in $Al_2O_3$ Films and Charge Storage in MAOS Structures," *J. Electrochem. Soc.*, **118**, p. 1993, Dec. (1971).

[21] J. T. Milek, "Silicon Nitride for Microelectronic Applications: Part I, Preparation and Properties," Vol. 3, *Handbook of Electronic Materials*, IFI/Plenum, New York (1971).

[22] V. Y. Doo and P. J. Tsang, "Morphology, Structure, and Properties of Pyrolytic Aluminum Oxide," Abstract No. 16, p. 33 in *Spring 1969, New York Meeting Electrochem. Soc.*, Extended Abstracts.

[23] R. C. G. Swann, R. R. Mehta, and T. P. Cauge, "The Preparation and Properties of Thin Film Silicon-Nitrogen Compounds Produced by a Radio Frequency Glow Discharge Reaction," *J. Electrochem. Soc.*, **114**, p. 713, July (1967).

[24] Y. Kuwano, "Some Properties of Silicon Nitride Films Produced by Radio Frequency Glow Discharge Reaction of Silane and Nitrogen," *Japan. J. Applied Physics*, **8**, p. 876, July (1969).

[25] R. Gereth and W. Scherber, "Properties of Ammonia—Free Nitrogen-$Si_3N_4$ Films Produced at Low Temperatures," *J. Electrochem. Soc.*, **119**, p. 1248, Sept. (1972).

[26] E. J. M. Kendall, "The Stabilization of Silicon Surfaces Using Silicon Nitride," *Brit. J. Appl. Physics (J. Phys. D)*, **1**, Series 2, p. 1409 (1968).

[27] A. R. Reinberg, "RF Plasma Deposition of Inorganic Films for Semiconductor Applications," *The Electrochem. Soc., Extended Abstracts*, **74-1**, Abstract No. 6, p. 19, May 1974.

[28] R. W. Kirk, "Applications of Plasma Technology to the Fabrication of Semiconductor Devices," Chapter 9 in *Techniques and Applications of Plasma Chemistry*, ed. J. R. Hollahan and A. T. Bell, John Wiley, New York (1974).

[29] R. S. Rosler, W. C. Benzing, and J. Baldo, "A Production Reactor for Low Temperature Plasma-Enhanced Silicon Nitride Deposition," *Solid State Tech.*, **19**, No. 6, p. 45 (1976).

[30] A. W. Stephens, J. L. Vossen, and W. Kern, "The Effect of Substrate Bias in the Properties of Reactively Sputtered Silicon Nitride," *J. Electrochem. Soc.*, **123**, p. 303, Feb. (1976).

[31] J. A. Aboaf, "Deposition and Properties of Aluminum Oxide Obtained by Pyrolytic Decomposition of an Aluminum Alkoxide," *J. Electrochem. Soc.*, **114**, p. 948, Sept. (1967).

[32] S. Krongelb, "Stability of Aluminum Oxide Films on Germanium Devices," *J. Electrochem. Soc.*, **116**, p. 1583, Nov. (1969).

[33] M. T. Duffy and A. G. Revesz, "Interface Properties of $Si-(SiO_2)-Al_2O_3$ Structures," *J. Electrochem. Soc*, **117**, p. 372, March (1970).

[34] M. T. Duffy, J. E. Carnes, and D. Richman, "Dielectric and Interface Properties of Pyrolytic Aluminum Oxide Films on Silicon Substrates," *Metall. Trans*, **2**, p. 667, March (1971).

[35] J. E. Carnes, M. T. Duffy, C. W. Mueller, D. Richman, and P. J. Zanzucchi, "Improved Dielectric Films for Semiconductor Application," Final Report, Nov. 1969–Oct. 1970, Contract No. N00019-70-C-0129, Naval Air Systems Command, Dept. of the Navy (October 1970).

[36] J. T. Clemens, E. F. Labuda, and C. N. Berglund, "Aluminum Oxide/Silicon Dioxide, Double-Insulator, MOS Structure," *The Bell Syst. Tech. J.*, **54**, p. 687 (1975).

[37] M. T. Duffy and W. Kern, "Chemical Vapor Deposition of Aluminum Oxide Films from Organo-Aluminum Compounds," *RCA Review*, **31**, p. 754 (1970).

[38] R. B. Comizzoli, unpublished results.

[39] W. Kern and R. C. Heim, "Chemical Vapor Deposition of Silicate Glasses for Use with Silicon Devices, II. Film Properties," *J. Electrochem. Soc.*, **117**, p. 562 (1970).

# Aluminum Corrosion in the Presence of Phosphosilicate Glass and Moisture*

**Robert B. Comizzoli**

RCA Laboratories, Princeton, N. J. 08540

**Abstract**—Using a test pattern typical of IC dimensions, cathodic corrosion of aluminum lines under phosphosilicate glass (PSG) layers was related to phosphorus content of the passivation glass. Little or no corrosion occurs for phosphorus concentration up to about 5 wt %. At 7.7 wt % phosphorus, serious corrosion occurs in a short time. A sequential procedure for evaluating corrosion effects in plastic packaged IC's is described, and tests using this procedure confirm previous models of corrosion. Measurement of aluminum-line resistance is used as a sensitive determinant of corrosion.

## 1. Introduction

Aluminum corrosion on IC's can be a serious reliability problem.[1-5] Cathodic corrosion of aluminum is more likely than anodic corrosion, since a protective oxide can form during the latter process.[1,2] Cathodic corrosion can occur with chemical-vapor-deposited (CVD) $SiO_2$ passivation,[3] but it is much more rapid in the presence of phosphosilicate glass (PSG).[3] Cathodic corrosion on PSG passivated IC's can be rapid at high humidity[1-4] and high phosphorus content[1,3,5] and is most severe at discontinuities in the passivating layer, such as cracks, pinholes, and bonding pads.[3-5] Bulk[4] and surface[2,4] electrical measurements of PSG layers show that in the presence of moisture the surface current between

---

* This work was in part supported by Air Force Materials Laboratory, Wright-Patterson Air Force Base, Ohio, under Contract No. F33615-74-C-5146.

discontinuities over metal in the PSG layer in IC's is much greater than the bulk current, and establish that the PSG surface electrical properties dominate the corrosion behavior. Surface conductivity in moist ambients is greater for CVD $SiO_2$ than for CVD PSG.[4] One would thus expect that aluminum corrosion would occur just as rapidly for $SiO_2$ as for PSG passivation, but this is not the case, since sufficient phosphorus must be present to take part in the corrosion chemistry[1-3] independent of the effect of phosphorus on the electrical properties. Corrosion can thus occur without phosphorus, but at much lower rates.

In this paper, further measurements of current flow between aluminum lines overcoated with CVD PSG are presented. The measurement of aluminum-line resistance is used as a measure of corrosion rate, and this rate is related to phosphorus content and water uptake, and the previous discontinuity model of corrosion is confirmed. In preliminary measurements with unencapsulated devices mounted on headers and wire bonded, we found that application of bias to aluminum patterns overcoated with PSG while in water vapor in an autoclave at 121°C, 15 psig, resulted in complete corrosion of a 1.8-$\mu$m thick, 10-$\mu$m wide line in tens of hours. This drastic corrosion was found in all layers tested, including those coated with low phosphorus content ($\sim$2 wt %) PSG and even CVD $SiO_2$. In order to find a less destructive test that would exhibit the differences known to exist depending on phosphorus content, the tests to be described were carried out. The objectives include the establishment of a useful test procedure for studying aluminum corrosion, the evaluation of various passivation layer parameters, and the correlation of previous predictions based on PSG electrical properties with test results.

## 2. Test Devices

Line patterns of aluminum on thermal $SiO_2$, overcoated with PSG layers of various composition and thickness and encapsulated in a Novolac epoxy molding compound, were used to study the corrosion. The test chips were encapsulated in 14-lead dual-in-line packages. The metal lines were $7.5 \times 10^{-2}$ cm long and had three gap widths (5.0, 7.5, and 10.0 $\mu$m). The line pattern used is shown in Fig. 1. Double layers of CVD PSG capped with CVD $SiO_2$, and triple layers of CVD $SiO_2$, CVD PSG, and CVD $SiO_2$ were studied. Phosphorus content in the PSG layers ranged from 2 to 7.7 wt %.

## 3. Results of Electrical Measurements

Two series of measurements were performed to establish relative corrosion rates. In the first series, current between line pairs at 100 V was measured at 95°C in dry nitrogen as a function of prior time in an autoclave. Results of the first series of measurements showed a large increase in current for the high-phosphorus samples. A typical result is shown in Fig. 2. Table 1 summarizes results at 35 hours autoclave exposure.

In the second series, the resistance of the aluminum lines was monitored as a corrosion-related parameter after autoclave exposure without bias, and after heat exposure (90°C) with 20-V bias applied between lines. Some line pairs were left floating. A complete cycle of line-resistance measurements in the second series consisted of the following procedure:

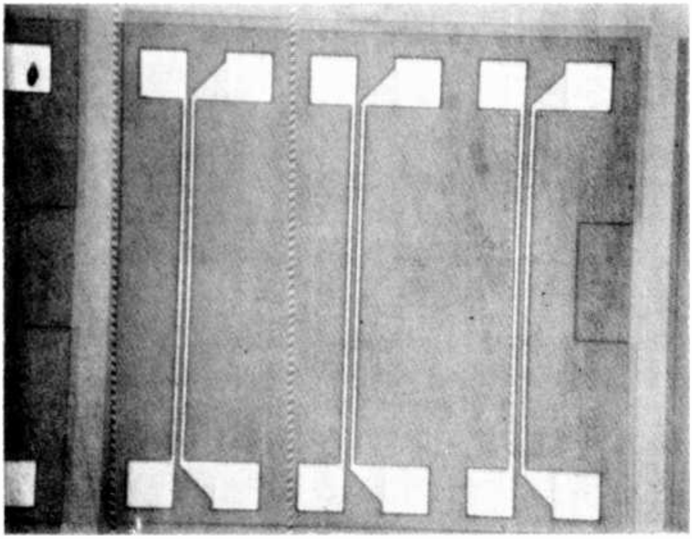

**Fig. 1**—Photomicrograph of line pattern used in corrosion study.

(1) Measure initial line resistance at 25°C.
(2) Place in autoclave at 121°C, 15 psig in vapor phase for 20 hours.
(3) Measure line resistance at 25°C.
(4) Place in room air, 90°C, with 20-V bias applied between line pairs for 5 hours.
(5) Measure line resistance at 25°C.

In the second series of measurements, it was found that the line resistance increased only after both autoclave stress and 90°C, 20-V bias were applied to a line pair. Only negatively biased lines showed the increase, and there was no increase after autoclave stress alone. A typical

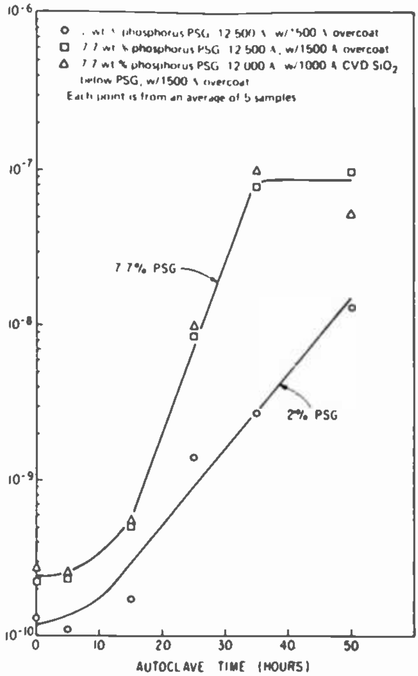

**Fig. 2**—Current (5-sample average) between aluminum line pairs 7.5 $\mu$m apart at 95°C, 100 V as a function of prior cumulative autoclave exposure. Points marked O = 2 wt % PSG of 12,500 Å thickness overcoated with 1500 Å $SiO_2$; □ = 7.7 wt % PSG of 12,500 Å thickness overcoated with 1500 Å $SiO_2$; Δ = 7.7 wt % PSG of 12,000 Å thickness with 1000 Å $SiO_2$ below PSG and 1500 Å $SiO_2$ over PSG.

*Table I*—Steady State Current between Line Pairs at 95° C, 100 V*

| | Layer Thickness (Å) | | | | |
|---|---|---|---|---|---|
| Sample No. | (1)† $SiO_2$ | (2)† PSG | (3)† $SiO_2$ | Wt % P | I (A) |
| 2A | 0 | 12,500 | 1,500 | 2.0 | $2.7 \times 10^{-9}$ |
| 1A | 0 | 12,500 | 1,500 | 2.6 | $4.2 \times 10^{-9}$ |
| 4A | 0 | 12,500 | 1,500 | 4.6 | $4.2 \times 10^{-9}$ |
| 6A | 0 | 12,500 | 1,500 | 7.7 | $7.8 \times 10^{-8}$ |
| 18A | 1,000 | 12,000 | 1,500 | 7.7 | $1.0 \times 10^{-7}$ |

*7.5-$\mu$m Line Spacing, 35-Hours Autoclave, Average of 5 Measurements.
†(1) CVD $SiO_2$ over metal, (2) CVD PSG over (1), (3) CVD $SiO_2$ over (2).

result is shown in Fig. 3 for three full cycles. Table 2 shows results at the end of three cycles for five sample types. Note the large increase in resistance for the 7.7 wt % phosphorus PSG, negative bias line.

In another experiment, the influence of phosphorus concentration and epoxy resin overcoating was determined using header-mounted CD4009A circuit metallization patterns without connection to silicon. Samples with the metal deposited on thermally grown $SiO_2$ and overcoated with PSG, (phosphorus concentrations of about 4% and 8% by weight) with and without epoxy resin overcoating, were subjected to 24 hours in an autoclave (steam, 121°C, 15 psig). Measurements of interelectrode current were then made at 60°C, dry nitrogen ambient, with 15 volts applied bias. Table 3 shows averaged values of current (in amperes) 1 minute after voltage application for 30 to 40 measurements for each entry.

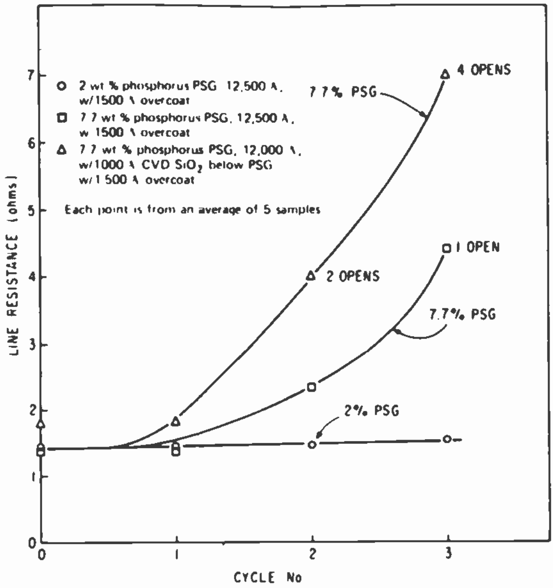

**Fig. 3**—Aluminum line resistance after three full cycles of autoclave followed by bias at 20 V at 90°C in room air. Each point is an average of 5 measurements except where open circuits occurred. Data point designations as in Fig. 2.

The current measured for the 8 wt % phosphorus PSG samples with epoxy overcoating shows a dependence on bonding pad position. That is, current is higher when the voltage is across two bonding pads that are near each other than when the pads are at opposite sides of the chip. This

*Table 2*—Aluminum-Line Resistance Values before and after Stress Testing*

| Sample† No. | Wt % P | Resistance (Ohms) of Lines for Various Bias Conditions: Floating, Initial | Floating, Final* | Positive Bias, Initial | Positive Bias, Final* | Negative Bias, Initial | Negative Bias, Final* |
|---|---|---|---|---|---|---|---|
| 2A | 2.0 | 1.537<br>1.472 | 1.534<br>1.467 | 1.531<br>1.540 | 1.541<br>1.547 | 1.474<br>1.451 | 1.542<br>1.547 |
| 1A | 2.6 | 1.481<br>1.416 | 1.474<br>1.410 | 1.502<br>1.464 | 1.503<br>1.463 | 1.505<br>1.376 | 1.541<br>1.402 |
| 4A | 4.6 | 1.494<br>1.433 | 1.491<br>1.431 | 1.505<br>1.500 | 1.510<br>1.502 | 1.455<br>1.415 | 1.512<br>1.456 |
| 6A | 7.7 | 1.459<br>1.392 | 1.458<br>1.395 | 1.475<br>1.456 | 1.477<br>1.459 | 1.420<br>1.373 | 5.216<br>4.409 |
| 18A | 7.7 | 1.889<br>1.787 | 1.889<br>1.793 | 1.903<br>1.933 | 1.918<br>1.967 | 1.796<br>1.795 | 5.980<br>6.990 |

*After 3 cycles of 20-hour autoclave followed by 5 hours at 90° C, 20 V. Average of five measurements.
†CVD layer parameters same as Table 1.

is not observed for the same PSG without an epoxy coating or for the 4 wt % phosphorus PSG with or without epoxy coating. This indicates that the enhanced conduction is due to surface conduction at the passivation glass–epoxy interface from one exposed wire bonding pad to the other. If the enhanced conduction were through the PSG bulk, there would be no dependence on pad-to-pad spacing, since the individual circuit patterns are identical. If the enhanced conduction were through the bulk of the resin, then the 4 wt % phosphorus PSG sample should also show a large increase due to the resin, but this was not found, as shown in Table 3.

## 4. Discussion and Conclusions

In these measurements the importance of phosphorus content on the corrosion rate is strongly evident. In addition, the presence of a CVD $SiO_2$ layer between the aluminum and the PSG apparently increased the corrosion rate, which is a somewhat surprising result. Also, it should

*Table 3*—Interelectrode Current at 60° C, 15V on CD4009A Patterns after Autoclave Stress

|  | Current 4 wt % P in PSG | Current 8 wt % P in PSG |
|---|---|---|
| No overcoat | $4.1 \times 10^{-12}$ | $1.3 \times 10^{-11}$ |
| With overcoat | $4.2 \times 10^{-12}$ | $6.5 \times 10^{-10}$ |

be pointed out that the current levels of Fig. 2 or Table 1 for the 7.7 wt % phosphorus PSG layers are about 20× the value calculated from the electrical properties of the PSG as described in Ref. [4]. This may be due to the presence of the encapsulating plastic as discussed (Table 3), or to conduction at the interface between the thermal oxide and the PSG. The data of Fig. 2 and Table 1 show that the electrical measurements indicate higher currents for the higher phosphorus samples. Since all the samples have a CVD $SiO_2$ top layer over the PSG, the differences must be ascribed to either bulk current contributions through the PSG, or to interactions between the plastic and the PSG at bond-pad cuts or other discontinuities. This question merits further investigation.

Assuming a Faraday efficiency of unity, degrees of aluminum corrosion based on observed or estimated currents can be made. For the line pattern used, $4.7 \times 10^{-4}$ C are needed for complete corrosion. Using the peak current of $10^{-7}$ A at 100 V (Fig. 2), a corrosion time of about 7 hours is calculated at 20 V, 90°C, assuming linear $I$-$V$ dependence. While this time agrees with data of Fig. 3, it is not suggested that uniform corrosion of the cathode takes place, since, as described later, mostly localized corrosion is found. Rather, the current decays drastically during the corrosion process.[4] Thus, as is shown in Table 2, essentially no anodic corrosion takes place, since the anode corrosion product is $Al_2O_3$, a good insulator that is stable in the absence of chloride ions. This distributes the corrosion over the entire available anode. No such limiting process occurs at the cathode, and thus, localized corrosion (at defects) leads to high resistance and open lines in the presence of high-phosphorus-content PSG.

At the present time it is not known if the large difference in corrosion rates as a function of phosphorus content as shown in Fig. 3 is due only to differences in current level, or if other factors such as varying Faraday efficiencies are involved.

Certain devices were decapsulated for microscopic examination upon completion of three full cycles. It was found that only the negative line had corroded, and that, in most cases, the corrosion was localized either at presumed defects or at bond-pad openings.

Stress-corrosion cracking[6] may be a factor in accelerating cathodic corrosion of aluminum metallization lines at grain boundaries. Aluminum-on-silicon wafers, after heat treatment at a temperature of 450°C, have been shown to be in tension at room temperature,[7] and would remain in tension under device usage conditions.

It is clear from a comparison of corrosion rates that phosphorus content up to about 5 wt % is suitable for IC's packaged in plastic. Higher phosphorus contents of about 8 wt %, however, can lead to serious corrosion in moist environments.

## Acknowledgments

I am indebted to G. L. Schnable for suggesting the measurement of line resistance as a corrosion monitor and for helpful discussions. R. E. Allen performed most of the electrical measurements and decapsulated the samples. M. Polinsky furnished the test samples.

### References:

[1] S. C. Kolesar, "Principles of Corrosion," *12th Ann. Proc. Reliability Phys.*, p. 155 (1974).

[2] H. Koelmans, "Metallization Corrosion in Silicon Devices by Moisture Induced Electrolysis," *12th Ann. Proc. Reliability Phys.*, p. 168 (1974).

[3] W. M. Paulson and R. W. Kirk, "The Effects of Phosphorus-Doped Passivation Glass on the Corrosion of Aluminum," *12th Ann. Proc. Reliability Phys.*, p. 172 (1974)

[4] R. B. Comizzoli, "Bulk and Surface Conduction in CVD $SiO_2$ and PSG Passivation Layers," *J. Electrochem. Soc.*, **123**, p. 386 (1976).

[5] W. Kern, R. B. Comizzoli, A. W. Fisher, and G. L. Schnable, "Improved Techniques for Depositing Passivation Layers on IC's," Final Report, Air Force Materials Laboratory, AFML-TR-75-160, Oct. 1975.

[6] W. W. Binger, E. H. Hollingsworth, and D. O. Sprowls, in *Aluminum, Properties, Physical Metallurgy and Phase Diagrams*, Vol. 1, pp. 209–276, K.r. Van Horn, Ed., Amer. Soc. for Metals, Metals Park, Ohio (1967).

[7] P. B. Ghate and L. H. Hall, "Internal Stresses in Multilayered Structures," *J. Electrochem. Soc.*, **119**, p. 491 (1972).

# Safe Operation of Capacitance Meters Using High Applied-Bias Voltage*

**Alvin M. Goodman**

RCA Laboratories, Princeton, N.J. 08540

**Abstract**—This paper describes a technique for using a commercial C-meter with a Bias-Isolation Unit (BIU) for capacitance measurements at bias-voltage magnitudes up to 10 kV without damage to the measurement equipment. The basic principles of operation and the details of the electrical design of a BIU are discussed. The use of the BIU imposes certain limitations on the range of sample capacitance which may be measured without introducing excessive error. The theory of these limitations is presented and compared with experimental results obtained from the use of the BIU with each of three commercially available C-meters. The measurement capability demonstrated by these results appears to be adequate for all current and future applications. For less than ±1% error in the indicated (measured) capacitance, the measurable range of the sample capacitance is found to be from 0 to at least 400 pF. In some applications, it is important to be able to accurately measure small changes in the sample capacitance; for less than ±1% error in the indicated (measured) value of a *small change*, the measurable range of the sample capacitance is found to be from 0 to at least 130 pF.

## 1. Introduction

The use of capacitance meters (C-meters) to determine small-signal (differential) capacitance as a function of applied-bias voltage is commonplace today in many research, development, and manufacturing

---

* The research described in this paper was partially funded by Advanced Research Projects Agency Order 2397 through the National Bureau of Standards' Semiconductor Technology Program Contract 5-35912 and is not subject to copyright. A version of this paper, containing mechanical details not included here, is available as NBS Special Publication 400-34.

applications. Many, if not most, of these applications are connected with the semiconductor industry. A variety of commercial instruments* is available to meet most existing measurement requirements.

Typically, an instrument of this type uses a crystal-controlled 1-MHz test signal whose amplitude is ~15 mV. The test signal is applied to the unknown capacitance; the resulting current is amplified, and its quadrature component (with respect to the applied voltage) is determined using some form of phase-locked synchronous detector. The quadrature component of the current is directly proportional to the measured capacitance, and the C-meter is usually calibrated to read directly in picofarads. In addition, an analog output voltage is generally made available to enable the plotting of capacitance on a recorder. Means are usually provided for applying a quasi-dc bias voltage to the unknown capacitance through the C-meter. This allows the capacitance to be recorded as a function of the applied-bias voltage using the arrangement shown in Fig. 1. The magnitude of the bias voltage that may be applied in this way is limited. Although the limit differs for different instruments, it is in no case greater than 600 V.

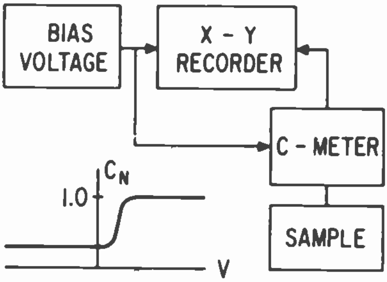

Fig. 1—Conventional high-frequency C(V) measurement. The inset is a schematic illustration of a typical plot of normalized capacitance $C_N$ versus voltage.

It is sometimes necessary to apply a bias voltage larger than 600 V to a capacitor sample.[1,2] This can be accomplished by using an arrangement which applies the bias directly to the sample but not to the C-meter. An example (based on a circuit described in Ref. [3]) is shown in Fig. 2. The isolation box allows the bias voltage to be applied to the sample while keeping it out of the C-meter; at the same time, it isolates the bias-voltage

---

[*] Some examples of commercial C-meters (or instruments containing C-meters) are BEC (Boonton Electronics Corp.) Models 71A, 71AR, 72A, 72AD, 72B, 72BD and PAR (Princeton Applied Research Corp.) Model 410.

supply from the high-frequency test signal. It is assumed that there is a dc path through the C-meter to allow the high-voltage-blocking capacitor to charge and discharge as the bias voltage is (slowly) varied. The parallel resonant circuits are tuned to the test frequency (1 MHz in this case) to provide the necessary ac isolation. This isolation can also be obtained by using sufficiently high-value resistors instead of the tuned circuits. The blocking capacitor between the sample and the C-meter must be sufficiently large that it does not introduce unacceptable error into the measurement. For the value shown (0.02 $\mu$F), the maximum error for samples with $C \lesssim 100$ pF would be $\lesssim 0.5\%$. The voltage rating of the blocking capacitor must, of course, be at least as large as the greatest anticipated bias voltage.

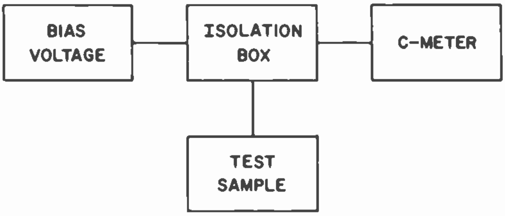

(a) BLOCK DIAGRAM

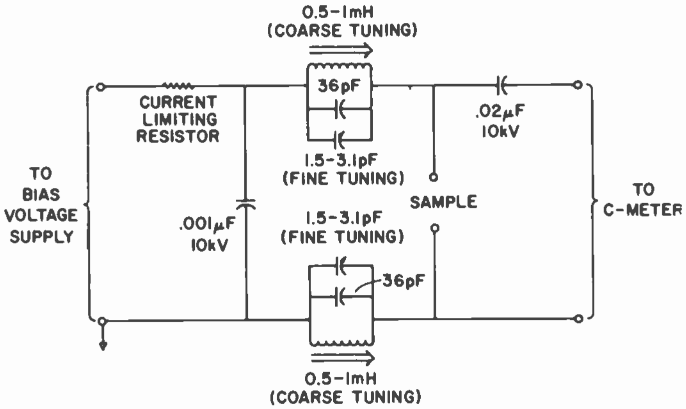

(b) ISOLATION BOX CIRCUIT

**Fig. 2**—Isolation box arrangement for measuring C(V) with an applied bias voltage larger than the C-meter limit: (a) block diagram, and (b) isolation box circuit.

The arrangement shown in Fig. 2 does not, however, provide complete protection for the C-meter in the case of sample failure. If the sample develops a short-circuit while a large bias voltage is applied to it, the blocking capacitor (which is also charged up to the bias voltage) must discharge through the C-meter. If the voltage across the blocking capacitor just before the sample "shorts" is sufficiently large, the C-meter will be damaged.

To prevent this type of damage to the C-meter, a "bias-protection circuit" has been developed. The basic principles of this circuit and some of the design considerations are discussed in Section 2. The actual circuit and operation of a C-meter "Bias-Isolation Unit" (BIU), which allows safe capacitance measurements at bias voltages up to ± 10 kV, are described in Section 3. In Section 4, some of the experimental results obtained using the BIU with commercial C-meters are presented. Finally, Section 5 discusses present and possible future applications of capacitance measurements at high applied-bias voltage.

## 2. Simplified Circuit and Principles of Operation

The operation of the C-meter bias-protection circuit can best be described by considering a simplified version: first, in the normal operating mode, as shown in Fig. 3(a), and second, the equivalent circuit after a sample "breaks down" with a large bias voltage applied to it, as shown in Fig. 3(b). The sample capacitance being measured is represented by $C_S$. The series combination of $L$ and $C_B$ is tuned to resonance (at the measurement frequency of the C-meter) so that there is no reactance in series with $C_S$. The diodes D exhibit very small capacitance and conductance at the measurement signal level (~ millivolts) and thus do not interfere with the measurement of $C_S$. The shunt capacitance and conductance of the diodes can be reduced still further by applying a small reverse bias to each of the diodes. The value of $R$ is much less than $X_{C_S}$, and its effect on the measurement of $C_S$ may be ignored in a first approximation. A detailed consideration of its effect will be presented later. The bias voltage is supplied to $C_S$ through high-value resistances ($r \gg X_{C_S}$); they serve two functions: (1) to effectively isolate the bias supply from the measurement circuit and (2) to limit the current in case of a sample breakdown (short-circuit).

The C-meter is represented by a parallel RLC circuit at the measurement frequency. There is a low-resistance dc path between the terminals of the C-meter. This allows the dc voltage at the C-meter terminal to remain effectively zero during slow variations of the applied-bias voltage. During large rapid variations of the sample bias-voltage, the voltage at the C-meter terminals would start to become significantly different from zero; one or the other of the diodes would then start to conduct heavily when biased in the forward direction. One rather important example of rapid variation of sample bias-voltage is the case in which the sample develops a short-circuit during application of a large bias voltage; the voltage across the sample drops (almost) instantaneously to zero, and $C_B$ must discharge through $R$, $L$, and the parallel combination of the diodes and the C-meter. This is illustrated schematically in Fig. 3(b). The forward resistance of the conducting diode

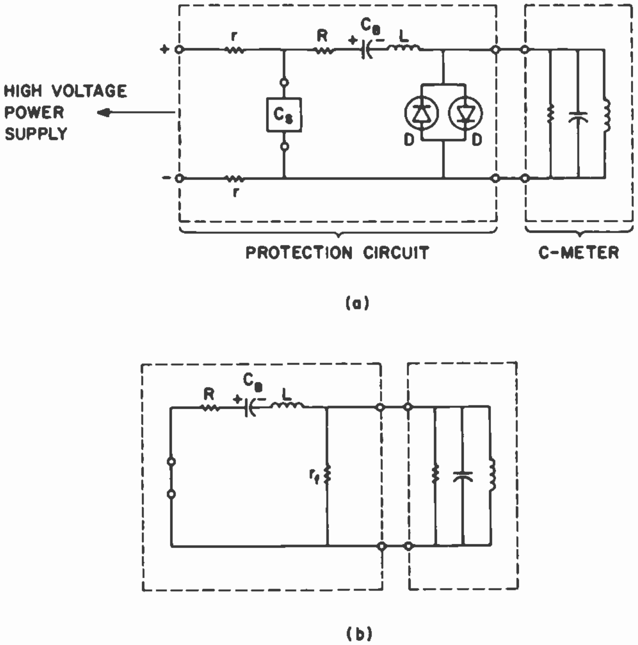

Fig. 3—Simplified version of C-meter bias-protection circuits: (a) normal operating mode and (b) after a capacitor sample breaks down with a large bias voltage applied to it.

$r_f$ must be sufficiently low that the voltage at the input terminals of the C-meter never exceeds the maximum allowable value; i.e., it remains "clamped" within some allowable range.

## 3. Actual Circuit

### 3.1 Circuit and Functional Description

The schematic circuit diagram of the C-meter bias-isolation unit (BIU) is shown in Fig. 4 and the individual circuit elements are described in Table 1. A front view of the unit is shown in Fig. 5. The circuit performs

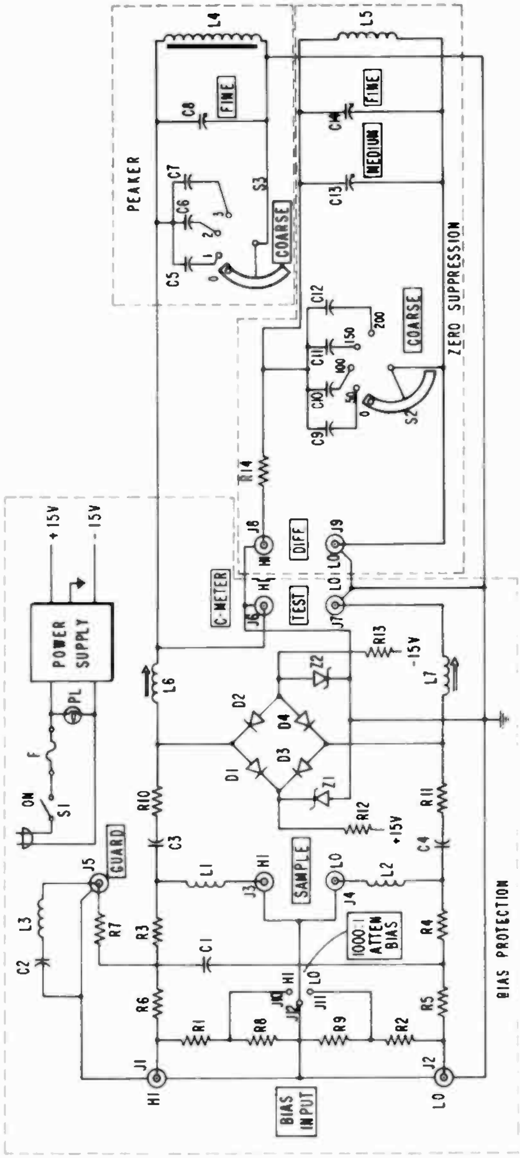

**Fig. 4**—Schematic circuit diagram of C-meter bias-isolation unit.

*Table 1*—Electrical Parts List for C-Meter Bias Isolation Unit (See Fig. 4)

| Schematic Reference | Description (Commercial description,* if appropriate, shown in parentheses) |
|---|---|
| R1, R2 | 48.8 × $10^6$-Ω nominal value, "high-voltage stable"; series string of 17 resistors: 2.87 × $10^6$ Ω, 1%, T2 (Sprague, Type 420 E, 1/2 W). |
| R3, R4 | 5 × $10^6$ Ω, 1%, 12.5 W, "high-voltage stable" (Victoreen, Type MOX-5). |
| R5, R6 | 4.7 × $10^5$ Ω, 10%, 2 W. |
| R7 | 4.7 × $10^6$ Ω, 10%, 2 W. |
| R8, R9 | 51,350-Ω nominal value. Actual values are obtained by selecting resistor combinations that will result in 1000:1 bias voltage attenuation at J10 and J11 when those terminals are shunted by the input impedance of the recorder ($10^6$ Ω). |
| R10, R11 | 25 Ω, "high-voltage stable"; series string of 25 resistors: 1 Ω, 3 W noninductive (Ohmite, Type 80173). |
| R12, R13 | 820 Ω, 10%, 2 W. |
| R14 | 51 Ω, 1%, 1/2 W, noninductive. |
| C1 | 0.01 μF, 14 kVDCW (Plastic Capacitors, Type HG 140-103). |
| C2, C3, C4 | 0.002 μF, 14 kVDCW (Plastic Capacitors, Type HG 140-202). |
| C5, C6, C7 | 36-pF silvered mica capacitor. |
| C8, C13 | 5.2–75 pF variable capacitor (E. F. Johnson, Type "L", No. 167-0004-001). |
| C9, C10, C11, C12 | 51-pF silvered mica capacitor. |
| C14 | 2.2–10 pF variable capacitor with speed-reducing planetary drive. (E. F. Johnson Type "L", No. 167-0001-001) (Jackson Brothers, Type 4511/DAF planetary ball drive with 6:1 ratio). |
| D1, D2, D3, D4 | PIN diodes (Unitrode, Type 7201D diodes). |
| L1, L2 | Special choke, 33 turns wound on 1 in. dia. × 4 in. length plastic form. |
| L3 | Special choke, ~50 turns wound on 1 in. dia. × 4 in. length plastic form to resonate with C2 at 1 MHz. |
| L4 | 145 μH, high Q choke (Boonton Electronics Corp., Type 100124). |
| L5 | 1000 μH (North Hills, Type 120K with core removed). |
| L6, L7 | 1.2 to 2.5 μH (North Hills, Type 120A with 3 turns removed leaving 12 turns remaining). |
| J1, J2, J3, J4, J5 | High voltage coaxial chassis connector (Amphenol, Type 97-3102A-18-120S). |
| J6, J7, J8, J9 | Insulated BNC coaxial chassis connector (Amphenol, Type 31-010). |
| J10, J11, J12 | Insulated banana jack. |
| S1 | SPST toggle switch. |
| S2, S3 | Ceramic insulated continuous shorting type switch (Centralab, Type PA-300 shaft and index assembly with Type PA-13 ceramic switch section). |
| Z1 | Type 1N3305B Zener diode. |
| Z2 | Type 1N3305RB Zener diode. |
| Fuse | Type 3AG-1A |
| Power Supply | Regulated with + and − 15 V outputs (Semiconductor Circuits, Type 2.15.100). |

*Designation of commercial components in this table and elsewhere in this paper does not imply recommendation or endorsement of these components, nor does it imply that they are necessarily the best available for the purpose.

not only the bias-protection function but a number of others as well; these will now be described.

### Bias-protection circuit

The high and low terminals of the output to the C-meter are individually clamped by diodes (D1 and D2 on the high side, D3 and D4 on the low side) to remain within some allowable range with respect to ground. The diodes D1 through D4 are PIN diodes with a low forward resistance, high reverse resistance, and fast turn-on. To reduce their loading effect on the C-meter, they are normally maintained at a reverse bias of 6.8 V. The bias voltages (+6.8 and −6.8 V) are provided with a very low source impedance by the Zener diodes, $Z_1$ and $Z_2$.

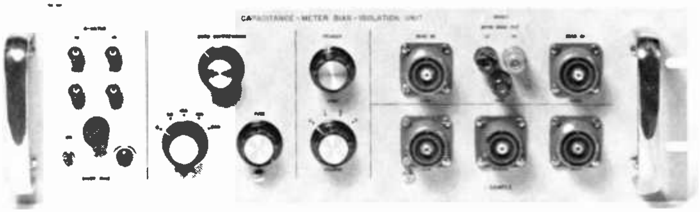

Fig. 5—Front view of capacitance-meter bias-isolation unit.

The high-voltage blocking capacitors C3 and C4 are at (or nearly at) series resonance at 1 MHz with L1 + L6 and L2 + L7, respectively. Adjustment of L6 and L7 can be used to compensate for series inductance of the connecting leads both inside and outside the BIU.

The voltage dividers formed by R1 and R8 on the HIGH side and R2 and R9 on the LOW side serve to attenuate the bias input by a factor of 1000:1 so that it may be fed directly to the X-axis of an X-Y recorder.

High-frequency noise from the bias supply is attenuated by the low-pass filter formed by R5, R6, and C1. The resistors R3 and R4 and the capacitor C1 form a filter isolating the bias supply from the 1-MHz measurement signal.

A bias voltage equal to that at the high side of the sample is available at J5 for application to a guard ring electrode. The 1-MHz series resonant circuit formed by L3 and C2 assures that the guard ring is effectively grounded at the measurement signal frequency.

### Zero adjustment and zero suppression

In order to facilitate the nulling ("cancelling out") of capacitance between the high-side and low-side test terminals, a circuit (labeled ZERO SUPPRESSION in Fig. 4) has been provided to allow a wide range of zero adjustment. This is useful not only for the usual nulling of stray capacitance due to sample holder and/or connecting leads but also for operation of the C-meter in a suppressed-zero mode as is required for "modified MIS C(V) measurements".[1,2]

The circuit consists of a variable amount of capacitive susceptance that is applied between the high side test terminal and a source of voltage* which is approximately equal to the test signal in magnitude but is 180° out of phase with it. A range of greater than 250 pF of zero suppression is available. In order that this range include "zero" (i.e., no zero suppression) the minimum value of C13 + C14 plus the stray capacitance of the wiring must be "cancelled out" by a small inductive susceptance (L5). The resistor R14 is approximately equal to the sum of R10 + R11 to minimize the phase imbalance between the signals applied to the high-side input terminal of the C-meter during operation in a suppressed-zero mode.

It is important that this circuit be ruggedly constructed in order to provide stability of the zero-suppression capacitance.

### Peaker circuit

A C-meter with a high-impedance input is sensitive to loading due to stray capacitance from the (high side) input terminal to ground. There is in the BEC Models 71A/71AR an adjustable tuned circuit that provides inductive susceptance from the high-side input terminal to ground; this circuit may be used to null (or compensate) up to about 100 pF of stray capacitance. The BIU, sample holder, and connecting cables may

---

* This voltage is available at the LO side of the terminals marked DIFF on BEC Models and at the terminal marked NULL on the PAR Model 410.

provide more stray capacitance than can be nulled by this circuit. Therefore, an additional circuit providing inductive susceptance has been built into the BIU for use if needed; it is capable of nulling up to an additional 150 pF. This portion of the circuit is labeled PEAKER in Fig. 4. In operation the PEAKER is adjusted as follows:

(1) With the cables and sample connected, the C-meter is set to its highest sensitivity (highest input impedance).

(2) The ZERO SUPPRESSION control is set to produce a reading in the upper half of the scale.

(3) The PEAKER is then adjusted to obtain a maximum reading. If the meter goes off-scale, repeat steps (2) and (3).

The peaker circuit adjustment is important only when the C-meter used has a high input impedance. If the C-meter has a low-impedance input like the PAR Model 410, its performance will be completely indifferent to adjustment of the peaker circuit.

The capacitor to be measured is connected to the terminals marked SAMPLE and the bias-voltage power supply is connected to the terminals marked BIAS INPUT. If a guard-ring electrode system is to be used on the sample, the guard ring is connected to the terminal marked GUARD and the guarded electrode must be connected to the HIGH side; the unguarded electrode is connected to the LOW side.

If the BIU is used with a BEC C-meter, the TEST and DIFF terminals of the C-meter are connected to the correspondingly marked terminals of the BIU. The external bias terminals of the C-meter should be connected together (short-circuited).

If the BIU is used with a PAR Model 410 C-meter, the HI side of the TEST and DIFF terminals of the BIU should be connected together and to the C-meter terminal marked INPUT. The LO side of the TEST and DIFF terminals of the BIU should be connected, respectively, to the C-meter terminals marked DRIVE and NULL.

## 3.2 Measurement Accuracy

### (a) Basic Considerations

The use of the BIU places certain constraints upon the range of test capacitance values that can be measured and the accuracy with which these measurements can be made. In what follows we shall first consider a simple equivalent circuit for the combination of the test capacitance and the BIU, and second derive expressions describing the deviation of the apparent or "measured" capacitance from the actual value as a function of the equivalent circuit parameters.

### (b) Equivalent circuit

The C-meter measures the capacitive susceptance of a test capacitance $C_S$ connected between its terminals and displays this value on a suitably calibrated linear scale reading directly in units of capacitance (usually pF). Let us define this value of susceptance as

$$B_0(C_S) \equiv \omega C_S. \quad [1]$$

When the C-meter is used with the BIU to measure the same test capacitance, the equivalent circuit is one in which the test capacitance appears to be in series with a resistance $R$ and (possibly) a reactance $X$. The resistance is due principally to the sum of R10 + R11 in Fig. 4. There may also be a small contribution due to the resistance in the windings of L1, L2, L6, and L7 and in the blocking capacitors C3 and C4. The reactance $X$ is equal to the difference between the inductive reactance of the sum of the circuit inductances (L1 + L2 + L6 + L7 + lead inductance) and the capacitive reactance of the series combination of C3 and C4. We shall see shortly that there is no advantage to $X$ being capacitive (negative); in practice we would like it to be either zero or slightly inductive. We shall therefore treat it as if it were due to an "excess" inductance $L_X$.

### (c) Derivation

The susceptance $B(C_S)$ of the series combination of $C_S$, $R$, and $L_X$ measured by the C-meter is

$$B(C_S) = \frac{\omega C_S[1 - \omega^2 L_X C_S]}{\omega^2 R^2 C_S{}^2 + [1 - \omega^2 L_X C_S]^2} \quad [2]$$

We may now define a relative sensitivity factor, $S(C_S)$:

$$S(C_S) \equiv \frac{B(C_S)}{B_0(C_S)} = \frac{[1 - \omega^2 L_X C_S]}{\omega^2 R^2 C_S{}^2 + [1 - \omega^2 L_X C_S]^2} \quad [3]$$

This gives the ratio of the apparent value of the $C_S$ that would be indicated by the C-meter when used with the BIU to the actual value of $C_S$ that would be indicated by the C-meter alone. In some measurement applications[1,2] it is necessary to determine small changes in a test capacitance. It is therefore of interest to derive an expression for the relative *incremental* sensitivity factor which we shall call $S'(C_S)$.

$$S'(C_S) \equiv \frac{dB(C_S)/dC_S}{dB_0(C_S)/dC_S} \quad [4a]$$

$$S'(C_S) = \frac{[1 - \omega^2 L_X C_S]^2 - \omega^2 R^2 C_S{}^2}{[(1 - \omega^2 L_X C_S)^2 + \omega^2 R^2 C_S{}^2]^2} \qquad [4b]$$

This gives the ratio of the apparent value of a small change in $C_S$ that would be indicated by the C-meter when used with the BIU to the actual value of the small change in $C_S$ that would be indicated by the C-meter alone. Ideally, of course, both $S$ and $S'$ should be equal to 1.0 for all values of $C_S$, but this could be true only for both $L_X$ and $R$ equal to zero; i.e., without the protection circuit to which $R$ is essential.

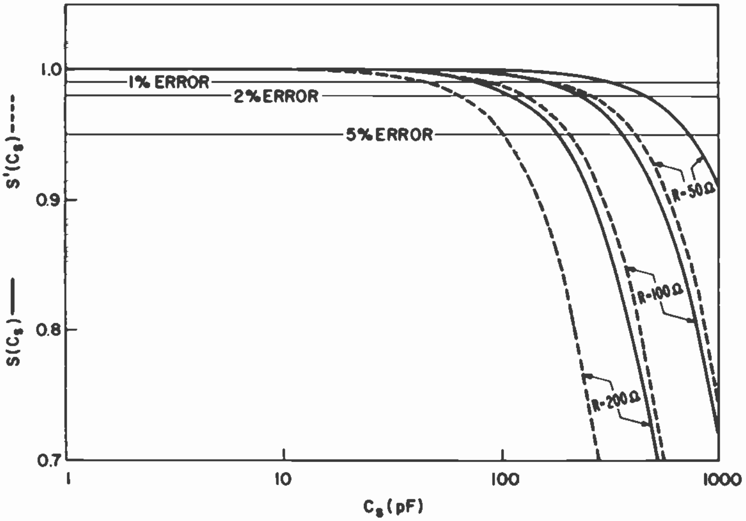

**Fig. 6**—Plots of relative sensitivity factor $S(C_S)$ and relative incremental sensitivity factor $S'(C_S)$ versus $C_S$ with series resistance $R$ as a parameter.

It is helpful to consider two separate regimes: $L_X = 0$ and $L_X \neq 0$.

(1) $L_X = 0$

In this regime, Eqs. [3] and [4b] reduce to

$$S(C_S) = \frac{1}{1 + \omega^2 R^2 C_S{}^2} \qquad [5]$$

and

$$S'(C_S) = \frac{1 - \omega^2 R^2 C_S{}^2}{[1 + \omega^2 R^2 C_S{}^2]^2} \qquad [6]$$

In Fig. 6, $S$ and $S'$ are plotted as a function of $C_S$ with $R$ as a parameter. For the value $R = 50$, it can be seen that the added error in measurement due to the BIU should be less than 1% in $S$ for $C_S \lesssim 300$ pF and less than 1% in $S'$ for $C_S \lesssim 180$ pF. These ranges of $C_S$ measurable with low added error far exceed any application requirements encountered to date.

(2) $L_X \neq 0$

It is helpful to write Eqs. [3] and [4b] in the form

$$S(C_S) = \frac{1 - \alpha C_S}{(1 - \alpha C_S)^2 + \beta C_S{}^2} \qquad [5a]$$

and

$$S'(C_S) = \frac{[1 - \alpha C_S]^2 - \beta C_S{}^2}{[(1 - \alpha C_S)^2 + \beta C_S{}^2]^2} \qquad [5b]$$

where

$$\alpha = \omega^2 L_X \quad \text{and} \quad \beta = \omega^2 R^2. \qquad [6]$$

We are particularly interested in the region in which $S(C_S)$ and $S'(C_S)$ are close to 1; i.e., the region in which $\alpha C_S \ll 1$ and $\beta C_S{}^2 \ll 1$. Eqs. [5a] and [5b] may be simplified by carrying out the indicated operations and retaining only first-order terms in $\alpha C_S$ and $\beta C_S{}^2$. This gives

$$S(C_S) \approx 1 + \alpha C_S - \beta C_S{}^2 \qquad [7a]$$

and

$$S'(C_S) \approx 1 + 2\alpha C_S - 3\beta C_S{}^2. \qquad [7b]$$

For non-zero $\alpha$, both $S(C_S)$ and $S'(C_S)$ are increasing functions of $C_S$ at low values of $C_S$, go through maxima and become decreasing functions of $C_S$. These maxima may be found by differentiating Eqs. [7a] and [7b] and setting them equal to zero. This gives

$$S(C_S)_{max} = 1 + \beta C_S{}^2 \qquad [8a]$$

$$\text{at } C_S = \alpha/2\beta \qquad [8b]$$

and

$$S'(C_S)_{max} = 1 + 3\beta C_S{}^2 \qquad [8c]$$

$$\text{at } C_S = \alpha/3\beta \qquad [8d]$$

It was previously stated that there is no advantage to the reactance $X$ being capacitive (negative); that this is true can be seen from the following argument. If the reactance were negative, the terms in Eqs. [7a] and [7b] which are linear in $C_S$ would become negative and the departure of $S(C_S)$ and $S'(C_S)$ from their ideal values of 1.00 would occur more rapidly with increasing $C_S$. This is clearly undesirable.

It is easily demonstrated that for a given allowable error *magnitude* in either $S(C_S)$ or $S'(C_S)$, a wider range of measurable $C_S$ can be obtained by using an "appropriate" value of $\alpha(L_X)$ than would be possible for $\alpha = 0$.

Let us consider two examples. First, we consider the case in which the maximum allowable error in $S(C_S)$ is $\pm\ \epsilon$. At its maximum value, $S(C_S)_{max} = 1 + \epsilon$. It follows from Eqs. [8a] and [8b] that the appropriate value of $\alpha$ is

$$\alpha(\epsilon) = 2\sqrt{\beta\epsilon}. \qquad [9]$$

The maximum value and, therefore, the maximum range of $C_S$ that can be measured without exceeding the allowable error $\epsilon$, is found from Eqs. [7a] and [9] to be

$$\Delta C_S(\alpha,\epsilon) = [1 + \sqrt{2}]\ [\epsilon/\beta]^{1/2}. \qquad [10]$$

This may be compared with the maximum range of $C_S$ that can be measured without exceeding the allowable error in $S(C_S)$ when $\alpha = 0$, i.e., when there is no excess inductance. In this case the range is

$$\Delta C_S(0,\epsilon) = [\epsilon/\beta]^{1/2}. \qquad [11]$$

Thus, the appropriate value of $\alpha$ can provide an increase in measurable range of $C_S$ by a factor of

$$\frac{\Delta C_S(\alpha,\epsilon)}{\Delta C_S(0,\epsilon)} = 1 + \sqrt{2}. \qquad [12]$$

As a second example, we consider the case in which the maximum allowable error in $S'(C_S)$ is $\pm\ \epsilon'$. At its maximum value, then, $S'(C_S) = 1 + \epsilon'$. It follows from Eqs. [8c] and [8d] that the appropriate value of $\alpha$ for this case is

$$\alpha(\epsilon') = \sqrt{3\beta\epsilon'}. \qquad [13]$$

The maximum value and, therefore, the maximum range of $C_S$ that can be measured without exceeding the allowable error $\epsilon'$ is found from Eqs. [7b] and [13] to be

$$\Delta C_S(\alpha,\epsilon') = [1 + \sqrt{2}]\ [\epsilon/3\beta]^{1/2}. \qquad [14]$$

This may be compared with the maximum range of $C_S$ that can be measured without exceeding the allowable error in $S'(C_S)$ when $\alpha = 0$, i.e., when there is no excess inductance. In this case the value is

$$\Delta C_S(0,\epsilon') = [\epsilon/3\beta]^{1/2}. \qquad [15]$$

Here again, there is an increase in the measurable range of $C_S$ by a factor of

$$\frac{\Delta C_S(\alpha,\epsilon')}{\Delta C_S(0,\epsilon')} = 1 + \sqrt{2}. \quad [16]$$

Note, however, that the "appropriate" values of $\alpha$ are not the same for equal error magnitudes $\epsilon$ and $\epsilon'$.

In summary then, excess inductance $L_X$ can be used to increase the measurable range of $C_S$ without exceeding a set of preassigned error limits on either $S(C_S)$ or $S'(C_S)$.

## 4. Experimental Results

The BIU described in Section 3 was tested to ensure that it would properly perform the desired bias-protection (transient-suppression) function and that the accuracy of measurements made with it would not be excessively degraded. These tests and their results will now be described.

### 4.1 Transient Suppression

The experimental arrangement for testing the transient-suppression capability of the BIU is shown in Fig. 7. A test capacitor periodically short-circuiting under high bias (10 kV) is simulated by a motor-driven spark gap. The resulting transient voltage at the C-meter terminals is picked up with a probe and displayed on a fast oscilloscope. The voltage from *each* C-meter terminal to ground was checked individually for each polarity of applied bias and found to have a peak value less than ± 200 V. A typical example is shown in Fig. 7(b).

In addition, repeated sample breakdowns were simulated under actual test conditions; i.e., with a C-meter connected. These tests were conducted with three different types of commercially available C-meters: (1) a BEC Model 71A, (2) a BEC Model 72AD, and (3) a PAR Model 410. The C-meters were tested before and after the simulated breakdowns; no damage or change in calibration was found.

Furthermore, many actual sample breakdowns have occurred during C(V) measurements using the BIU at high voltage levels (approaching 10 kV). In none of these breakdowns was a C-meter damaged.

### 4.2 Effect of the BIU on Measurement Accuracy

In Section 3.2 the effect of the BIU on the accuracy of C-meter measurement was considered from a theoretical point of view. The actual effect was determined experimentally by measuring $S(C_S)$ and $S'(C_S)$ for each of the three C-meters used in the transient suppression tests

(Section 4.1). Prior to these measurements L6 and L7 were adjusted to produce minimum reactance at 1 MHz between the terminals J3 and J6 and between J4 and J7 of Fig. 4. That is, there was no intentional use of excess inductance to "stretch" the measurable range of $C_S$. Some slight additional inductance was, of course, present due to the leads connecting the BIU to the C-meter and the test capacitor to the BIU.

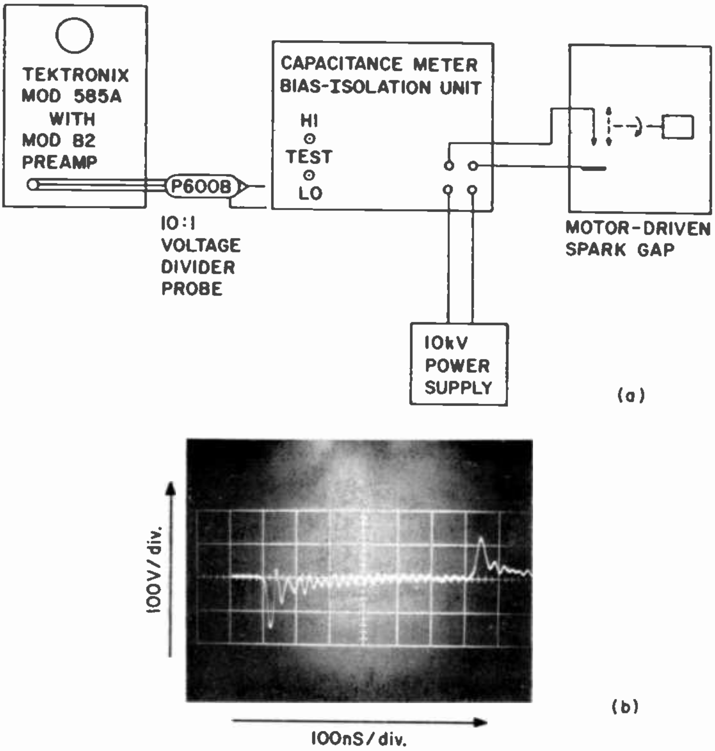

Fig. 7—(a) Schematic representation of the experimental arrangement for testing the transient suppression capability of the BIU and (b) photograph of a typical observed transient (HI terminal to ground).

In order to measure $S(C_S)$ and $S'(C_S)$, a precision decade capacitor (BEC Model 71-3A) was used as a standard. This 3-terminal capacitance standard has an accuracy of 0.25% for each of its component capacitors. In each case, the output of the C-meter was read on the 10-inch scale of an X-Y recorder with an accuracy of 0.2% of full scale. Each C-meter was calibrated on the appropriate scale(s) by connecting the standard capacitor *directly* to the C-meter (i.e., with the BIU out of the circuit) and following the manufacturer's calibration instructions.

After the completion of the calibration procedure, the standard capacitor was connected to the C-meter through the BIU, and the apparent capacitance (as measured through the BIU) was determined as a function of the standard capacitance. From Section 3.2, $S(C_S)$ = apparent value of $C_S$/standard value of $C_S$.

It was not possible to obtain $S'(C_S)$ directly. Therefore, the following approximation was used: $S'(C_S) \approx$ (measured increase in the apparent value of $C_S$ due to an actual increase of $\delta C_S)/\delta C_S$. For all of the measurements discussed in this report, $\delta C_S = 1$ pF. The actual measurement procedure was as follows: (1) a value of $C_S$ was set on the standard capacitor, (2) the output was reduced to zero using the ZERO SUPPRESSION controls, (3) the sensitivity of the recorder was increased by a factor such that an additional 1 pF should cause full scale deflection on the recorder, (4) the output was again adjusted to zero, (5) the standard capacitor was increased by 1 pF, and (6) the value of $S'(C_S)$ was read directly from the recorder with full scale corresponding to $S' = 1.00$; if the deflection exceeded full scale by more than 1% (the available recorder over-range) the sensitivity was reduced by a factor of ½, in which case half-scale deflection corresponded to $S' = 1.00$.

Measurements of apparent capacitance versus standard capacitance were carried out using each C-meter, and the value of $S(C_S)$ was computed for each data point. The results are shown in Figs. 8, 9, and 10. For comparison, the theoretical expression, Eq. [5] for $S(C_S)$ based on the simplified equivalent circuit with $L_X = 0$, is also shown in each figure. Qualitatively, the results are similar for the three C-meters, viz., the falloff of $S(C_S)$ with increasing $C_S$ is smaller than would be expected from Eq. [5] over most of the measured range of $C_S$. This occurs undoubtedly because the connecting leads provide a small excess inductance $L_X$, having the effect discussed in Section 3.2(c) ($L_X \neq 0$). This is most evident in the data for the Boonton Model 72AD C-meter (see Fig. 9), where there is a detectable peak in $S(C_S)$.

There is one other deviation from $S(C_S) = 1.00$ using the BEC Model 71A. This occurs on the lower capacitance ranges where the input resistance is high. On the 1, 3, and 10 pF scales, $S(C_S)$ was 0.892, 0.968, and 0.995, respectively, independent of $C_S$. This falloff in sensitivity is due to the loading of the input circuit by the BIU. The effect is not detectable on the 30 pF and higher capacitance ranges. The effect is not a serious one in any case, since it is independent of $C_S$ and may easily be compensated by an appropriate internal adjustment of the C-meter sensitivity on the lower scales (if the C-meter is dedicated to operation with the BIU) or, alternatively, by appropriately adjusting the recorder sensitivity. The input impedance of each of the other two C-meters tested is sufficiently low that they are not loaded by the BIU on any scale.

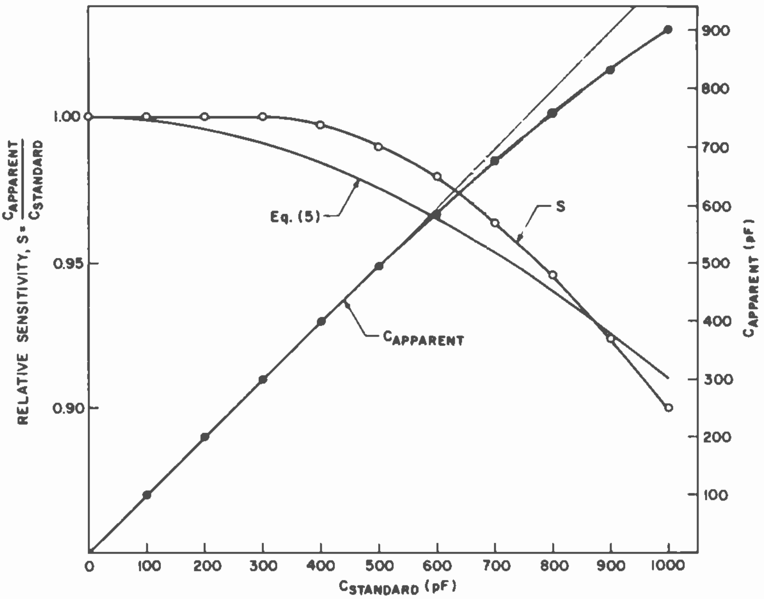

**Fig. 8**—Calibration curves for BIU operating with BEC Model 71A C-meter.

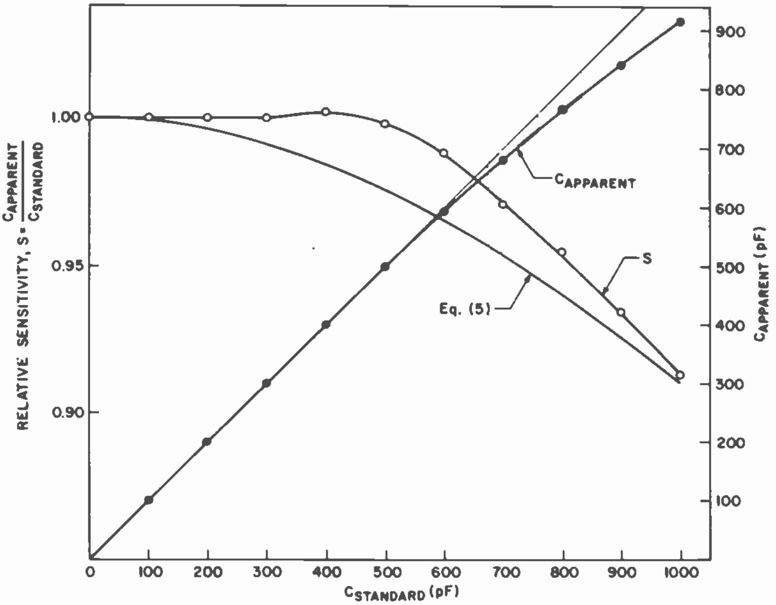

**Fig. 9**—Calibration curves for BIU operating with BEC Model 72AD C-meter.

The value of $S'(C_S)$ was then determined for each of the C-meters. The results are plotted as open circles in Figs. 11, 12, and 13. The other data in Figs. 12 and 13 will be discussed shortly. For comparison, each figure also shows the theoretical expression, Eq. [6], for $S'(C_S)$ based on the simplified equivalent circuit with $L_X = 0$. The results for the three C-meters are distinctly different in this case.

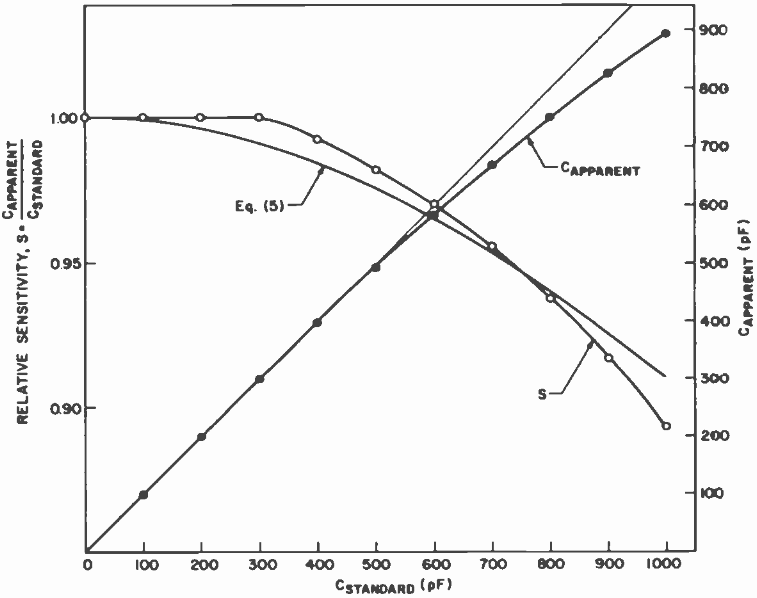

Fig. 10—Calibration curves for BIU operating with PAR Model 410 C-meter.

For the BEC Model 71A C-meter (see Fig. 11) the experimentally determined values of $S'(C_S)$ rise above 1.0 at low $C_S$ and fall below 1.0 at higher $C_S$. The initial rise is thought to be due to the excess inductance provided by the connecting leads. Above $C_S \approx 120$ pF, the experimental values of $S'(C_S)$ fall off more rapidly with increasing $C_S$ than would be expected from Eq. [6]. There are probably two reasons for this:

(1) The measurements were made using the 100-pF scale corresponding to an input resistance of approximately 60 ohms; as $C_S$ and the zero-suppression capacitance are increased, the effective capacitance from the HI terminals to ground increases, shunting the 60-ohm input resistance and lowering the apparent sensitivity of the C-meter.

(2) The effective series resistance of the BIU may be larger than 50 ohms

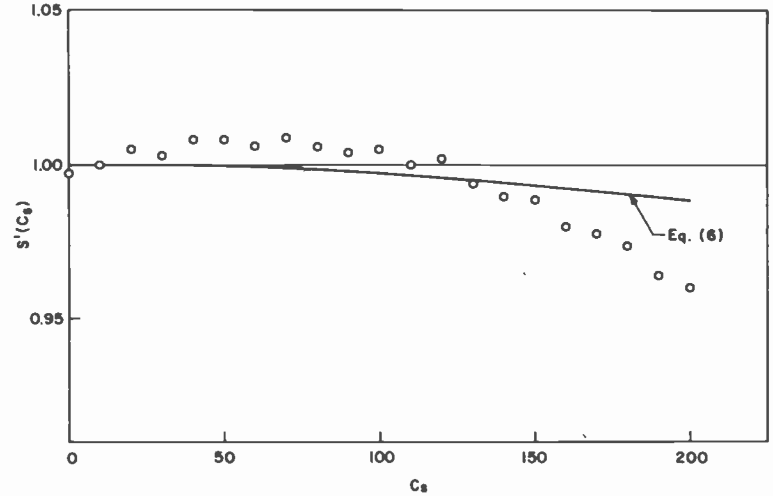

Fig. 11—Relative incremental sensitivity $S'(C_S)$ for BIU operating with BEC Model 71A C-meter.

due to the series resistance contribution of the coils and blocking capacitors.

Nevertheless, there is a measurement range of 140 pF in $C_S$ in which $S'$ does not deviate from its ideal value of 1.0 by more than 1%.

For the BEC Model 72AD C-meter (see Fig. 12), the initial experi-

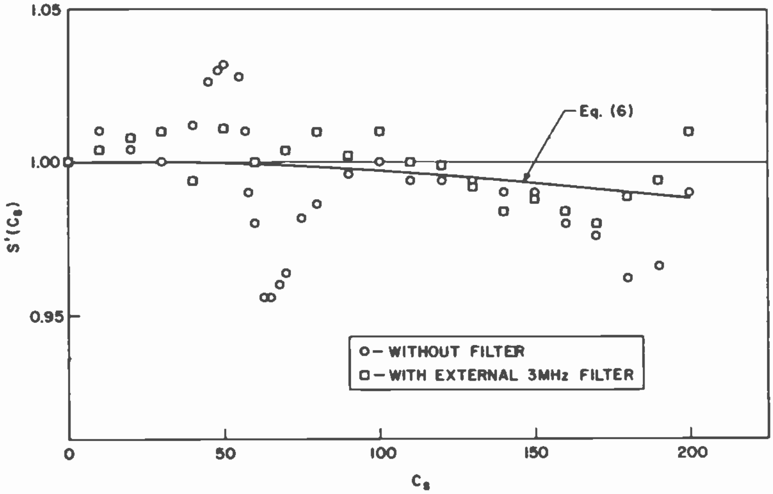

Fig. 12—Relative incremental sensitivity $S'(C_S)$ for BIU operating with BEC Model 72AD C-meter.

mental results (unfilled circles) were rather bizarre. Similar results were obtained from the initial experimental measurements (unfilled circles in Fig. 13) of $S'(C_S)$ using the PAR Model 410 C-meter. The undulation of $S'(C_S)$ suggested the possibility of resonances occurring at frequencies other than the 1-MHz test signal. An analysis of the equivalent circuit at harmonics of 1 MHz, taking into account the value of $C_S$ at which the largest undulation takes place, indicated that the major culprit was probably a third-harmonic component in the test signal. To test this hypothesis, a crude filter was assembled for use between the BIU and the C-meter (Fig. 14). The purpose of the filter was to attenuate the third-harmonic component of the current flowing from the test capacitor $C_S$ into the C-meter HI terminal. The measurements of $S'(C_S)$ were repeated for the BEC Model 72AD and PAR Model 410 C-meters using the filter. The results are shown as the squares in Figs. 12 and 13. It was clear that the filter provided a substantial improvement in the 0- to 100-pF range of $C_S$; it was equally clear that further improvement was desirable. For this reason, a spectral analysis of the test signal of each of the three C-meters was carried out using a Hewlett-Packard Model 141T Spectrum Analyzer. The results (shown in Table 2) indicate that the BEC Model 71A has the "cleanest" test signal, while the test signals

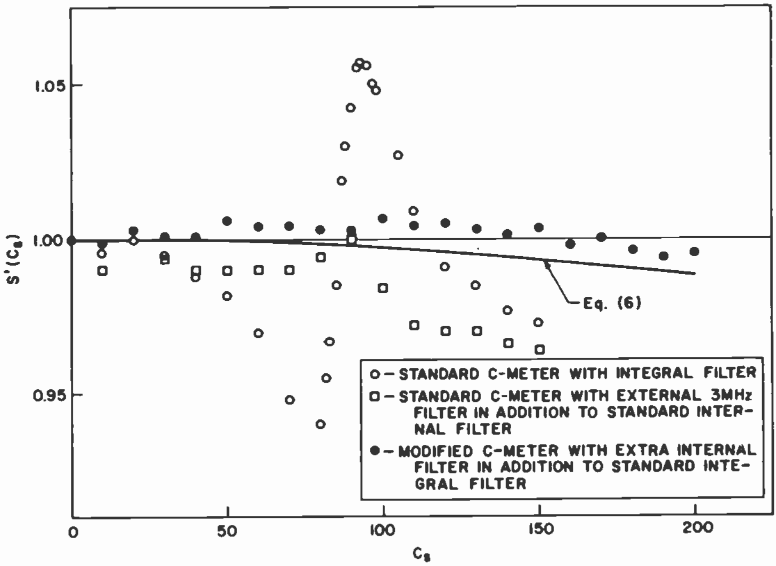

Fig. 13—Relative incremental sensitivity $S'(C_S)$ for BIU operating with PAR Model 410 C-meter.

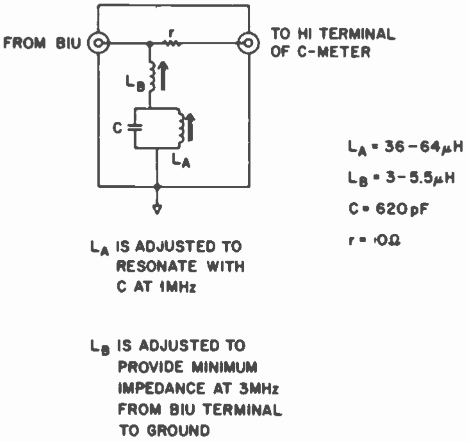

**Fig. 14**—Schematic circuit diagram of 3-MHz filter.

of the other two are relatively rich in harmonics. These results confirmed that the unexpected behavior of $S'(C_S)$ was indeed due to the presence of undesirable harmonics in the test signal.

It was felt that the best place to eliminate the harmonics was in the C-meter, either in the test signal generator or in the amplifier chain preceding the phase-sensitive detector. Accordingly, arrangements were made with the PAR Corp. to obtain a modified version of the PAR Model 410 C-meter with extra filtering to eliminate the unwanted harmonics. The results of measurement of $S'(C_S)$ using the BIU with this C-meter are shown as the filled circles in Fig. 13. The deviation of $S'(C_S)$ from 1.0 is less than 1% over the range 0 to 200 pF. The experimental points

*Table 2*—Test Signal Spectral Analysis for Three C-Meters

| | Test Signal Component ($mV_{rms}$) | | |
|---|---|---|---|
| $F$ (MHz) | BEC Mod. 71A | BEC Mod. 72AD | PAR Mod. 410 |
| 1 | 13.0 | 12.7 | 10 |
| 2 | 0.112 | 0.590 | 0.35 |
| 3 | 0.050 | 0.063 | 0.400 |
| 4 | 0.010 | 0.044 | 0.100 |
| 5 | <0.007 | 0.050 | 0.112 |
| 6 | <0.007 | 0.014 | 0.050 |
| 7 | <0.007 | 0.009 | 0.045 |
| 8 | <0.007 | 0.009 | 0.040 |
| 9 | <0.007 | 0.009 | 0.032 |
| 10 | <0.007 | 0.010 | 0.028 |

do not fall below 1.0 as rapidly with increasing $C_S$ as would be expected from Eq. [6]; this is consistent with the behavior expected from a small excess inductance provided by the connecting leads. It is reasonable to expect that similar results could be obtained using the BIU with a BEC Model 72AD C-meter suitably modified to filter out the test signal harmonics.

In summary, the tests demonstrated that the BIU can be used with any of three commercially available C-meters at applied voltages up to 10 kV. For less than ± 1% error in relative sensitivity $S(C_S)$, the measurable range of $C_S$ is from 0 to greater than 400 pF; for less than ± 1% error in relative incremental sensitivity $S'(C_S)$, the measurable range of $C_S$ is from 0 to greater than 130 pF.

## 5. Discussion and Conclusions

It is useful to consider the results that have been achieved thus far with the BIU and to place them in the broader perspective of the requirements of present and possible future applications.

The two applications of high-voltage capacitance measurements which have already been investigated in some detail are:

(1) measurements of C(V) of metal-glass-Si capacitors for the purpose of characterizing the interface between Si and a passivating glass layer ($t_{glass} \approx 10$ to 100 $\mu$m), and

(2) measurements of $C(V)$ of metal-sapphire-Si capacitors for the purpose of characterizing SOS and the Si-sapphire interface ($t_{sapphire} \approx 100$ to 150 $\mu$m).

In these applications the range of values of $C_S$ encountered was 5 to 55 pF. Clearly, the equipment described herein is entirely adequate for these measurements. It is anticipated, however, that future measurement applications (using thicker sapphire wafers) will require bias-voltage capability up to about ± 25 kV, and current efforts are directed toward the development of equipment that will be capable of operating at these higher voltage levels.

Two other applications have been investigated only in sufficient detail to show that the measurement technique is a useful one. These applications are: (1) characterization of the interface between heavily doped Si and a thick (> 1 $\mu$m) overlying insulator, (2) measurement of the base-collector capacitance of a very high voltage transistor (max $V_c \gtrsim$ 1500 V) in order to nondestructively characterize the doping profile of its base-collector region. Other possible future applications include the characterization of new passivating and encapsulating layers for semiconductor devices (e.g., plastics, resins, and epoxies), studies of the electric field dependence of dielectric polarization under high fields, and studies of dielectric-electrolyte interfaces. In each of these applications, the equipment described appears to be adequate for all current and future applications.

In conclusion, a technique has been described that allows the safe operation of commercially available C-meters for capacitance measurements with applied-bias voltage up to ± 10 kV. The technique requires a bias-isolation unit for which the circuit, theory, and practical results have been presented.

## Acknowledgments

I am indebted to Chester J. Halgas for the mechanical design and the construction of the bias-isolation unit described in this report, to Paul Kuczer for construction of an earlier developmental version, and to James M. Breece for assistance with some of the measurements.

## References:

[1] A. M. Goodman, "A Useful Modification of the Technique for Measuring Capacitance as a Function of Voltage," *IEEE Trans. Electron Devices*, **ED-21**, p. 753 (1974).

[2] A. M. Goodman, "An Investigation of the Silicon-Sapphire Interface Using the MIS Capacitance Method," *IEEE Trans. Electron Devices*, **ED-22**, p. 63 (1975).

[3] Instruction Manual for BEC Models 71A and 71AR Capacitance/Inductance Meter, Boonton Electronics Corp., Whippany, N.J.

# Compensatory Pre-emphasis

**Leonard Schiff**

RCA Laboratories, Princeton, N.J. 08540

**Abstract**—Multi-destination FDM/FM is a common transmission technique for satellite telephony. If the various receive stations have different down-link performance, the use of standard pre-emphasis will result in different SNR at each receive station. If a certain minimum SNR is specified (as is often the case), the link budget must be drawn for the poorest performing earth station and the better earth stations will have unnecessarily large margins. It is shown that the use of nonstandard and easily achieved pre-emphasis can provide equal (and just sufficient) margins at the various stations while reducing the required bandwidth and/or power of the carrier. This pre-emphasis compensates for variable downlink performance by boosting the FDM channels going to the poorer earth stations more (and those going to the better earth stations less) than standard pre-emphasis.

## 1. Introduction

The calculations for FDM/FM links and the techniques for implementing these links are based on terrestrial radio practice. But while terrestrial radio FDM/FM links are point-to-point, satellite FDM/FM links are often point-to-multipoint (or multiple destination). If the carrier-to-total noise density, $C/N_0$, is the same (or almost the same) at each destination station, the normal terrestrial implementation is reasonable. However, when the values of $C/N_0$ at the various receive stations are significantly different from one another, the use of the standard implementation is wasteful of resources—either power or bandwidth or a combination of the two. This is because this implementation corresponds to a worst-case design. In other words, the required SNR is achieved at the station with the lowest value of $C/N_0$ and the stations with higher $C/N_0$ achieve higher SNR (more than needed).

Compensatory pre-emphasis is a technique for having all stations reach their required SNR without any being overdesigned. This is achieved by implementing an effective pre-emphasis that compensates for higher (lower) $C/N_0$ by using lower (higher) pre-emphasis.

Section 2 presents the standard model for an FDM/FM system. In Section 3, this model is used to derive the savings obtained by compensatory pre-emphasis with normal loading (defined as the multiplex arrangement in the FDM baseband in which the channels lowest in the baseband go to earth stations with the lowest value of $C/N_0$). In Section 4, we consider reverse loading and show that the savings are much less. Both the results of Sections 3 and 4 are for modifications of parabolic pre-emphasis. In Section 5, the results of modification of constant-plus-parabola pre-emphasis are contrasted with parabolic and the results are shown to be similar.

## 2. Model

An FM receiver with carrier-to-noise density $C/N_0$ (assuming additive white gaussian noise) has an output parabolic noise spectrum given by*

$$N(f) = k^2 f^2 \left(\frac{C}{N_0}\right)^{-1} \text{volt}^2/\text{Hz}$$

for frequencies, $f$, between 0 and half the rf bandwidth. The constant $k$ is the demodulator gain. Any voice channel, of bandwidth $b$ Hz, located at frequency $f$ will then have noise power of $k^2 f^2 (C/N_0)^{-1} b$ (assuming $f^2 \approx (f+b)^2$). Further, let a 1 mW test tone at the reference point produce an rms frequency deviation of $f_r$ at the transmitter. The test tone's power at the output of the demodulator is then $k^2 f_r^2$ and the test-tone-to-noise ratio, $TT/N$, is given by

$$TT/N = \left(\frac{C}{N_0}\right) \frac{1}{b} \left(\frac{f_r}{f}\right)^2. \qquad [1]$$

Further, the rf bandwidth would be given by 2

$$B = 2f_m + 2pg\,f_r = 2f_m \left[1 + pg\frac{f_r}{f_m}\right]. \qquad [2]$$

---

* See any text on FM, e.g., Ref. [1].

The above is a version of Carson's rule where $f_m$ is the highest modulating frequency ($\approx Nb$ where $N$ is the number of voice channels) and $pgf_r$ is the approximate "peak" deviation. This approximation is obtained by first relating the rms frequency (voltage) of an FDM group of $N$ channels to the rms frequency (voltage) of any one through the loading factor* $g$. Secondly, one approximates this multiplex group as a Gaussian signal (central limit theorem) with flat power spectrum between 0 and $f_m$. Finally, one assumes a peaking factor $p$ relating peak and rms of a Gaussian signal where $p = 3.16$ (i.e., 10-dB peaking factor).

All the above holds without pre-emphasis. If now a pre-emphasis network is inserted between multiplexer and FM transmitter having magnitude transfer function $H(f)$ and $H^2(f) = P(f)$, the rms frequency deviation produced by a 1-mW test tone is $f_r\sqrt{P(f)}$ if the test tone is at frequency $f$. Hence, the $TT/N$ for a voice channel of bandwidth $b$ at baseband frequency position $f$ is given by

$$TT/N = \left(\frac{C}{N_0}\right)\frac{1}{b}\left(\frac{f_r}{f}\right)^2 P(f). \qquad [3]$$

The $TT/N$ is, in general, a function of the frequency the voice channel occupies.

Since the $H(f)$ without pre-emphasis is unity between frequency 0 and $f_m$, we can, without loss of generality, impose the normalizing condition

$$\int_0^{f_m} P(f)df = \int_0^{f_m} 1 \cdot df = f_m. \qquad [4]$$

With the adoption of this normalization, we can argue that the bandwidth result given by Eq. [2] still holds. The reasoning is that, because of Eq. [4], any input to the pre-emphasis filter having flat power spectrum has the same power out as it has in. Hence the rms frequency deviation of the multiplexed group is $gf_r$ as it was without pre-emphasis. Further, since a Gaussian input to any linear device (e.g., pre-emphasis filter) produces a Gaussian output, the same peaking factor $p$ can be assumed.

The above is a sketch of the standard assumptions and model for FDM/FM. In the next two sections, we shall derive results for "ideal" pre-emphasis (parabolic). For this case, $P(f) = Af^2$, in order that the $TT/N$ for all voice channels be equal. Use of Eq. [4] gives $A = 3/f_m{}^2$. Substitution into Eq. [3] gives

---

* The CCIR recommendation for $g$ is $g = 10^{-3/4}\sqrt{N}$ for $N \geq 240$ and $g = 10^{-1/20}N^{1/5}$ for $N \leq 240$.

$$TT/N = \left(\frac{C}{N_0}\right)\frac{1}{b}\left(\frac{f_r}{f_m}\right)^2 3. \qquad [5]$$

This result is slightly different than the standard CCIR recommended formula because the standard CCIR pre-emphasis is constant plus parabolic. The differences are discussed in Section 5.

## 3. Normal Loading

If there are $M$ receiving earth stations, order them in increasing $C/N_0$ so that for the $i$th station the carrier-to-noise density ratio is $(C/N_0)_i$ where $(C/N_0)_1 \leq (C/N_0)_2 \leq \ldots \leq (C/N_0)_M$. Further, let the number of circuits destined for the $i$th station be $N_i$ and the total number of circuits $N$, therefore, given by $N = \Sigma_{i=1}^{M} N_i$. The test tone-to-noise ratio at the $i$th station is given by

$$(TT/N)_i = \left(\frac{C}{N_0}\right)_i \frac{1}{b}\left(\frac{f_r}{f}\right)^2 P(f), \qquad [6]$$

and, in general depends on the exact frequency position the voice channel occupies in the baseband. If one uses the "ideal" pre-emphasis with no compensation for the different values of $C/N_0$, then $P(f) = 3(f/f_m)^2$ and

$$(TT/N)_i = \left(\frac{C}{N_0}\right)_i \frac{1}{b}\left(\frac{f_r}{f_m}\right)^2 3.$$

All the voice channels at the $i$th station have the same value of $TT/N$ but the values differ from one station to the next. Since the 1st station has the lowest value and since it is assumed that all stations have the same required value of test tone-to-noise ratio $(TT/N)_{req}$, $f_r$ must be chosen such that

$$(TT/N)_{req} = \left(\frac{C}{N_0}\right)_1 \frac{1}{b}\left(\frac{f_r}{f_m}\right)^2 3, \qquad [7]$$

and the rf bandwidth is then given by Eq. [2].

With compensatory pre-emphasis, a new pre-emphasis function is chosen. We assume normal loading, by which we mean that the lowest group of circuits in the FDM baseband $N_1$ go to station 1, the next group of circuits $N_2$ go to station 2, . . . , with the highest frequency $N_M$ channels going to station $M$. The pre-emphasis function is now given by

$$P(f) = a_i f^2, \;\; \xi_{i-1} f_m \leq f \leq \xi_i f_m \qquad [8a]$$

where

$$\xi_i = \frac{1}{N}\sum_{j=1}^{i} N_j \text{ and } \xi_0 \equiv 0. \tag{8b}$$

The $M$ constants $a_i$ are chosen such that

$$\frac{a_i}{a_1} = \frac{(C/N_0)_1}{(C/N_0)_i}. \tag{9}$$

Further, the constants are such that the normalizing condition of Eq. [4] is satisfied. Upon substituting Eqs. [8] and [9] into Eq. [4], one solves for $a_1$

$$a_1 = \frac{3}{f_m{}^2}\frac{1}{\delta}, \tag{10a}$$

where

$$\delta = \sum_{i=1}^{M} \frac{(C/N_0)_1}{(C/N_0)_i}\left[\xi_i{}^3 - \xi_{i-1}{}^3\right]. \tag{10b}$$

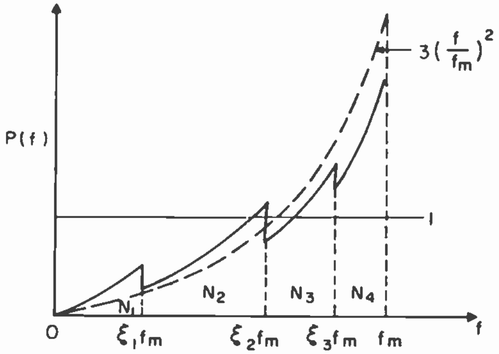

**Fig. 1.**—Pre-emphasis function for compensatory pre-emphasis with normal loading.

The pre-emphasis function given by Eq. [8] is sketched in Fig. 1 for the case $M = 4$. As can be seen, each segment is parabolic in shape with constant $a_i$ (as given by Eq. [9]) inversely proportional to $(C/N_0)_i$. Stations with lower $C/N_0$ are boosted more (and stations with higher $C/N_0$ less) than in the case of "ideal" noncompensatory pre-emphasis. The shape of the curve also demonstrates the reason this type of channel arrangement is called normal. For, when compared to any other arrangement, it produces a power spectrum at the output of the pre-emphasis network with lowest mean frequency, i.e., the power spectrum is squeezed toward the low frequency end. On a purely intuitive base, this should result in an improvement since (all other things being equal) it should reduce the rf bandwidth. In the next section, we consider the exact opposite type of loading and show that the improvement is much less.

With $a_1$ given by Eq. [10] and all other $a_i$ ($i = 2,3, \ldots, M$) given by Eq. [9], the function $P(f)$ is known, and using Eq. [6] the $TT/N$ for each of the $N_i$ circuits received at the $i$th station is given by

$$(TT/N)_i = \left(\frac{C}{N_0}\right)_i \frac{1}{b} f_r^{\,2} a_i$$

$$= \left(\frac{C}{N_0}\right)_1 \frac{1}{b} f_r^{\,2} a_1$$

$$= \left(\frac{C}{N_0}\right)_1 \frac{1}{b} \left(\frac{f_r}{f_m}\right)^2 \frac{3}{\delta} \qquad [11]$$

When this result is compared with Eq. [7], one observes that *all voice circuits* at *all stations* have the same value of $TT/N$ and this value is $1/\delta$ as much as the required value. Further, since the pre-emphasis filter used satisfies the normalizing condition of Eq. [4] and $f_r$ is unchanged, the bandwidth is exactly the same as in the noncompensatory case. This means that the carrier power to each station can be reduced to a value $\delta$ times as much to achieve the required $TT/N$ with compensatory pre-emphasis while using the same bandwidth.* Alternatively, if one wants to use the same power and reduce the bandwidth, observation of Eq. [11] shows that $f_r$ can be reduced to the value $\sqrt{\delta}\, f_r$ and still produce the test tone-to-noise ratio $(TT/N)_{req}$ at each station (see Eq. [7]). Hence use of compensatory pre-emphasis with the same carrier power can reduce bandwidth by a factor of $[1 + p{\cdot}g\sqrt{\delta}\, f_r/f_m]/[1 + p{\cdot}g\, f_r/f_m]$. Obviously, one can also achieve combinations of bandwidth and power reduction.

In order to gain some appreciation for the gains achieved in compensatory pre-emphasis, consider the case of two destinations where $(C/N_0)_1/(C/N_0)_2 = \rho \leq 1$. Substituting in Eq. [10b], we have the simple result

$$\delta = \rho + (1 - \rho)\xi_1^{\,3}. \qquad [12]$$

In Fig. 2, we plot (solid curves) the gain of compensatory pre-emphasis ($-10 \log_{10}\delta$) as a function of the fraction of circuits ($\xi_1$) going to the poorer earth station with $\rho$ (or $10 \log_{10}\rho$) as a parameter. The results are better than linear. In other words, the curve is always above the straight line segment between the value of gain at $\xi_1 = 0$ and $\xi_1 = 1$. Notice also

---

* Assuming, of course, that the resulting reduction still produced a carrier-to-noise in rf band that is over threshold.

that the results in Fig. 2 can be used as a lower bound on the gain for the case of more than two stations. That is, if the $C/N_0$ for the stations $i = 3,4, \ldots M$ are set equal to $(C/N_0)_2$, the gain is as in Fig. 2, and this value is certainly less than or equal to the actual gain since $(C/N_0)_i \geq (C/N_0)_2$, for $i \geq 3$.

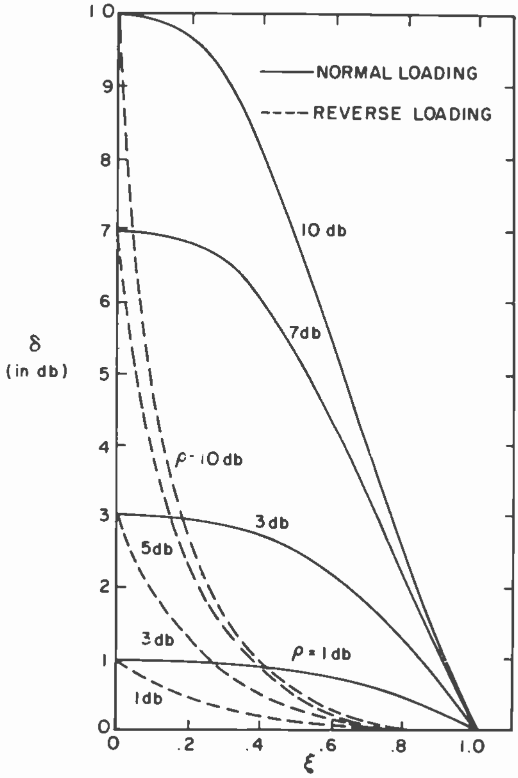

Fig. 2—Gain in compensatory pre-emphasis versus fraction of circuits destined for poorer earth station.

One final point that must be made in connection with the pre-emphasis filter is its construction. One does not attempt to synthesize a filter with the form of Eq. [8]. One rather uses a filter for which $|H(f)|^2 = f^2$ (or in the case of Section 5, constant $+ f^2$) and adjusts the gains of the individual channels to form the effect of Eq. [8]. These gain adjustments for voice channels and groups of channels are normally present in any case. In other words, in all cases the effect of compensatory pre-emphasis is achieved by forming an FDM baseband with nonconstant power spectral density (the power spectrum looking like a "staircase" function) and inputing this signal to a standard pre-emphasis filter. The effect is exactly the same as having a constant power spectrum signal fed into a compensatory pre-emphasis filter (such as in Eq. [8]) which is more convenient to treat mathematically.

## 4. Reverse Loading

In the previous section, we treated the case in which voice channels are placed in the baseband in accordance with the $C/N_0$ of the earth station to which they are headed—channels to the poorest quality stations being lower in the baseband. One can, however, use any ordering scheme. Each different ordering scheme will, however, result in a different gain with the technique for finding it being the same as in Section 3. To demonstrate the variability of gain with channel ordering, we consider the case of reverse loading. This is an ordering scheme that is the exact opposite of the one in Section 3. The channels headed to the highest $C/N_0$ earth station are lowest in the FDM baseband, those headed to the next highest are placed next, and so on. As in the previous section, the earth stations are labeled 1 through $M$ with $(C/N_0)_1 \leq (C/N_0)_2 \leq \ldots (C/N_0)_M$ with $N_i$ circuits going to station $i$, $i = 1,2, \ldots M$. The definition of $\xi_i$ are as in Eq. [8b]. The pre-emphasis filter than has the form

$$P(f) = a_i' f^2, \quad f_m(1-\xi_i) \leq f \leq f_m(1-\xi_{i-1}) \text{ for all } i = 1,2, \ldots M \tag{13}$$

Further, in order to equalize SNR at each earth station, we require

$$\frac{a_i'}{a_1'} = \frac{(C/N_0)_1}{(C/N_0)_i}. \tag{14}$$

The normalizing condition of Eq. [4] still holds, of course. A sketch of the form of $P(f)$ is given in Fig. 3 for the case $M = 4$.

Upon substituting Eqs. [13] and [14] into Eq. [4] and again using Eq. [6], one finds similarly to Section 3

$$(TT/N)_i = (C/N_0)_1 \frac{1}{b}\left(\frac{f_r}{f_m}\right)^2 \frac{3}{\delta'} \tag{15}$$

$$\delta' = \sum_{i=1}^{M} \frac{(C/N_0)_1}{(C/N_0)_i} \left[(1-\xi_{i-1})^3 - (1-\xi_i)^3\right], \tag{16}$$

and again the rf bandwidth is the same as without the compensatory pre-emphasis.

The conclusions are as in the last section. To make $TT/N$ equal to the required value at all earth stations, one may reduce the received carrier power to $1/\delta'$ as much (or by $-10 \log_{10}\delta'$ dB) and keep the bandwidth the same; or, arguing as before, one can keep the power the same and reduce the rf bandwidth by the factor $[1 + p \cdot g\sqrt{\delta'}\, f_r/f_m]/[1 + p \cdot g f_r/f_m]$ or any number of combinations.

Considering as before the case $M = 2$ and substituting into Eq. [16], we have

$$\delta' = 1 - (1 - \rho)(1 - \xi_1)^3. \qquad [17]$$

The gain in dB is plotted as a function of $\xi_1$ in Fig. 2 with $\rho$ as a parameter (dotted curves). The results, as expected, are much worse than for normal loading and indicate the undesirability of this procedure.

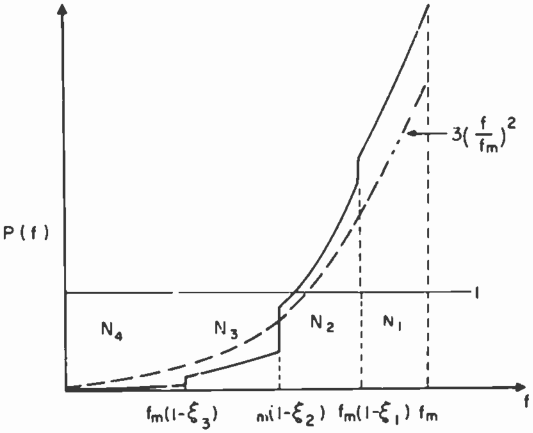

**Fig. 3**—Pre-emphasis function for compensatory pre-emphasis with reverse loading.

Actually, the results for this case are only accurate for cases where $(C/N_0)_M/(C/N_0)_1$ is not too large. If, however, the maximum discrepancy in earth station performance becomes large, these results, as poor as they are, become somewhat optimistic. To see why, we must retrace the discussion in Section 2. Recall that in deriving the bandwidth result for an FDM/FM system with pre-emphasis, a crucial step is to approximate the input to the pre-emphasis filter as a Gaussian signal and (because the filter is a linear device) to therefore approximate the output as a Gaussian signal. While the nature of the approximation at the input is complicated,[3] it is clear that the approximation becomes poorer when the individual voice channels have different gains (as they do at the output of the pre-emphasis network). With standard pre-emphasis it is found, in practice, that the variation in gain produced at the output is not sufficiently high to necessitate a correction. It therefore follows that for compensatory pre-emphasis and normal loading no correction is necessary either, since the variation in gain at the output is actually less than it is for the ideal parabolic pre-emphasis (see Fig. 1). For reverse loading, however, the variation is greater than for a parabolic shape—the variation becoming greater the bigger the difference between $C/N_0$ value at the various earth stations. The problem is that the output signal depends very heavily on only a subset of the $N$ channels going to the poorest earth stations. This could be handled by boosting the value of $g$, but the exact value would depend on the distribution of voice channels. We shall end the discussion by pointing out that while the results derived above hold for reverse loading, increased rf bandwidth probably needs to be allowed for in some situations.

## 5. Standard Pre-Emphasis

The standard pre-emphasis filters used are not actually parabolic but have a constant plus-parabola shape. This is because the pre-emphasis corrects for or equalizes for more than the effects of thermal* noise. Since the output noise density due to thermal noise approaches zero at low baseband frequencies, other sources of noise which are normally negligible become dominant. The effect of these various sources is taken into account by assuming that the shape of the noise spectrum is of the form $[1 + (f/f_0)^2]$ where $f_0$ depends on the relative strengths of thermal and nonthermal noise. In calculating link budgets, where these relative strengths are not known a priori, it is common practice to use a CCIR recommendation, which indirectly specifies $f_0$. The pre-emphasis filter has the same form as the total noise spectrum assumed

$$P(f) = K^{-1}[1 + (f/f_0)^2]. \qquad [18]$$

To meet the normalization condition of Eq. [4], it follows that

$$K = \left[1 + \frac{1}{3}\left(\frac{f_m}{f_0}\right)^2\right] \qquad [19]$$

The CCIR recommendation is to take the pre-emphasis for the topmost channel ($f = f_m$) as 4 dB (or a factor of 2.511 . . .) rather than a factor of 3 which is the result for a parabolic pre-emphasis. Using Eqs. [18] and [19] and $P(f_m) = 2.511$ implicitly specifies $f_0$ in terms of $f_m$. Then $(f_m/f_0)^2$

---

* We call it thermal noise when it is lumped into the $C/N_0$ value of the station even though the ultimate causes may be nonthermal (such as intermod noise from the satellite TWT).

= 9.292 . . . , and we shall use this value whenever making numerical calculations.

In analogy to the work of Section 3, we wish to provide equal SNR for each voice channel at each earth station taking into account a constant-plus-parabolic noise spectrum. Because the value of $f_0$ will in general be different for each station, there is no simple modification of the pre-emphasis of Eqs. [18] and [19] that will accomplish this. Further, these values (of $f_0$) will not usually be known. In analogy with the CCIR procedure for standard pre-emphasis, we change the problem slightly and (for normal loading) we imagine that at station 1 the lowest group of voice channels $N_1$ have a test tone-to-noise given by $(TT/N)_{req}$, that the second group $N_2$ have the value $[(C/N_0)_1/(C/N_0)_2](TT/N)_{req}$ and so on until the last group of $N_M$ has value $[(C/N_0)_1/(C/N_0)_M](TT/N)_{req}$. The idea is that the other stations will arrive at approximately the required value of $TT/N$ because of the proportionately higher $C/N_0$. Another way of putting this is that an $(f_m/f_0)^2$ value of 9.292 is assumed at each of the earth stations.

In analogy with Section 3, we assume a pre-emphasis function $P(f)$ given by

$$P(f) = b_i \frac{1 + (f/f_0)^2}{K}, \quad \xi_{i-1} f_m \leq f \leq \xi_i f_m \tag{20}$$

where $K$ is given by Eq. [19]. The values of $b_i$ obey the relation

$$\frac{b_i}{b_1} = \frac{(C/N_0)_1}{(C/N_0)_i} \tag{21}$$

and, of course, the normalizing relation of Eq. [4] holds. Substituting Eqs. [20] and [21] into Eq. [4] [gives

$$b_1 = 1/\delta'' \tag{22}$$

$$\delta'' = \left[1 + \frac{1}{3}\left(\frac{f_m}{f_0}\right)\right]^{-1} \left\{ \sum_{i=1}^{M} \frac{(C/N_0)_1}{(C/N_0)_i} \times \left[ (\xi_i - \xi_{i-1}) + (\xi_i^3 - \xi_{i-1}^3) \frac{1}{3} \left(\frac{f_m}{f_0}\right)^2 \right] \right\}. \tag{23}$$

Now since the CCIR recommended pre-emphasis network has the form $K^{-1}[1 + (f/f_0)^2]$ and the pre-emphasis function of the $N_1$ channels going to earth station one is $b_1 K^{-1}[1 + (f/f_0)^2]$, it follows that compensatory pre-emphasis provides a gain over noncompensatory pre-emphasis of $b_1$ or $1/\delta''$ where $\delta''$ is given by Eq. [23]. Likewise, the gains of all the other groups are $1/\delta''$.

To gain some appreciation for how this modification of standard pre-emphasis differs from the "ideal" case, consider the case $i = 2$ with $\rho = (C/N_0)_1/(C/N_0)_2$. Then

$$\delta'' = (1-\rho)\frac{\xi_1 + \xi_1^3 \frac{1}{3}\left(\frac{f_m}{f_0}\right)^2}{1 + \frac{1}{3}\left(\frac{f_m}{f_0}\right)^2} + \rho. \qquad [24]$$

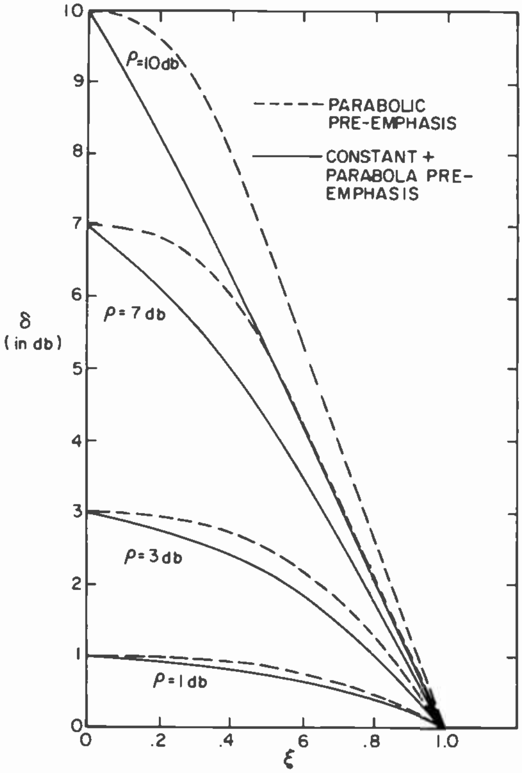

**Fig. 4**—Gain for parabolic pre-emphasis and constant-plus-parabolic pre-emphasis.

This is plotted in Fig. 4 along with the results for "ideal" pre-emphasis from Section 3 for comparison. As would be expected, the results for standard pre-emphasis are somewhat worse. Bear in mind that the solid curve holds only for the value $(f_m/f_0)^2 = 9.292$. For higher values of this ratio (i.e., lower $f_0$ or less excess low-frequency noise), the results are higher. In fact, as $f_m/f_0 \to \infty$, the results of Eq. [24] approaches the result of Eq. [12] as indeed it should.

## 6. Summary

We have shown that as long as the $C/N_0$ at the various destination stations are different, compensatory pre-emphasis always results in a gain. The numerical value of this gain has been calculated for various circumstances. We have further shown how this gain may be utilized to reduce carrier power or reduce rf bandwidth or combinations of these. We have also shown that the compensatory pre-emphasis function can be simply produced by the normal pre-emphasis filter fed by channel groups in the FDM group inputted at different gains.

It should be remarked that while all the calculations performed here are for providing equal SNR at each earth station, this is by no means necessary. The development of expressions for the case of unequal desired SNR proceeds in a parallel way. The results differ in that the expressions, which in our case involve quotients of carrier-to-noise density ratios, will (in the case of unequal SNR) involve the product of quotients of carrier-to-noise density and SNR.

## Acknowledgment

The author wishes to thank H. Staras for many helpful discussions.

### References

[1] M. Schwartz, *Information Transmission, Modulation and Noise* (Section 6.11), Second Edition, McGraw-Hill Book Co., N.Y. (1970).

[2] P. L. Bargellini, "Intelsat IV Communication System," *COMSAT Tech Rev.*, 2, No. 2, 1972 (pp. 437–572 and p. 460 in particular).

[3] *Transmission Systems for Communications*, Fourth Edition, Bell Telephone Laboratories (Sections 9.1 and 9.2).

# A High-Speed CCD-Scanned Photosensor for Gigabit Recording Applications*†

**D. A. Gandolfo, A. Boornard, E. P. Herrmann, and D. B. Stepps**

RCA Advanced Technology Laboratories, Camden, N.J. 08102

**Abstract**–Experiments with a CCD-scanned photocapacitor array are given. The device, a 32-stage, linear array processed in buried channel technology has been operated at clock frequencies in excess of 100 MHz. At frequencies up to 50 MHz, we estimate that the upper limit of the transfer loss is $2 \times 10^{-4}$ per transfer. Parallel charge transfer from the photocapacitor array into the readout register in 5 nanosec with less than 5% loss has been observed. The paper also describes several possible device configurations for use in a 2-gigabit/sec recording system.

## 1. Introduction

The continuing objective of the work presented here is to develop photosensors capable of serving as readout devices for ultra-wideband, holographic recorder-reproducer systems. In particular, the use of charge-coupled devices is investigated, and it is found that these devices with high sensitivity, low noise, and high operating speed are well suited to the application. Earlier work[1] examined, in a general way, the requirements imposed by two classes of gigabit recording systems on charge-coupled photosensors. That work provided an experimental demonstration that a crucial requirement, that of high-speed low-loss serial transfer of the photogenerated charge, could be met. Analysis showed that the signal-to-noise ratio would be adequate at the low light

---

* Supported in part by Rome Air Development Center contract F30602-76-C-0072; A. Jamberdino and J. Petruzelli, Project Engineers.

† This paper was presented at the 1976 Electro-Optics/Laser Conference, N.Y., Sept. 14-16 (1976), and appears in the Proceedings of that conference.

levels expected. More recent work has concentrated on high-speed parallel transfer of charge from the photosensors into the serial transport register, serial transfer at still higher speeds, and device configurations capable of operating with a breadboard version of a gigabit recorder. We have developed a CCD-scanned photosensor array that has demonstrated (1) serial transfer at frequencies up to 50.5 MHz with no observable transfer loss and (2) parallel transfer time as short as 5 nanosec with very small transfer loss. Several device configurations for a 2-gigabit-per-second system have been considered and will be described.

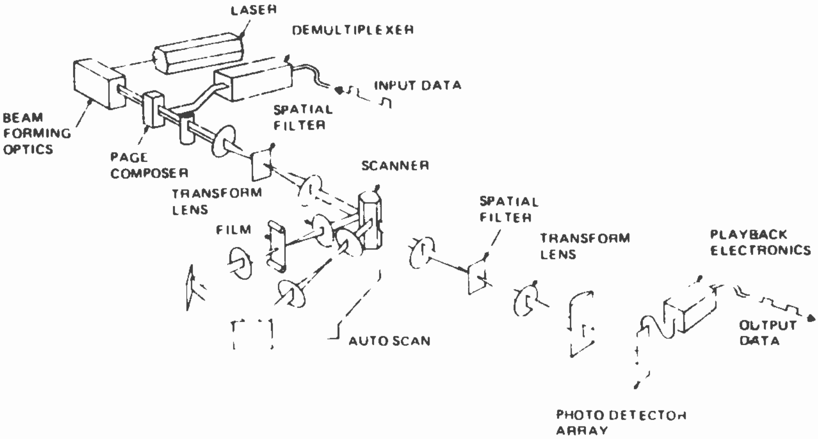

Fig. 1—Functional diagram of the SP* class of holographic recorder reproducer systems. The high-speed scanner deflects 128 bit Fourier transform holograms. (After Bardos.[2])

## 2. Ultra-Wideband Recording

The baseline system for realization of a gigabit recorder-reproducer has been designated the SP*-2. It is shown schematically in Fig. 1 and has been described by Bardos[2] and others.[3] The distinguishing characteristic of this system (as far as the readout technique is concerned) is a polygonal mirror that rotates at high speed and sweeps 128-bit holograms past the image plane at a rate of up to $1.56 \times 10^7$ holograms/sec. An output data rate of up to 2 gigabits/sec is thus realized. The format of an individual hologram is simply a linear array of 128 bit positions with each position occupied by a bright or dark spot. During readout, an entire 128-bit hologram will be imaged on the readout device at one time. The dwell time for a single hologram is 64 nanoseconds, for a 2-gigabit/sec rate, with laser light incident during approximately 50% of this time. Thus, a new hologram is presented for readout every 64 nanoseconds. The characteristics of the SP*-2 system that are particularly relevant to development of a readout subsystem are summarized in Table 1.

*Table 1*—System SP*-2 Baseline Readout Parameters for 2-Gb/sec input—2-Gb/sec output Holographic Recorder-Reproducer

| | |
|---|---|
| Hologram Readout Rate | $15.625 \times 10^6$ Holograms/sec ($2$ Gb $\text{sec}^{-1}/128$ Bits $\text{Holo}^{-1}$) |
| Hologram Scan Duration (128 Bit "1"/"0" pattern) | 64 ns (per 128 bits) |
| Laser Type | Argon (5145 Å) |
| Laser Operation | CW |
| Laser Power | 3.0 watts |
| Height of "1"/"0" pattern at readout plane | 0.325 cm (128 mils) to 0.650 cm (256 mils)* |
| Optical Power per "1" | 240 nW* |
| Optical Energy per "1" | $7.68 \times 10^{-15}$ joules† |
| No. of Photons per "1" | $2.0 \times 10^4$ |

* Conversation H. N. Roberts, Harris Corporation, Melbourne, Florida.
† Assumes 1/2 of 64 ns scan period is useful.

## 3. CCD-Scanned Photocapacitor Array

Ref. [1] pointed out that the CCD scanned photosensor has important advantages as a readout device in high-speed recording systems. This device (Fig. 2) in its simplest form consists of a photocapacitor array, a transfer gate and a CCD readout register. Minority carriers generated by light incident on the photocapacitor array are collected in potential wells created by a bias applied to the photogate. (Majority carriers escape into the substrate.) A pulse applied to the transfer gate will cause parallel transfer of the accumulated charge packets from the photocapacitor array into the CCD register. The charge packets are then clocked out by the CCD register. The principal advantage of this arrangment is that data smearing is prevented. The transfer gate isolates the photosensors from the readout register so that optical integration of a hologram can occur while the previous hologram is being read out.

High-speed operation of CCD's is made possible by the buried channel process. This process causes signal charges to be stored a small distance below the silicon-oxide interface so that charges are not exposed to surface states. Thus, transfer loss associated with surface states is eliminated, resulting in low noise and a higher MTF at high frequency. In addition, the charge transport is governed by bulk mobility so that higher drift velocity and higher operating frequencies may be realized.

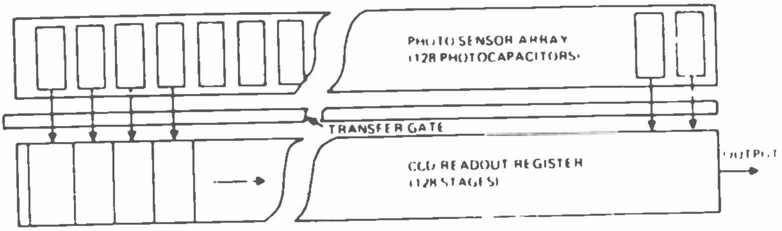

(A) BASIC READOUT ARRAY

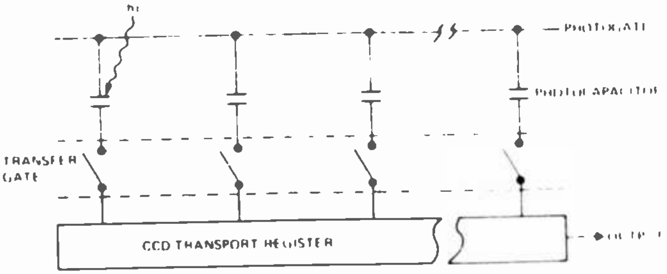

(B) PARTIAL SCHEMATIC OF READOUT ARRAY

**Fig. 2**—Basic arrangement of CCD scanned photocapacitor array and partial schematic circuit.

## 4. Requirements for Potential Photosensor Configurations

We will now examine several ways in which CCD-scanned photocapacitor arrays may be arranged to satisfy the readout requirements of a 2 gigabit/sec system. The characteristics of each arrangement, especially with respect to operating speed, will be given. Figs. 3–7 show, conceptually, five configurations differing from each other in the number of devices

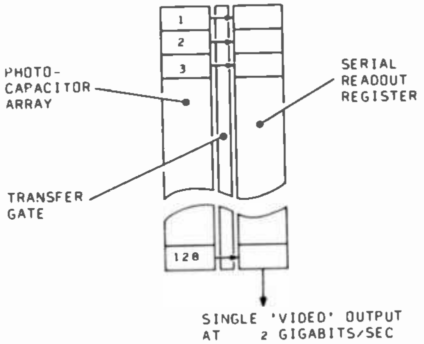

**Fig. 3**—Modulo 1 photosensor configuration.

employed, the number of data outputs, the time allowed for parallel transfer, and the CCD clock (serial transfer) frequency. The arrangement designated Modulo 1 is not considered a realistic option but is given in order to establish perspective. If all 128 bits are read out by a single CCD register and if 10 nanosec parallel transfer time is allowed, then the CCD must be clocked at 2.36 GHz, well beyond even the most optimistic estimate of CCD capability.

The Modulo 16 configuration (Fig. 4) would have 16 CCD readout registers arranged (8 on either side) about a linear array of 128 photosensors. Thus, there would be 16 outputs at 148 MHz each (the CCD clock frequency), where we are still allowing 10 nanosec parallel transfer time. While operation at 148 MHz is difficult, it is in the range achieved by several laboratories.[4,5] The Modulo 32 configuration (Fig. 5) is similar to Modulo 16 except that 32 CCD registers (hence, 32 outputs), operating at 74 MHz each, are required. The Modulo 128 approach (Fig. 6) would have 128 outputs, each yielding data at a 16 MHz rate. This approach eliminates the CCD serial transfer register. However, it does make use of charge coupling principals in transferring signal charge from the photosensors to the output circuits, thereby achieving low noise and high sensitivity (chiefly through a reduction in the sense node capacitance). Modulo 16 with 5:1 fanout (Fig. 7) would use 5 photosensor devices in parallel. The devices would be coupled to the image plane via fiber optics (or possibly, prismatic beam splitters). This approach permits an increase in parallel transfer time to 80 nanosec while slowing the CCD clocks to 40 MHz. The penalty, of course, is a decrease in signal-to-noise ratio by a factor equal to the fan out, since light from a single image plane position must be divided to illuminate several sensors. The characteristics of the various approaches are summarized in Table 2.

## 5. Experiments

Laser probe experiments on a CCD-scanned photocapacitor array, developed at RCA, have provided answers to important questions about serial and parallel transfer. The laser probe experimental setup (Fig. 8) enables us to illuminate one photosensor element at a time and to move the laser spot from element to element for comparison. The light source is a 3-mW He-Ne laser. With precision attentuators, we can vary the power incident on the sample from 3 mW down to a few nanowatts. The modulator controls the optical integration time so that the quantity of light incident may be held constant while other parameters are varied. The autocollimator provides a gaussian spot and the micromanipulator moves the laser spot from element to element. High-speed, emitter-

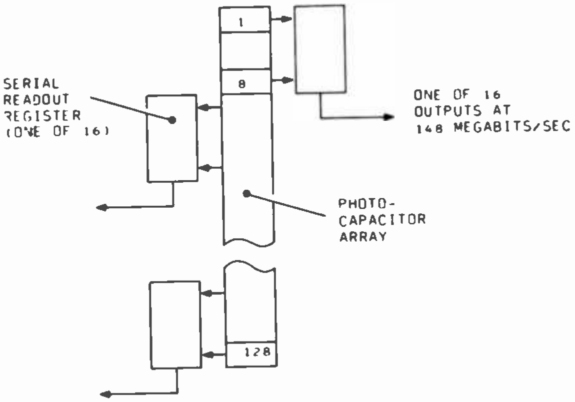

Fig. 4—Modulo 16 photosensor configuration.

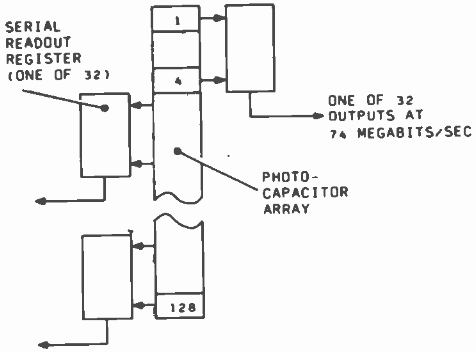

Fig. 5—Modulo 32 photosensor configuration.

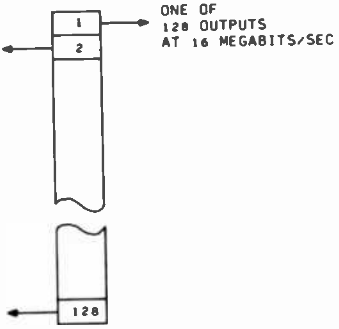

Fig. 6—Modulo 128 photosensor configuration.

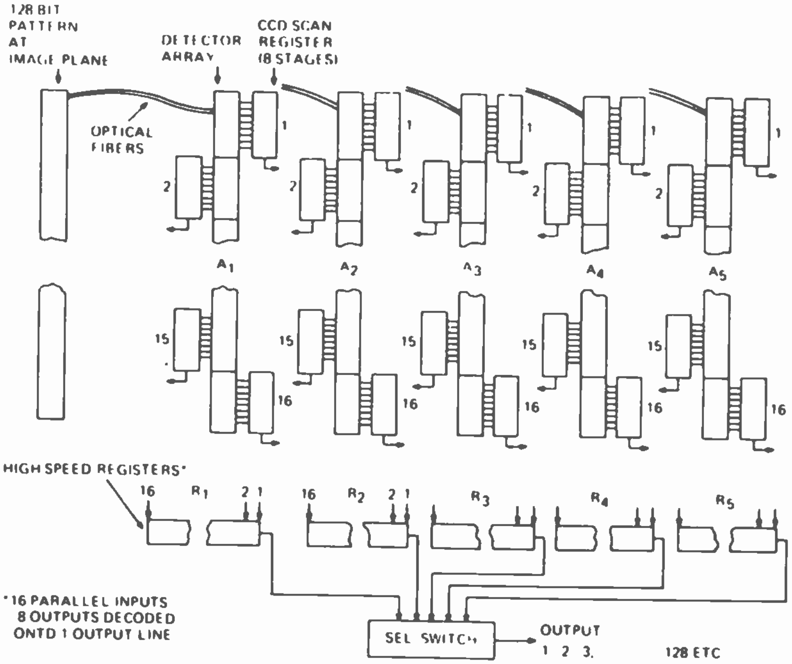

Fig. 7—Modulo 16 photosensor configuration with 5:1 fan-out.

coupled-logic circuits are used for timing; discrete devices are used for clock drivers.

The experimental device is shown in Fig. 9(a). It is a 32-element CCD scanned photocapacitor array and was fabricated using the RCA buried n-channel process with aluminum and polysilicon gates. The important features of the photosensor array are shown schematically in Fig. 9(b).

*Table 2*—Summary of Requirements for Various Photosensor Configurations

| Configuration | No. of Outputs | Parallel Transfer Time | CCD Clock Frequency |
|---|---|---|---|
| Modulo 1 | 1 | 10 nsec | 2.36 GHz |
| Modulo 16 | 16 | 10 nsec | 148 MHz |
| Modulo 32 | 32 | 10 nsec | 74 MHz |
| Modulo 128 | 128 | 32 nsec | * |
| Modulo 16 w/5:1 fanout | 16 from each of 5 CCDs | 80 nsec | 40 MHz |

* No CCD register is used in this case. The output data rate is 16 MHz.

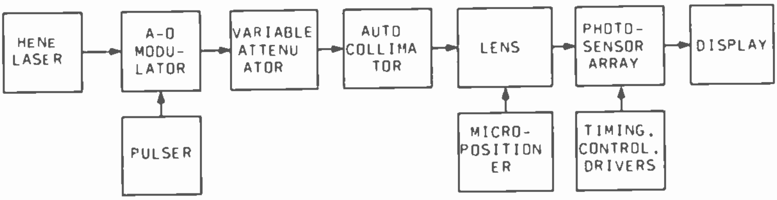

**Fig. 8**—Schematic of laser probe experimental setup.

The complex structure of the photosensor was designed to enable the high-speed transfer of charge over a long length, approximately two mils (50 $\mu$m), as initially required by the geometry of the data bits in the readout application. In the experiments reported here, the laser spot was imaged on image gate 1 while the storage electrode and the transfer gate were tied together and operated as a single gate.

Several different clocking techniques were used: (1) sine-wave, four-phase, interrupt; (2) sine-wave, two-phase, continuous; and (3) square-wave, four-phase, interrupt. Square-wave clocks were used up to 40 MHz

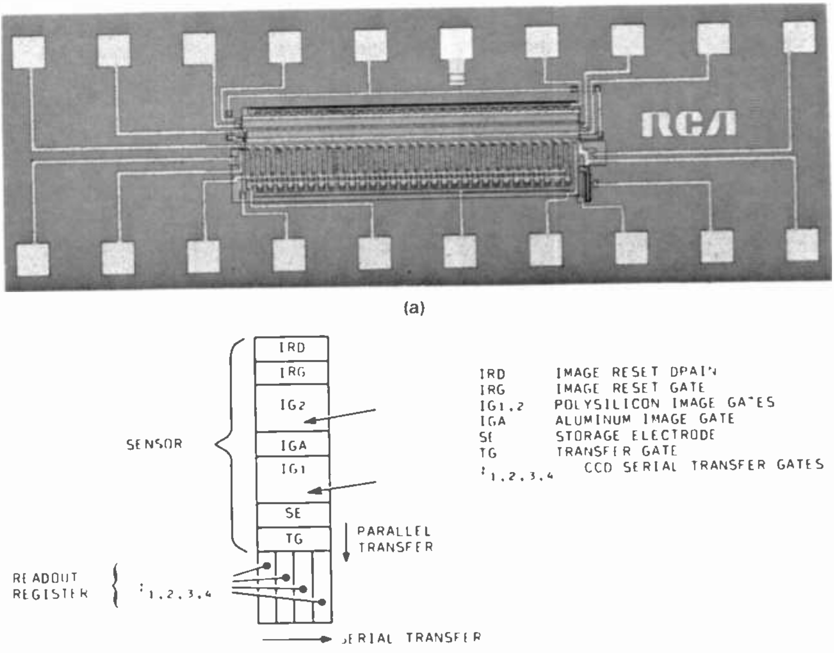

**Fig. 9**—Photomicrograph of experimental charge-coupled photosensor array (TC1180) and gate structure schematic showing one sensor element and one stage of the CCD readout register.

while sine-wave clocks were used up to 180 MHz. (While operation at 180 MHz was observed, the clocks were not optimized for that frequency and no quantitative results can be given.) Two-phase operation simplified timing but four-phase operation yielded lower transfer loss. In the interrupt mode, the CCD serial-transfer clocks were stopped during parallel transfer; in the continuous mode, used at the highest frequencies, the serial clocks continued to run during parallel transfer. Continuous clocking permits operation without additional time for parallel transfer, thus allowing a reduction in serial-transfer clock frequency. However, the timing of the transfer pulse is more critical than in the interrupt mode.

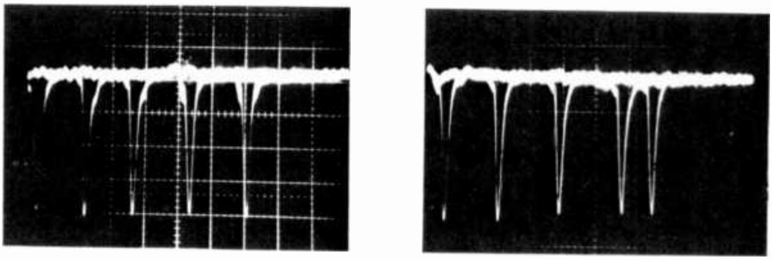

(a) 41.5 MHz

(b) 42.9 MHz

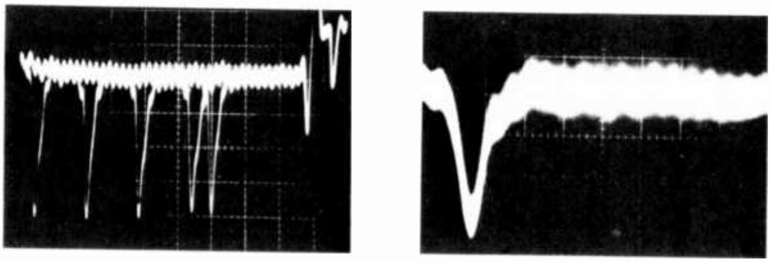

(c) 50.5 MHz

(d) 109 MHz

Fig. 10—Serial transfer measurements. Photos (a), (b), and (c) for four-phase sine wave interrupt clocks; photo (d) is for two-phase sine wave continuous clocks. Shown are output signals when individual sensor elements are illuminated by laser spot.

Data are presented for two general classes of measurements—those concerned with high-speed serial transfer in the CCD register, and those concerned with high-speed parallel transfer from the photosensors into the serial transport register.

Serial transfer data are given in Fig. 10 for several frequencies. In photos (a) and (b), four-phase, sine-wave, interrupt clocks were used. The photos are multiple exposures with the laser spot illuminating a different element for each exposure. Photo (c) was made with the device operated by two-phase, sine-wave, continuous clocks. In photos (a) and (b), the left-most signal is from a sensor near the device output while the right-most signal is from the sensor farthest from the output. If there were significant transfer losses, the signals from the more distant sensors would be smaller since they undergo more transfers. However, this is not the case in the data shown here, where signals from more distant elements are equal in amplitude to those nearer the output. If we say that the last signal is one-half of one small division smaller than the first signal, we may estimate the upper limit to be $\epsilon = 2 \times 10^{-4}$ per transfer. This would result in a barely-perceptible amplitude difference between the first and last elements. The scope trace in photo (c) shows operation at 109 MHz.

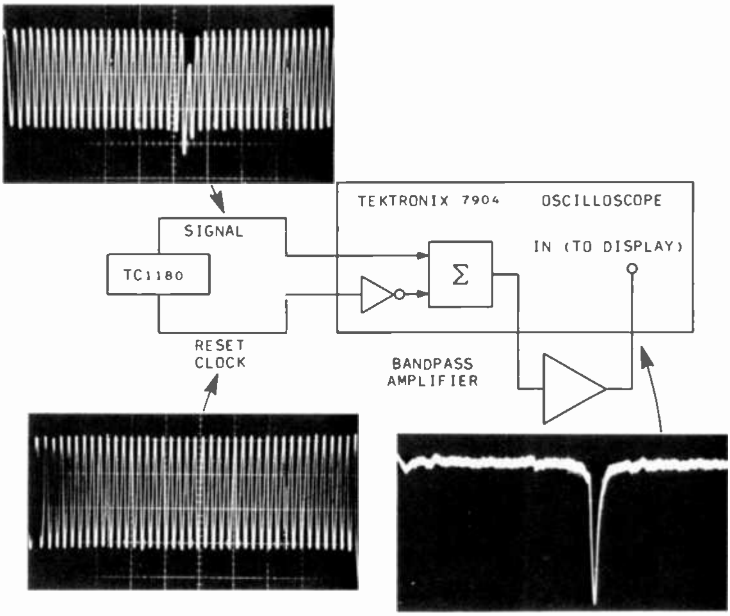

**Fig. 11**—Clock feed through cancellation.

Clock feedthrough cancellation was used as shown in Fig. 11. One of the chief advantages of the sine-wave clocks is that they greatly simplify feedthrough cancellation.

In measuring the effects of high-speed parallel transfer, we used the modulated laser beam. A light pulse of about 600 nanosec duration illuminated Image Gate 1 (see Fig. 9(b)). The serial register was driven by 40 MHz, four-phase, sine-wave clocks interrupted for parallel transfer. As stated previously, the storage electrode and the transfer gate were tied together. The photogenerated charge had to travel at least 0.6 mils (21 $\mu$m), the distance from the edge of Image Gate 1 to the edge of the serial register (phase-3) gate. Transfer pulse widths from 140 nanosec to 5 nanosec were used and the amplitude of the output signal was observed. The modulated laser pulse ensured that the quantity of photogenerated charge was constant, thus any change in output signal could be attributed to parallel transfer loss. A typical experiment is illustrated in Fig. 12, showing that the 5-nanosec transfer pulse is capable of effecting parallel transfer. The data are summarized in Table 3 where it is seen that there is a change of not more than 5% in the output signal amplitude as the transfer pulse width decreases from 140 nanosec to 5 nanosec. This result is consistent with a calculation from the theory[6] that indicates that for the conditions given here (transfer pulse amplitude 10 volts, oxide thickness 0.1 $\mu$m, and taking the effective gate length to be 1 mil (25.4 $\mu$m)), the fringe-field time constant, which governs charge transport, is about 1 nanosec. Thus, we calculate that 5 nanosec (5 time-constants) after application of the transfer pulse, 99% of the photogenerated charge will have been transferred.

## 5. Conclusions

The efficient, high-speed, serial and parallel transfer demonstrated in the experiments reported here, indicate that charge-coupled photosensor arrays will serve as readout devices in gigabit recording systems. Several possible configurations have been described, offering flexibility in designing devices for specific systems.

## Acknowledgment

The authors are grateful to J. E. Carnes, R. Dawson, W. F. Kosonocky, and F. Shallcross of RCA Laboratories, who provided design consultation and device processing, and to R. F. Kenville and P. E. Wright who encouraged this work.

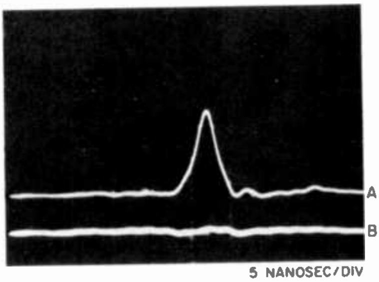

(a) transfer pulse

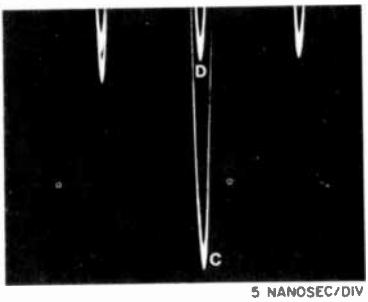

(b) photosensor output signal

**Fig. 12**—High speed parallel transfer: trace A shows the pulse applied to the transfer gate and trace C the corresponding output signal; when the transfer pulse amplitude is reduced to zero (trace B), the output signal drops to the feedthrough level (trace D).

*Table 3*—Parallel Transfer Results (Serial Transfer Clock 40 MHz)

| Transfer Pulse Width (nanosec) | Output Signal Amplitude (mV) |
|---|---|
| 140 | 105 |
| 116 | 105 |
| 104 | 105 |
| 95 | 105 |
| 60 | 105 |
| 50 | 105 |
| 28 | 105 |
| 15 | 100 |
| 5 | 100 |

## References:

[1] D. A. Gandolfo, A. Boornard and L. J. Nicastro, "Charge Coupled Devices for Gigabit Recording Applications," *Proc. 1975 Electro-Optical Systems Design Conf.*, Anaheim, CA, Nov. 11-13, 1975.

[2] Andrew Bardos, "Wideband Holographic Recorder," *Applied Optics*, **13**, p. 832, April 1974.

[3] A. M. Bardos, R. H. Nelson, H. N. Roberts and C. A. Shuman, "Multigagbit Per Second Digital Data Recording," *Proc. 1975 Electro-Optical Systems Design Conf.*, Anaheim, CA, Nov. 11-13, 1975.

[4] M. J. J. Theunissen and L. J. M. Esser, "PCCD Technology and Performance," 1974 International Conf. on Technology and Applications of Charge-Coupled Devices, Edinburgh, Scotland, Sept. 1974.

[5] Y. T. Chan, B. T. French and P. E. Green, "Extremely High Speed CCD Analog Delay Line," 1975 International Conf. on the Application of Charge-Coupled Devices, San Diego, CA, Oct. 29-31, 1975.

[6] A. Boornard and L. J. Nicastro, "Charge Coupled Devices for Gigabit Recording Applications," Final Report to Rome Air Development Center, Contract F30602-74-C-0339.

# Recent Papers by RCA Authors

*Listing is alphabetical by name of primary author. For copies of reprints, the reader should contact the publication directly.*

R. C. Alig, "Optical Properties of a Dense Two-Dimensional Electron Gas," **RCA Review,** Vol. 37, No. 2, p. 206, June 1976.

G. A. Alphonse and W. Phillips, "Iron-Doped Lithium Niobate as a Read-Write Holographic Storage Medium," **RCA Review,** Vol. 37, No. 2, p. 184, June 1976.

G. A. Alphonse and W. Phillips, "Read-Write Holographic Memory with Iron-Doped Lithium Niobate," **Ferroelectrics,** Vol. 11, p. 397, 1976.

G. W. Beakley, "Television to Small Earth Stations," **Trans. on Broadcasting,** Vol. 22, No. 3, p. 96, Sept. 1976.

A. Bloom, R. A. Bartolini, P. L. K. Hung, and D. L. Ross, "A Non-Polymeric Organic Host for Recording Volume Phase Holograms," **Appl. Phys. Lett.,** Vol. 29, No. 8, p. 483, Oct. 15, 1976.

D. E. Carlson and C. E. Tracy, "Metallization of Glass Using Ion Injection," **Amer. Ceramic Soc. Bull.,** Vol. 55, No. 5, p. 530, May 1976.

J. E. Carnes and R. L. Rodgers, III, "Recent Results on CCD Imagers," **Laser 75 Opto-Electronics,** p. 78.

R. S. Crandall, "Properties of Surface State Electrons on Liquid Helium," **Surface Science,** Vol. 58, p. 266, 1976.

M. Ettenberg, G. H. Olsen, and C. J. Nuese, "The Effect of Gas Phase Stoichiometry on the Minority Carrier Diffusion," **Appl. Phys. Lett.,** Vol. 29, No. 4, p. 141, Aug. 1, 1976.

D. G. Fisher, "Sources of Photoemission in $Na_3Sb$Thin Films," **J. Appl. Phys.,** Vol. 47, No. 8, p. 3471, Aug. 1976.

B. Goldstein, D. J. Szostak, and V. S. Ban, "Langmuir Evaporation from the (100), (111A), and (111B) Faces of GaAs," **Surface Science,** Vol. 57, p. 733, 1976.

I. Gorog, P. V. Goedertier, J. D. Knox, I. Ladany, J. P. Wittke, and A. H. Firester, "Information Scanning Technology: Applications of CW AlGaAs Injection Lasers," **Appl. Optics,** Vol. 15, No. 6, p. 1425, June 1976.

J. J. Hanak and R. W. Klopfenstein, "Model of Target Cross Contamination During Co-Sputtering," **RCA Review,** Vol. 37, No. 2, p. 220, June 1976.

E. W. Herold, "A History of Color Television Display," **Proc. IEEE,** Vol. 64, No. 9, p. 1331, Sept. 1976.

G. W. Hughes, R. J. Powell, and M. H. Wood, "Oxide Thickness Dependence of High-Energy Electron, VUV, and Corona-Induced Charge in MOS Capacitors," **Appl. Phys. Lett.,** Vol. 29, No. 6, p. 377, Sept. 1976.

A. C. Ipri and D. W. Flatley, "Radiation Tolerant Silicon Gate CMOS/SOS Using Ion Implantation," **IEEE Trans. Electron Devices,** p. 1110, Sept. 1976.

W. Jantz, J. R. Sandercock, and W. Wettling, "Determination of Magnetic and Elastic Properties of $FeBO_3$ by Light Scattering," **J. Phys. C:Solid State Phys.,** Vol. 9, p. 2229, 1976.

K. M. Kim and H. E. Temple, "Growth of Optically Homogeneous Single Crystals of $Pb_5GeO_4(VO_4)$ from the Melt," **J. Crystal Growth,** Vol. 34, p. 177, 1976.

H. Kressel, I. Ladany, M. Ettenberg, and H. Lockwood, "Light Sources for Optical Communications Using Fibers," **Phys. Today,** Vol. 25, No. 5, May 1976.

H. Kressel and M. Ettenberg, "Low-Threshold Double-Heterojunction AlGaAs/GaAs Laser Diodes: Theory and Experiment," **J. Appl. Phys.,** Vol. 47, No. 8, p. 3353, Aug. 1976.

H. B. Law, "The Shadow Mask Color Picture Tube: How it Began—an Eyewitness Account of its Early History," **IEEE Trans. Electron Devices,** Vol. 23, No. 7, p. 752, July 1976.

D. Meyerhofer, "Distortion of Liquid Crystals in the Twisted Field Effect Configuration," **Mol. Cryst. Liq. Cryst.,** Vol. 34, p. 13, 1976.

R. Mezrich, D. Vilkomerson, K. Etzold, "Ultrasonic Waves: Their Interferometric Measurement and Display," **Applied Optics,** Vol. 15, p. 1499, No. 6, June 1976.

R. M. Moore, "Cost Predictions for Photovoltaic Energy Sources," **Solar Energy,** Vol. 18, p. 225, Pergamon Press, 1976.

C. J. Nuese, G. H. Olsen, and M. Ettenberg, "Vapor-Grown CW Room-Temperature $GaAs/In_yGa_{1-y}P$ Lasers," **Appl. Phys. Lett.,** Vol. 29, No. 1, p. 54, July 1, 1976.

S. M. Perlow, "Third-Order Distortion in Amplifiers and Mixers," **RCA Review,** Vol. 37, No. 2, p. 234, June 1976.

W. Phillips, "Recent Results on Diffused Lithium Niobate-Tantalate Waveguides," **Ferroelectrics,** Vol. 10, p. 221, 1976.

A. Pierrefeu, B. Dorner, and E. F. Steigmeier, "Inelastic Neutron Scattering in SbSI Near the Ferroelectric Phase Transformation," **Ferroelectrics,** Vol. 12, p. 125, 1976.

R. J. Powell, "Photoconductive Processes in $Al_2O_3$ Films," **J. Appl. Phys.,** Vol. 47, No. 3, p. 4604, Oct. 1976.

M. Rayl, P. J. Wojtowicz, and H. D. Hanson, "Magnetic Gas Sensor," **AIP Conf. Proc. Magnetism and Magnetic Materials,** 21st Annual Conf., 1975.

W. Rehwald, "Ultrasonic Studies of Ferroelectric Phase Transitions," **Ferroelectrics,** Vol. 12, p. 105, 1976.

J. R. Sandercock, "Simple Stabilization Scheme for Maintenance of Mirror Alignment in a Scanning Faby-Perot Interferometer," **J. Physics E: Scientific Instrument,** Vol. 9, p. 567, 1976.

G. L. Schnable, "Applications of Electrochemistry to Fabrication of Semiconductor Devices," **Fabrication of Semiconductor Devices,** Vol. 123, No. 9, p. 310, Sept. 1976.

G. L. Schnable, "Reliability of MOS Devices in Plastic Packages," **International Microelectronics Conf.,** June 9, 1976.

E. K. Sichel and B. Serin, "The Right-Leduc Effect in Superconductors," **J. Low Temperature Phys.,** Vol. 24, Nos. 1/2, p. 145, 1976.

E. K. Sichel and R. E. Miller, "Sputtering of Reactive Metals for Composite Materials: Erbium and $Al_2O_3$," **Thin Solid Films,** Vol. 37, p. L19, 1976.

E. K. Sichel and R. E. Miller, "Thermal Conductivity of Highly Oriented Pyrolytic Boron Nitride," **Thermal Conductivity,** Vol. 14, 1976.

H. S. Sommers, Jr. and D. O. North, "The Power Spectrum of Injection Lasers: The Theory and Experiment on a Nonlinear Model of Lasing," **Solid State Electronics,** Vol. 19, No. 8, p. 675, 1976.

W. C. Stewart, "On Differential Phase Contrast with an Extended Illumination Source," **J. Optical Soc. Amer.,** Vol. 66, No. 8, p. 813, Aug. 1976.

M. Toda and S. Osaka, "Optical Imaging Effect of Cr Film," **Japanese J Appl. Phys.,** Vol. 15, No. 6, p. 1101, June 1976.

L. C. Upadhyayula, "Quasienhancement Mode of Operation of Transferred Electron Logic Devices (TELDs)," **Elec. Lett.,** Vol. 2, No. 10, May 13, 1976.

L. C. Upadhyayula, "Trigger Sensitivity of Transferred Electron Logic Devices," **IEEE Trans. Electron Devices,** Vol. 23, No. 9, p. 1049, Sept. 1976.

D. H. R. Vilkomerson, "Measuring Pulsed Picometer-Displacement Vibrations by Optical Interferometry," **Appl. Phys. Lett.,** Vol. 29, No. 3, Aug. 1, 1976.

P. K. Weimer, "A Historical Review of the Development of Television Pickup Devices (1930–1976)," **IEEE Trans. Electron Devices,** Vol. 23, No. 7, p. 739, July 1976.

A. E. Widmer, R. Fehlmann, and H. P. Kleinknecht, "Liquid-Phase Epitaxial Growth of Multiple (AlGa)P-GaP Heterojunction Structures," **J. Crystal Growth,** Vol. 35, No. 1, p. 89, Aug. 1976.

R. Williams, R. S. Crandall, and P. J. Wojtowicz, "Melting of Crystalline Suspensions of Polystyrene Spheres," **Phys. Rev. Lett.,** Vol. 37, No. 6, p. 348, Aug. 9, 1976.

J. P. Wittke, M. Ettenberg, and H. Kressel, "High Radiance LED for Single-Fiber Optical Links," **RCA Review,** Vol. 37, No. 2, p. 159, June 1976.

C. P. Wu, E. C. Douglas, and C. W. Mueller, "Redistribution of Ion-Implanted Impurities in Silicon During Diffusion in Oxidizing Ambients," **IEEE Trans. Electron Devices,** p. 1076, Sept. 1976.

# **Patents Issued to RCA Inventors** Fourth Quarter, 1974

## July

**A. A. Ahmed** Current Mirror Amplifier (3,973,215)
**J. G. Amery** Color Image Signal Processing Circuits (3,969,757)
**J. G. Amery** Defect Compensation Systems (3,969,759)
**J. P. Bingham** Single Frame Color Encoding/Decoding System (3,968,515)
**D. J. Channin and E. B. Priestley** Method of Preparing a Liquid Crystal Display (3,973,057)
**C. W. Clark and C. M. Dye** Window Greenhouse (D240,755)
**E. J. Conlon, R. Destephanis, and T. T. Hitch** Wire Placement Fixture (3,972,463)
**A. G. Dingwall** Low Power Counting Circuits (3,973,139)
**I. Drukaroff and W. Morren** Light Shield for a Semiconductor Device Comprising Blackened Photoresist (3,969,751)
**R. E. Hanson and W. F. Fordyce** Measuring Ignition Timing Using Starter Current (3,968,425)
**R. E. Hanson and W. F. Fordyce** Detecting Malfunction in Cylinders of Internal Combustion Engines (3,972,230)
**L. D. Huff** Signal Pickup Lifting/Lowering Apparatus (3,972,533)
**G. S. Kaplan** Adaptive Parameter Processor for Continuous Wave Radar Ranging Systems (3,968,492)
**E. O. Keizer** Apparatus and Methods for Playback of Color Picture/Sound Records (3,972,064)
**N. Kucharewski** Astable Multivibrator Circuit (3,973,222)
**S. Liu** Apparatus for Mounting a Diode in a Microwave Circuit (3,972,012)
**D. Meyerhofer and A. Sussman** Liquid Crystal Devices of the Surface Aligned Type (3,967,883)
**R. S. Mezrich, K. F. Etzold, and D. H. Vilkomerson** Visual Display of Ultrasonic Radiation Pattern (3,969,578)
**R. W. Nosker and L. P. Fox** Trapezoidal Smooth Grooves for Video Disc (3,968,326)
**E. J. Nossen and E. R. Starner** Digital Arithmetic Synthesizer Phase Lock Loop with Direct Doppler and Frequency Readout (3,973,209)
**R. C. Palmer and J. K. Clemens** Color-Picture/Multichannel-Sound Record and Recording/Playback Apparatus and Methods Therefor (3,969,756)
**G. D. Pyles** Tape Cartridge Player Mechanism (3,973,178)

## August

**R. C. Alig and L. S. Onyshkevych** Surface Acoustic Wave Device and Method of Making Same (3,978,436)
**J. F. Alves, III** Apparatus for Indicating Over-Current Condition in a Transistor Amplifier (3,974,438)
**R. S. Braudy and H. H. Roberts, Jr.** Transfer Recording Process (3,978,247)
**A. R. Campbell** Calculator Timer with Simple Base-6 Correction (3,976,867)
**A. G. Dingwall** Shaped Riser on Substrate Step for Promoting Metal Film Continuity (RE28952)
**R. W. Engstrom and D. E. Bowser** Photodetector Filter Structure (3,976,875)
**R. D. Faulkner and C. M. Tomasetti** Channel Plate Electron Multiplier Tube Having Reduced Astigmatism (3,974,411)
**H. E. Haslau and G. A. Mattson** Automatic Coil Winding Machine and Method (3,976,256)
**L. R. Hulls and S. C. Hadden** Engine Diagnosis from Frequency Components in Exhaust (3,977,239)
**A. C. Ipri, J. C. Sarace, and J. H. Scott** IGFET on an Insulating Substrate (3,974,515)
**R. A. Ito and G. A. Jones** Controlling Communications Between Computer Devices over Common Bus (3,978,451)
**J. E. Keigler, L. Muhlfelder, and R. J. Cenker** Orientation System for a Spin Stabilized Spacecraft (3,977,633)
**S. W. Kessler, Jr., and R. F. Keller** Reinforced Transcalent Device (3,978,518)
**H. Kressel, M. Ettenberg, and I. Ladany** Electroluminescent Edge-Emitting Diode Comprising a Light Reflector in a Groove (3,974,514)
**R. A. Kumbatovic** Switching Circuit (3,978,349)
**E. Lachocki** Power Supply with Means to Reduce On and Off Switching Times of Series Regulated Device (3,975,672)
**I. Ladany, A. C. Limm, and J. T. O'Brien** Method of Making Electrical Contacts Having a Low Optical Absorption (3,975,555)
**J. D. Longbottom** Overbed Table with Locking Mechanism (3,976,016)
**R. W. Longsderff and D. B. Kaiser** Laser Device and a Method of Fabrication (3,976,956)

**C. W. Mueller and E. C. Douglas** Method of Making a Bipolar Transistor (3,974,560)
**D. Redfield** Solar Cell with Grooved Surface (3,973,994)
**A. D. Ritzie** Dual-Mode Adaptive Parameter Processor for Continuous Wave Radar Ranging Systems (3,974,501)
**A. L. Smith and D. D. Shaffer** Manganese-and-Magnesium-Activated Strontium Sulfide Phosphors (3,977,991)
**E. M. Sutphin, Jr.** Filter which Tracks Changing Frequency of Input Signal (3,978,416)
**J. R. Tomcavage** Wire Mesh Cathode (3,976,909)
**D. H. Vilkomerson** Pressure Sensitive Field Effect Device (3,978,508)
**C. P. Wu, E. C. Douglas, and C. W. Mueller** Method of Obtaining the Distribution Profile of Electrically Active Ions Implanted in a Semiconductor (3,976,377)
**C. T. Wu** Conversion of FSK to NRZ Coding (3,976,996)

## September

**A. A. Ahmed** Current Level Detector (3,979,606)
**A. F. Arnold** Nickel-Gold-Cobalt for Silicon Devices (3,982,908)
**H. Arnoldi** Transistor Testing Circuit (3,979,672)
**L. J. Bazin** High Efficiency Deflection Circuit (3,983,452)
**H. R. Beelitz and D. R. Preslar** Electrical Circuit (3,979,607)
**S. Berkman and J. G. Martin** Graphite Susceptor Structure for Inductively Heating Semiconductor Wafers (3,980,854)
**D. R. Carley** Method of Making a Semiconductor Device (3,980,507)
**D. J. Channin** Liquid Crystal Display (3,981,559)
**L. A. Cochran** Switching Arrangement for Flesh Tone Correction and Chrominance Overload Control Circuits (3,982,273)
**A. D. Checki, Jr., and A. G. Frey** Automatic Assembly of Semiconductor Devices (3,978,579)
**L. J. DiMattio** Electron Tube Base (3,979,157)
**N. Feldstein** Method for Electrolessly Depositing Metals Using Improved Sensitizer Composition (3,982,054)
**J. B. George** Tuner Bandswitching System for a Television Tuning System (3,980,959)
**M. Glogola** Protection Circuit (3,980,930)
**A. M. Goldschmidt, W. A. Dischert, and J. R. West** System or Controlling Tension of Magnetic Tape (3,982,160)
**S. C. Hadden, L. R. Hulls, P. J. Slaney, and E. M. Sutphin, Jr.** Tachometer Without Physical Connection to Internal Combustion Engine (3,978,719)
**P. E. Haferl** Deflection Circuit (3,980,927)
**P. M. Heyman, R. L. Quinn, and I. Gorog** Electrochromic Display Device (3,981,560)
**J. O. Horsley** High-Speed Counter with Reliable Count Extraction System (3,982,108)
**H. W. Justice** Etchant for Silicon Nitride and Borosilicate Glasses and Method of Using the Etchant (3,979,238)
**G. J. Lo, F. L. Papworth, N. E. Tenne-Sens, M. V. O'Donovan, and G. Dziub** Metal Plated Body Composed of Graphite Fibre Epoxy Composite (3,982,215)
**M. E. Miller and J. G. Amery** Velocity Correction System with Damping Means (3,983,318)
**F. R. Nyman, J. L. Vossen, Jr., D. G. Fisher, and G. F. Nichols** Metal Coating for Video Discs (3,982,066)
**D. Olivieri and R. J. Socci** Heat Spreader and Low Parasitic Transistor Mounting (3,982,271)
**M. I. Payne** Information Storage Circuit (3,979,735)
**M. I. Payne and B. S. Dalal** Transistor Switching Circuit (3,979,611)
**J. C. Peer and D. W. Luz** Power Supply for a Television Receiver (3,980,821)

# AUTHORS

**A. Boornard** received the B.S. degree in Physics in 1953 from the College of William and Mary and the M.S. degree in Physics from Indiana University in 1955. He served with the U.S. Army from 1955 to 1957. Since joining RCA's Advanced Technology Laboratories in 1957, he has been engaged in research and development in a number of diverse areas. These include electromagnetic wave plasma interactions, radiation effects in semiconductors, microwave plasma diagnostic techniques, experimental studies of the Cerenkov microwave interaction, applications of bulk negative resistance microwave and millimeter wave devices, FET scanned photodiode arrays, pyroelectric IR sensors, and CCD imagers and signal processing devices.

Mr. Boornard is presently associated with the Advanced Technology Laboratories Electron Devices Group. Current programs include the application of large scale, high resolution CCD-scanned photosensor arrays to airborne imaging systems, to specialized high-speed readout devices and the development of CCD signal processing circuits.

Mr. Boornard is a member of the American Physical Society.

**Robert B. Comizzoli** received a B.S. in Physics summa cum laude from Boston College in 1962. He attended Princeton University from 1962 to 1966, receiving the Ph.D. in Physics in 1967. His thesis work involved polarization effects in photoconductors. Since 1966, he has been at RCA Laboratories, Princeton, New Jersey. His research experience includes thermal neutron interactions with polarized nuclei, photoconductivity and transport in II-VI compounds, and electrophotography. He has studied the electrical and photoconductive properties of inorganic and organic electrophotographic materials, including dye-sensitization, and has developed new techniques for the investigation of charge distributions in electrophotographic layers. Presently he is engaged in reliability physics studies on silicon devices.

**D. A. Gandolfo** received the B.S. in Physics at Saint Joseph's College and the M.A. and Ph.D. in Physics at Temple University. He is presently the leader of the Electron Devices group of Advanced Technology Laboratories, engaged principally in the development and application of charge coupled devices. CCD programs in this group include the development of custom devices for a variety of applications, such as analog scan converters for video systems, high-frequency line-scan imagers, and programmable and fixed code correlators. In addition, his group seeks new applications for CCDs developed at other RCA locations and by other manufacturers. Since joining RCA in 1960, he has worked in CCDs, infrared sensors, surface acoustic waves, microwaves, cryogenics, plasma physics, and radiation damage. His work in surface acoustic waves covered a broad spectrum, ranging from investigation of mechanisms for generating, detecting, and guiding surface waves to the development of a wide variety of practical devices and the application of these devices to systems problems in radar, communications and electronic warfare. He has also studied other microwave delay techniques employing YIG devices and superconductive slow wave structures. His cryogenics experience includes the design and fabrication of superconductive maser magnets and operation of these magnets in liquid helium baths as well as in closed-cycle refrigerators. In the area of plasma physics, Dr. Gandolfo has studied the interaction of electromagnetic waves with rocket exhaust plasmas and the effects of this interaction on radar and telemetry systems. He has also experimented with a coaxial-rail gun plasma accelerator. In radiation damage studies, he has measured and analyzed the effects of neutron and gamma irradiation on semiconductor devices. He also analy?ed the effects of high-energy proton bombardment on transistors.

Dr. Gandolfo is a member of the American Physical Society and a Senior Member of the IEEE.

**Alvin Malcolm Goodman** received a B.S.E. in 1952 from the Drexel Institute of Technology, Philadelphia, Pa. He did graduate work at Princeton University, receiving an M.A. in 1955 and a Ph.D. in 1958. From June 1956 to January 1957 he served as Research Assistant at Princeton University, and then as Assistant Professor of Electrical Engineering at the Case Institute of Technology up to June 1959. He performed research at RCA Laboratories as a summer employee in 1954, 1955, and 1958. He has been a Member of the Technical Staff since June 1959. During the year 1970–71, Dr. Goodman engaged in postdoctoral studies at the Swiss Federal Institute of Technology. Dr. Goodman has specialized in solid-state physics. His thesis subject was "December Effect and Trap Levels in Silver Chloride," and he has worked extensively in the areas of photoconductivity, metal-semiconductor contacts, metal-insulator contacts, insulator properties, and tunnel diodes. He has received two RCA Laboratories Achievement Awards for work on metal-semiconductor contacts (1963) and MNOS (metal-nitride-oxide-silicon) memory devices (1969). Since January 1973, Dr. Goodman has served as a Member of the Editorial Board of the Review of Scientific Instruments. He is a member of the American Physical Society, Sigma Xi and the Institute of Electrical and Electronics Engineers, and is listed in American Men of Science.

**E. P. Herrmann** received the B.S.E.E. degree from Rutgers University in 1969, with honors in a Physics Option Program, and the M.S.E.E. degree from Rutgers in 1972. Mr. Herrmann joined RCA's Microelectronic Technology Group in 1969. While with MET he worked in design and development of P-MOS large-scale integrated custom arrays, including dynamic and static digital logic arrays, self-scanned monolithic image sensors, and topologically adjusted arrays for radiation hardness.

In 1971, Mr. Herrmann joined the Advanced Technology Laboratories of RCA where he was assigned to their sensor development group. Here he was responsible for both system and device design and development in the areas of: infrared sensors utilizing pyroelectrics and quantum detectors, implementation of charge coupled devices for imaging, multiplexing, analog and digital storage, and integrating conventional MOS logic with charge coupled devices to form monolithic analog signal processing systems.

Mr. Herrmann joined the RCA Solid State Technology Center in 1976 where he is presently involved in the evaluation of bipolar integrated circuits for consumer applications and the evaluation of CMOS large scale integrated circuits for consumer applications. He is also actively involved in charge coupled device development as a consultant to the Advanced Technology Laboratories.

Mr. Herrmann is a member of Tau Beta Pi, Eta Kappa Nu, the IEEE and holds a professional engineer's license.

**L. T. Sachtleben** received his B.Sc. Degree in Physics and Mathematics from Antioch College. His work in optics began in the field of sound motion pictures, from which point he has continued as a generalist in optics at the RCA plants in Camden and Indianapolis. He has written or co-authored numerous published papers, and 47 patents have been issued to him. He is a member of SMPTE, OSA, AAPT, and NCTM.

**Leonard Schiff** received the B.E.E. from City College of New York in 1960, the M.S.E.E. from New York University in 1962, and the Ph.D. from the Polytechnic Institute of Brooklyn in 1968. From 1960 to 1966 he was employed by Bell Telephone Laboratories, Inc., Murray Hill, N.J., where he was concerned with various aspects of electronic switching systems. Since 1967, he has been with RCA Laboratories where he has been concerned with data transmission systems. He has worked on vehicle locations systems and on various system aspects of mobile radio, especially techniques for more efficient use of the spectrum. More recently, Dr. Schiff has been working on satellite communications systems.

Dr. Schiff is a member of Eta Kappa Nu, Tau Beta Pi, and Sigma Xi.

**D. B. Stepps** graduated with honors from California Polytechnic State University with a B.S.E.E. degree in 1973 and is currently pursuing a M.S.E.E. in electron devices at Drexel University.

In 1973 he joined RCA's Applied Physics Group, working with surface acoustic wave devices. After developing a saw pulse compression filter for NASA, he began working with charge coupled devices. Mr. Stepps has worked with CCD's in applications such as analog data reformatting for display systems, memories, CHIRP-Z-transform implementation, high resolution photography, and high speed imaging systems. At present, he is investigating CCD performance as programmable-tapped delay lines and analog correlators for varying length codes with applications in advanced radar systems. His main responsibilities include the design of supporting control circuits and drivers, plus experimental evaluation of the CCD's in the above mentioned areas.

RCA Review

A technical journal published quarterly by RCA Research and Engineering in cooperation with the subsidiaries and divisions of RCA.

# Index Volume 37, 1975

## March 1976 Volume 37 Number 1

## June 1976 Volume 37 Number 2

## September 1976 Volume 37 Number 3

## December 1976 Volume 37 Number 4

# Index to Authors, Volume 37, 1976